Dielectric Nanostructures for Control of Electromagnetic Waves

by

Toshihiko Shibanuma

A thesis submitted to Imperial College London
for the degree of Doctor of Philosophy

Experimental Solid State Physics Group (EXSS)
Department of Physics
Imperial College London

30th September 2017

Declaration of Originality

I hereby declare that the following work in this thesis is original and has been done by me. The work of others is appropriately acknowledged and referenced.

Toshihiko Shibanuma

for my family

Abstract

High refractive index dielectric nanoantennas have emerged as a promising unit for improving optical nanodevices by compensating the drawbacks of plasmonic nanoantennas, which have played a key role in nanophotonics to date. The features of high refractive index dielectric nanoantennas, such as low energy losses, excitation of strong magnetic resonances and enhancement of electric field inside and outside the particle, are expected to provide novel methods to manipulate electromagnetic waves in the nanometer scale.

In this thesis, we theoretically explore and experimentally demonstrate a variety of nanostructures based on high refractive index dielectric nanoantennas to aim at the efficient and tuneable control of electromagnetic waves in linear and nonlinear manners. Firstly, asymmetric Si dimers are investigated to achieve unidirectional forward scattering with high efficiency. An electric or magnetic dipole mode is excited in each particle constituting the asymmetric dimer at the same wavelength. The interference between these two dipolar modes can direct the scattered field selectively into the forward direction with high scattering efficiency. Secondly, we investigate metasurfaces built of array of Si nanodimers to obtain switching from high transmission to reflection depending on the incident polarization. The different linear polarization direction of the incident light can alter the hybridization modes of the constituent Si dimers and, hence, the effective permittivity and permeability of the metasurface. The resulted overlap and separation of the electric and magnetic dipolar resonances facilitates the control over the switching between high transmission and reflection. Thirdly, asymmetric Si dimers are explored to obtain tuneable control of directional scattering either in the left or right direction from the incident axis. Our theoretical analysis reveals that the electric or magnetic dipoles excited perpendicular to the dimer axis are mainly responsible for the tuneable scattering. Experimental demonstration of the scattering tuneability is carried out along the substrate by using back focal plane techniques combined with a prism coupling setup. Fourthly, we show that the third harmonic generation from a high refractive index dielectric nanoantenna can be significantly improved by adding a metallic component to build a metal-dielectric hybrid nanostructure. In this way, the plasmonic resonance of a Au nanoring can boost the anapole mode excited in a Si nanodisk, strongly enhancing the electric field inside the Si nanodisk. As a result, high third harmonic intensity and conversion efficiency can be achieved even in nanometer scale. Our findings on how we can attain the efficient and tuneable control of electromagnetic waves using high refractive index dielectric nanostructures will contribute to opening the new paths towards the realization of novel optical nanodevices.

Contents

Chapter 1

Introduction

1.1. General introduction of high refractive index dielectric nanostructures for nanophotonics

Nanophotonics is a research field which investigates light-matter interactions at the scale near or even smaller than the wavelength of light, aiming at gaining physical understandings and implementing useful manipulations of electromagnetic waves in the nanometer scale[1–4]. Research in nanophotonics has grown at a rapid pace recently for various reasons; the increase in capability of data processing that makes large numerical analyses and simulations possible, and the development in the fabrication and characterization techniques that facilitate the experimental demonstration of optical phenomena using subwavelength nanostructures. Both the research community and industry have given tremendous attention to nanophotonics, since it could play a key role in providing novel solutions towards recent global issues, such as climate change and the sharp rise in the amount of data processing. One of the promising solutions by nanophotonics is the development of highly efficient optical devices, such as solar cells and light emitting diodes[5–8], which could encourage the usage of renewable energy sources and reduce the emission of green-house gases by saving the energy consumption. Moreover, nanophotonics could lead to the development and fabrication of unprecedented devices, such as all-optical logical devices which can process data and information at an incredibly fast speed to meet the increasing demand for high speed and high quantity data processing[9–13]. However, to employ nanophotonics in these nanometer scale devices, a fundamental problem needs to be solved; the size of light confinement in free space is larger than its wavelength because of the Abbe's diffraction limit of light[14]. Furthermore, the strength of light-matter interactions at the nanometer scale is quite small because of the short light path and hence the small chance for light to significantly interact with matter[2,3]. These issues have to be overcome to attain control of electromagnetic waves in nanometer scale.

One of most established methods to manipulate light even beyond the diffraction limit is the use of plasmonic resonances of metallic nanoparticles[15–17]. Plasmonics – a field of research that deals with interactions between electromagnetic waves and free electrons in metals – has played an important role in the development of nanophotonics. When incident light shines on a metallic nanoparticle, a coherent oscillation of free electrons can be excited in the particle, which is called a localized surface plasmon resonance (LSPR). The restoring force is exerted on the oscillated electrons, which results in the enhancement of electric field near the particle surface. Since the size of metallic nanoparticles that show LSPR in visible light regime is in general several tens of nanometers, the enhanced electric field near the particle can be strongly confined beyond the diffraction limit of light[18,19]. Furthermore, LSPR excited in a nanoparticle prompts strong scattering of light in the far field. The amplitude and pattern of the scattered field can be determined and tuned by the mode of LSPR in nanometer scale[20–23]. These charateristics of plasmonic nanoparticles have made them one of the most promising techniques to manipulate light on the nanometer scale, stimulating many attempts to utilize them to realize highly efficient optical nanodevices. For example, the efficiency of some of the aforementioned optical devices, solar cells and light emitting diodes, can potentially be improved utilizing LSPR of metallic nanoparticles[24–26]. Also, LSPR can drastically improve the signal and sensitivity of spectroscopic and sensing applications, such as Raman, IR, and fluorescence, by amplifying the electric field intensity near targeted molecules[27–32]. Furthermore, as LSPRs can provide the control of electromagnetic fields even beyond the diffraction limit, plasmonic nanoparticles can be the building blocks of metamaterials, which show unique and intriguing optical properties. One typical example is the negative refractive index that can be achieved when both the effective permittivity and permeability of medium consisting of a lattice of plasmonic nanoparticles are negative[33–36]. Novel optical applications, such as an invisibility cloak and diffraction-free planar lenses, can be achieved using the optical effects of metamaterials[37–39], potentially providing a novel platform for controlling electromagnetic waves.

However, inevitable drawbacks of plasmonics have hindered the realization of those applications using plasmonic nanoparticles. The main problems, which will be discussed in detail in Chapter 2.1, are substantial energy losses and heat generated by the absorption of light, especially in near infrared (NIR) and visible regimes[40–44]. Plasmonic nanoparticles are generally made of noble metals, such as Au and Ag, which have a large imaginary part of the refractive index in the NIR and visible light regions[45]. The large value of the imaginary refractive index originates from ohmic losses of free electrons.

The energy dissipation decreases the quantum efficiency of optical devices using plasmonic nanoparticles[43]. Furthermore, a considerable amount of heat could be generated via damping processes of the energy dissipation at the LSPR[46]. Even though several attempts have utilized the heat from LSPR for thermal therapy of tumors[47], it would be undesirable in some cases, such as spectroscopic measurements of molecules that are sensitive to heat[48]. Another drawback of metallic nanoparticles is the lack of strong magnetic resonances. The interaction with the magnetic field of light is a key factor to manipulate electromagnetic waves, as well as the interaction with the electric field. However, large magnetic effects cannot be easily achieved with metallic nanoparticles; complex structures, such as a split-ring resonators, are required to excite magnetic modes when plasmonic nanoparticles are used[33]. This requirement makes the fabrication challenging on the nanometer scale, impeding the realization of practical plasmonic applications.

In recent years, nanostructures made of high refractive index dielectric materials, such as Si, GaAs, GaP and Ge, have emerged as an alternative to overcome the drawbacks of plasmonic nanoparticles. High-index dielectric nanoparticles can exhibit Mie resonances when excited with light, similar to the LSPRs, allowing their use in optical nanodevices. A clear advantage of high-index dielectric nanostructures over plasmonic ones is the lack of ohmic losses due to the absence of free electrons. This makes the imaginary part of their refractive index relatively small compared to that of metallic materials, leading to small light absorption and suppression of the heat generated[49–54]. Moreover, high-index dielectric nanoparticles are capable of exhibiting the excitation of not only electric but also magnetic resonances even with simple geometries, like a sphere or disk[55–59]. A rotational oscillation of displacement current can be generated inside the particle when the excitation wavelength in the particle approximately matches the size of the particle. From Maxwell equations, the rotation of the displacement current induces a magnetic field, offering the excitation of magnetic resonances in high-index dielectric nanostructures. The presence of the magnetic resonances can potentially introduce other ways of controlling electromagnetic waves (this will be presented in Chapter 2). Another distinct feature of high-index dielectric nanoparticles, compared to plasmonic ones, is the concentration of an enhanced electric field inside the particle. This would be suitable for optical nonlinear harmonic generations as the field enhancement in large volume of nonlinear susceptible media can increase the efficiency of nonlinear harmonic generations[60–62]. Even though the field enhancement by plasmonic nanoparticles is larger, the enhanced volume of the metallic material is generally too small to obtain high enough nonlinear harmonic generation efficiency[63–65]. Large volume

field enhancement is achieved inside high-index dielectric nanoparticles and is expected to improve the efficiency of harmonic generation, exhibiting the possibility of the realization of nonlinear optical nanodevices.

1.2. Current research and challenges

The magnetic resonances excited in high-index dielectric nanostructures can potentially interfere with the electric resonances. An example utilizing this interference is the directional control of electromagnetic field scattered from high-index dielectric nanoantennas. Besides the conventional platforms, such as particle waveguides and Yagi-uda nanoantennas[66–70], one of the unique methods to achieve directional light scattering from dielectric nanoantennas is the fulfillment of Kerker conditions. Kerker's conditions, which were proposed in 1983 using ideal magnetodielectric nanoparticles[71], provide a fundamental foundation on how the interference between the excited electric and magnetic resonances results in unidirectional forward or backward scattering. By satisfying Kerker's conditions, a simple sphere and cylinder of high-index dielectrics can exhibit unidirectional forward and backward scattering[72–75].

The excitation of magnetic resonances provides not only the control over the scattering of dielectric nanoantennas, but also the control over the transmission or reflection of dielectric metasurfaces consisting of arrays of high-index dielectric nanoantennas. In the ideal case where the excited electric and magnetic resonances show a perfect spectral overlap, high transmission with a full 2π phase control was theoretically proposed and experimentally demonstrated[76,77]. The high transmission has been achieved with dielectric metasurfaces with low-aspect ratio resonators, which would be preferable for spectral overlapping. On the other hand, a high reflection of more than 99 % was demonstrated with metasurfaces made of arrays of high aspect ratio dielectric resonators[78–80]. The mechanism behind the high reflection is either negative permittivity or negative permeability, which can be achieved based on the peak separation between the electric and magnetic dipolar resonances.

Besides the linear optical effects shown above, nonlinear optical phenomena can be attained using high-index dielectric nanoantennas with high efficiency. In particular, the third harmonic generation (THG) from dielectric nanoantennas has been intensely explored since THG can be generated from crystals even with an inversion symmetry[60,81–84]. High refractive index in general results in high third order harmonic susceptibilities

from the generalized Miller's rule[85], making high-index dielectrics a promising material for nonlinear effects. Furthermore, the electric field is enhanced inside the dielectric nanostructures, offering a large volume enhancement[60,86]. Among various studies of THG from high-index dielectric nanostructures[60,61,81–83,87], the largest value of TH efficiency thus far is 0.001 %, which was achieved from a high order anapole mode (this term will be described in detail later) excited in a Ge nanodisk[87]. This conversion efficiency is quite high in nanometer scale, in comparison to plasmonic nanoantennas.

Thus, high-index dielectric nanoantennas have many interesting optical effects and great potential in extending the capability of devices based on nanophtonics. However, there are still several problems that need to be addressed in order to improve the usability, practicality and feasibility of high-index dielectric nanoantennas. The first issue is the efficiency of the optical effects from dielectric nanostructures. Although Kerker's conditions provide high directionality in light scattering, the scattering efficiency is quite low with a simple spherical dielectric nanoparticle because of the spectral separation of the excited electric and magnetic dipoles[73,74]. Also, the nonlinear third harmonic generation still showed low conversion efficiencies, which are not sufficient to apply to practical nanodevices[87,88]. The efficiency of optical effects of high-index dielectric nanostructures is crucial to fully utilize their advantages of low energy losses and low absorption. The second issue is the lack of tuneablity of the obtained optical phenomena. For example, Kerker's conditions can only determine the direction of scattering along the incident axis, limiting the possibility of how we can exploit the directional scattering in practical applications. Another example is high-index dielectric metasurfaces showing only high transmission or reflection. Whether the high transmission or reflection can be achieved is usually determined by the shape of nanoantennas and hence cannot be actively tuned. Some attempts using liquid crystals or circular polarization states of the incident light have been conducted to add tuneability to these highly transmissive or reflective metasurfaces[89–91]. Nevertheless, more simple and efficient methods to tune the transmission and reflection are still needed.

1.3. Objective and structure of the thesis

In this thesis, we explore various nanostructures based on high-index dielectric materials to extend their capability of controlling electromagnetic waves in nanometer scale, especially in terms of efficiency and tuneability.

In Chapter 2, theoretical background will be introduced to understand how high-index dielectric nanostructures can exhibit low loss electric and magnetic resonances. First, we will review the response of LSPR in metallic nanoparticles and their drawback of large absorption for comparison. Mie resonances of high-index dielectric nanostructures are then explored to reveal the origin of low absorption and excitation of magnetic resonances, followed by an explanation of optical effects that can be obtained with the resonances of dielectric nanostructures. We will discuss how Kerker conditions can lead to unidirectional forward or backward scattering thanks to the interference between electric and magnetic resonances. High-index dielectric metasurfaces showing high transmission or reflection are also explored, detailing the importance of tuning permittivity and permeability in attaining the desirable optical behavior of the metasurfaces. In the following section, we examine the excitation of a unique mode, a non-radiative anapole mode, which can be realized by a destructive interference between an electric and toroidal dipolar resonances in a high-index dielectric nanoparticle. Finally, nonlinear THG from high-index dielectric nanostructures are studied. Special attention will be paid to the clarification of mechanisms behind the high conversion efficiency.

Chapter 3 details theoretical, numerical and experimental methods that we used to understand and demonstrate novel optical effects which are the focus of this thesis. A theoretical model to understand the optical behavior of high-index dielectric dimers, an analytical dipole-dipole model based on Mie theory, is re-constructed for asymmetric dielectric dimers. Since the finite-difference time-domain (FDTD) method is used throughout the thesis for numerical simulations of our high-index dielectric nanostructures, its basic theory is introduced in this chapter. This is followed by a description of the fabrication procedure we used to fabricate two types of nanostructures; all-dielectric and hybrid metal -dielectric nanostructures. Dry fabrication processes including electron beam lithography and reactive ion etching techniques are employed to fabricate target nanostructures. Characterization methods and setups, which are introduced in this chapter, vary depending on the purpose of the measurement. To obtain the spectra of the scattering intensity into the forward and backward direction from single nanoantennas, dark field optical spectroscopy with a microscope is set up. Transmission, reflection and extinction spectra are retrieved by Fourier transform infrared spectroscopy technique. We also build up a back focal plane imaging system combined with prism coupling to monitor the distribution of light scattering which propagates along the substrate. The nonlinear third order harmonic generation is observed by nonlinear optical measurement setup using fs-pulsed laser, which is developed for single nanoantennas measurement.

The following four chapters 4-7 present our theoretical and experimental work on how we can improve the performance of high-index dielectric nanostructures in terms of efficiency and tuneability. Chapter 4 explores asymmetric Si dimers for highly efficient unidirectional forward scattering by satisfying the first Kerker condition. The electric and magnetic dipolar resonances are excited in each particle of the Si dimer at the same wavelength. This fulfills the achievement of the first Kerker condition at the peak of the resonances, leading to the high scattering efficiency towards the forward direction. The analytical dipole-dipole model confirms that the first Kerker condition is satisfied even with the Si dimer. The experimental demonstration of highly unidirectional forward scattering is carried out using dimers of Si diskl nanoparticles fabricated on a sapphire substrate. The forward and backward scattering is characterized by the dark field optical spectroscopy with a microscope. The idea of using dielectric trimers for unidirectional forward scattering at multi-wavelengths is also proposed to achieve broadband responses.

In Chapter 5, metasurfaces made of high-index dielectric nanodimer arrays are studied to obtain the tuneability to switch high transmission to reflection by changing the linear polarization of light. Because of the orientation of each dipole, the interaction between electric and magnetic dipoles excited in the Si dimer is modulated by the linearly polarized incidence. While the metasurface itself remains passive, resulting mode hybridizations present the spectral overlap and separation of the electric and magnetic dipoles, which is preferable for high transmission and reflection, respectively. Metasurfaces of Si disk nanodimers verify the switching between the high transmission and reflection by linear polarization in experiment using the microscopic Fourier transform infrared measurement system.

Chapter 6 presents tuneable control of light scattering direction either to the left or right side from the incident axis using asymmetric dielectric dimers. Detailed theoretical investigations reveal that the interference between the electric or magnetic dipoles excited in each particle can tune the light scattering direction, depending on the excitation wavelength. Experimental demonstration of tuneable light scattering along the substrate from an asymmetric Si dimer is conducted using a specially designed back focal plane imaging system combined with prism coupling. An evanescent wave excited at the interface propagates along the substrate, exciting the fabricated Si dimer. An objective with high numerical aperture collects the scattered fields, which provides scattering patterns on the back focal plane. The applications of the asymmetric dimers for optical nanocircuitry is theoretically studied by achieving selective excitation using the tuneable directional scattering.

In Chapter 7, highly efficient third harmonic generation from metal–dielectric hybrid

nanostructures is presented. Si nanodisk excites an anapole mode, which is a unique excitation mode confining electric field inside the dielectric nanoparticle. The anapole mode in the Si nanodisk is enhanced more by coupling with the plasmonic resonance of a Au nanoring. The greatly enhanced electric field inside the Si nanodisk in the hybrid structures leads to the high efficiency of third harmonic generation, reaching 0.007 % at maximum. This value is, to our best knowledge, the highest value in third harmonic generation in the nanometer scale reported so far. The scalability of the efficient THG from the hybrid nanoantennas is also demonstrated by changing their geometrical parameters.

Chapter 8 delivers the conclusion of our work and emphasizes its crucial role in obtaining efficient and tuneable control of electromagnetic waves using dielectric nanostructures for the realization of novel optical applications in nanometer scale. Prospective future work based on our studies is also proposed to further understand and improve the optical effects offered by high-index dielectric nanostructures.

We believe that the work described in this thesis can provide us with new schemes to boost the development of novel optical devices in nanometer scale using dielectric nanostructures.

Chapter 2

Theories - the resonances and optical effects of dielectric nanostructures

This chapter introduces the theoretical descriptions of the resonances and optical effects of high-index dielectric nanostructures. We first explore the localized surface plasmon resonances (LSPRs) of metallic nanoparticles and their drawbacks which have hindered the realization of nano-photonic applications using plasmonic nanoparticles. The theoretical investigations of resonances of high-index dielectric nanoparticles based on Mie theory are conducted in detail to clarify the origin of their low-loss electric and magnetic resonances. The excitation of the magnetic resonant modes in the dielectric nanoparticles is a key aspect because it enables the achievement of some unique and intriguing optical effects which have already been broadly studied with ideal magnetic nanoparticles. One of these optical effects is the Kerker conditions, by which unidirectional forward or backward scattering can be achieved due to the interference between the electric and magnetic resonances excited in high-index dielectric nanoparticles. Also, we examine dielectric metasurfaces that can be used to tune their effective permittivity and permeability by electric and magnetic resonances of dielectric nanoparticles. Later in this section, how the precise control of these optical constants gives rise to high transmission or reflection from the metasurface will be presented. The next section describes the excitation of an anapole mode using dielectric nanostructures. This mode is non-radiating due to destructive interference between electric and toroidal dipole moments, resulting in the strong field confinement inside dielectric nanostructres. The last part of this chapter will be devoted to the introduction of the nonlinear optical effects, specifically third harmonic generation, that can be achieved with resonant high-index dielectric nanoparticles. High-index dielectric nanoparticles improve the efficiency of third harmonic generation in nanometer scale, an advantage compared to their counterpart plasmonic nanoparticles.

2.1. Localized surface plasmon resonances of metallic nanoparticles and their drawbacks

When illuminated by light at a certain wavelength, small metallic nanoparticles exhibit a collective oscillation of free electrons coupled to the electromagnetic field. This excitation is so-called localized surface plasmon resonance (LSPR), and it is capable of confining electromagnetic fields even below the diffraction limit[15,16,18,92–94]. In this section, we go through the physics of LSPR and discuss its drawbacks, specifically the problems associated with the absorption of light.

In the case that the radius a of a spherical metallic particle is much smaller than the incident wavelength in the medium, the incident field $\mathbf{E}_0$ generates the electric dipole moment $\mathbf{p}$, which is proportional to the incident field, in the particle. The polarizability at the LSPR is calculated from the definition $\mathbf{p} = \varepsilon_0\varepsilon_m\alpha\mathbf{E}_0$ as follows[15]

$$\alpha = 4\pi a^3 \frac{\varepsilon - \varepsilon_m}{\varepsilon + 2\varepsilon_m} \tag{2.1}$$

where ε and ε_m are the permittivity of the metallic nanoparticle and medium, respectively. Thus, the metallic nanoparticle experiences a resonance when the polarizability is maximized. In other word, the LSPR of a metallic particle is excited when the system's permittivity profile satisfies the following condition

$$\mathrm{Re}(\varepsilon + 2\varepsilon_m) = 0 \tag{2.2}$$

and $\mathrm{Im}(\varepsilon + 2\varepsilon_m)$ is small, although it cannot be exactly zero due to the causality.

The scattering and absorption of the particle are quantitatively estimated by scattering and absorption cross sections, C_{sca} and C_{abs}, respectively, which can be calculated using polarizability α as follows[15].

$$C_{\mathrm{sca}} = \frac{k^4}{6\pi}|\alpha|^2 \tag{2.3}$$

$$C_{\mathrm{abs}} = k\mathrm{Im}(\alpha) \tag{2.4}$$

$$C_{\text{ext}} = C_{\text{scat}} + C_{\text{abs}} \tag{2.5}$$

where k is the wavenumber in free space. Figure 2.1 shows the spectra of scattering, absorption and extinction of a Au nanoparticle (50 nm diameter) in air, calculated using eq. (2.3) – (2.5). The optical constants were obtained from a ref[45]. The spectrum is normalized by the geometrical cross section of the nanoparticle. A peak around 520 nm is observed in the spectrum of the Au nanoparticle, corresponding to the LSPR exciting electric dipole mode[15]. This resonance is dominated by the substantial non-radiative absorption, rather than radiative scattering, which is caused by the ohmic losses in the Au nanoparticle[40]. Also, the absorption would result in a considerable amount of heat, which reportedly reaches up to 1000 K[95]. The generated heat may cause problems in, for instance, sensing applications for molecules which are sensitive to heat, or optical devices whose performance could be degraded by heat[51]. These drawbacks of plasmonic nanoparticles are believed to be the main causes hampering the development and realization of nanophotonics applications using LSPRs[41].

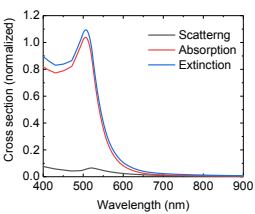

Figure 2.1. Scattering, absorption and extinction spectra of a Au nanoparticle (diameter 50 nm) calculated by the eq. (2.3) – (2.5).

2.2. Mie resonances of high refractive index dielectric nanoparticles

While metallic nanoparticles exhibit LSPRs due to the coherent oscillation of free electrons, high-index dielectric nanoparticles can excite resonances due to the displacement current inside the particle instead[55,56,96,97]. This type of resonances can be exactly determined by Mie theory in the case of a spherical nanoparticle[98,99]. This section discusses how electric and magnetic resonances can be achieved using high-index dielectric nanoparticles with low energy losses.

Electromagnetic waves that satisfy Maxwell equations and wave equations can be described in spherical coordinates using vector spherical harmonics **M** and **N** as follows[98].

$$\mathbf{M}_{emn} = \frac{-m}{\sin\theta}\sin m\phi\, P_n^m(\cos\theta) z_n(\rho)\mathbf{u}_\theta - \cos m\phi \frac{dP_n^m(\cos\theta)}{d\theta} z_n(\rho)\mathbf{u}_\phi \tag{2.6}$$

$$\mathbf{M}_{omn} = \frac{m}{\sin\theta}\cos m\phi\, P_n^m(\cos\theta) z_n(\rho)\mathbf{u}_\theta - \sin m\phi \frac{dP_n^m(\cos\theta)}{d\theta} z_n(\rho)\mathbf{u}_\phi \tag{2.7}$$

$$\mathbf{N}_{emn} = \frac{z_n(\rho)}{\rho}\sin m\phi\, n(n+1)P_n^m(\cos\theta)\mathbf{u}_r - \cos m\phi \frac{dP_n^m(\cos\theta)}{d\theta}\frac{1}{\rho}\frac{d}{d\rho}\{\rho z_n(\rho)\}\mathbf{u}_\theta - m\sin m\phi \frac{P_n^m(\cos\theta)}{\sin\theta}\frac{1}{\rho}\frac{d}{d\rho}\{\rho z_n(\rho)\}\mathbf{u}_\phi \tag{2.8}$$

$$\mathbf{N}_{omn} = \frac{z_n(\rho)}{\rho}\sin m\phi\, n(n+1)P_n^m(\cos\theta)\mathbf{u}_r + \sin m\phi \frac{dP_n^m(\cos\theta)}{d\theta}\frac{1}{\rho}\frac{d}{d\rho}\{\rho z_n(\rho)\}\mathbf{u}_\theta + m\cos m\phi \frac{P_n^m(\cos\theta)}{\sin\theta}\frac{1}{\rho}\frac{d}{d\rho}\{\rho z_n(\rho)\}\mathbf{u}_\phi \tag{2.9}$$

where $P_n^m(\cos\theta)$ is the associated Legendre function of the first kind of degree n and order m, z_n is any of four spherical Bessel functions (j_n, y_n, $h_n^{(1)}$ or $h_n^{(2)}$), and ρ is the dimensionless variable $\rho = kr$. The incident electric and magnetic fields ($\mathbf{E}_i$ and $\mathbf{H}_i$), the

scattered fields ($\mathbf{E}_s$ and $\mathbf{H}_s$), and the fields inside the spherical particle ($\mathbf{E}_l$ and $\mathbf{H}_l$) are calculated with following equations[98].

$$\mathbf{E}_i = E_0 \sum_{n=1}^{\infty} i^n \frac{2n+1}{n(n+1)} \left(\mathbf{M}_{o1n}^{(1)} - i\mathbf{N}_{e1n}^{(1)} \right) \tag{2.10}$$

$$\mathbf{H}_i = \frac{-k}{\omega \mu_m} E_0 \sum_{n=1}^{\infty} i^n \frac{2n+1}{n(n+1)} \left(\mathbf{M}_{e1n}^{(1)} + i\mathbf{N}_{o1n}^{(1)} \right) \tag{2.11}$$

$$\mathbf{E}_s = \sum_{n=1}^{\infty} E_n \left(i a_n \mathbf{N}_{e1n}^{(3)} - b_n \mathbf{M}_{o1n}^{(3)} \right) \tag{2.12}$$

$$\mathbf{H}_s = \frac{k}{\omega \mu_m} \sum_{n=1}^{\infty} E_n \left(i b_n \mathbf{N}_{o1n}^{(3)} + a_n \mathbf{M}_{e1n}^{(3)} \right) \tag{2.13}$$

$$\mathbf{E}_l = \sum_{n=1}^{\infty} E_n \left(c_n \mathbf{M}_{o1n}^{(1)} - i d_n \mathbf{N}_{e1n}^{(1)} \right) \tag{2.14}$$

$$\mathbf{H}_l = \frac{-nk}{\omega \mu} \sum_{n=1}^{\infty} E_n \left(d_n \mathbf{M}_{e1n}^{(1)} + i c_n \mathbf{N}_{o1n}^{(1)} \right) \tag{2.15}$$

where the superscript (1) or (3) to the vector spherical harmonics indicate the number of kind of Bessel functions, μ and μ_m are the permeability of the particle and medium, $E_n = i^n E_0(2n + 1)/n(n + 1)$, and a_n, b_n, c_n, and d_n are the coefficients of the scattering electric and magnetic fields and fields inside the particle.

Now we try to solve the equations for unknown four coefficients by imposing boundary condition at the interface of the particle and medium $r = a$.

$$(\mathbf{E}_i + \mathbf{E}_s - \mathbf{E}_l) \times \mathbf{u}_r = (\mathbf{H}_i + \mathbf{H}_s - \mathbf{H}_l) \times \mathbf{u}_r = 0 \tag{2.16}$$

Then the four coefficients are calculated as follows[98].

$$a_n = \frac{m\psi_n(mx)\psi_n'(x) - \psi_n(x)\psi_n'(mx)}{m\psi_n(mx)\xi_n'(x) - \xi_n(x)\psi_n'(mx)} \tag{2.17}$$

$$b_n = \frac{\psi_n(mx)\psi_n'(x) - m\psi_n(x)\psi_n'(mx)}{\psi_n(mx)\xi_n'(x) - m\xi_n(x)\psi_n'(mx)} \tag{2.18}$$

$$c_n = \frac{\mu j_n(x)\left\{xh_n^{(1)}(x)\right\}' - \mu h_n^{(1)}(x)\{xj_n(x)\}'}{\mu j_n(mx)\left\{xh_n^{(1)}(x)\right\}' - \mu_m h_n^{(1)}(x)\{mxj_n(mx)\}'} \tag{2.19}$$

$$d_n = \frac{\mu m j_n(x)\left\{xh_n^{(1)}(x)\right\}' - \mu m h_n^{(1)}(x)\{xj_n(x)\}'}{\mu_m m^2 j_n(mx)\left\{xh_n^{(1)}(x)\right\}' - \mu h_n^{(1)}(x)\{mxj_n(mx)\}'} \tag{2.20}$$

where x is the size parameter ka, m is relaive refractive index N/N_m (N and N_m are the refractive indices of the particle and medium, respectively), ψ_n and ξ_n are the Riccati Bessel functions.

$$\psi_n = \rho j_n(\rho), \quad \xi_n = \rho h_n^{(1)}(\rho), \tag{2.21}$$

Now that we have expressions for the scattered electric field. Then the extinction, scattering and absorption cross sections are determined[98].

$$C_{sca} = \frac{2\pi}{k^2}\sum_{n=1}^{\infty}(2n+1)(|a_n|^2 + |b_n|^2) \tag{2.22}$$

$$C_{ext} = \frac{2\pi}{k^2}\sum_{n=1}^{\infty}(2n+1)\mathrm{Re}(a_n + b_n) \tag{2.23}$$

$$C_{abs} = C_{ext} - C_{sca} \tag{2.24}$$

Note that the Mie coefficients are the function only of the size parameter and relative refractive index. Therefore, the scattering and absorption properties can be determined only by the diameter and optical constants of the nanoparticle.

Figure 2.2a shows the extinction, scattering and absorption cross section spectra of a Si nanoparticle, deriving from the calculation of Mie coefficients a_1 and b_1, which correspond to the electric and magnetic dipoles, respectively[98]. The diameter of the Si nanoparticles is set as 160 nm, and the refractive indices are obtained from ref[45]. The Si nanoparticle shows absorption significantly smaller than the scattering throughout the optical spectra, showing the low loss resonances in contrast to the LSPR of metallic nanoparticles presented in the previous section. Furthermore, there are two distinct peaks at λ = 520 nm and 642 nm observed in the extinction spectrum. To clarify the origin of these two peaks, we decomposed the extinction spectrum into the two Mie coefficients a_1 and b_1 (Figure 2.2b). Both the two coefficients, which correspond to the electric and magnetic dipolar resonances, present the resonance at λ = 520 nm and 642 nm, confirming the capability of exciting electric and magnetic dipolar modes. The presence of the magnetic resonances is a clear advantage of high-index dielectric nanoparticles over plasmonic ones. This offers a new mechanism to control the behavior of electromagnetic waves when interacting with matter, which will be shown in the later part of this chapter. Note that higher order resonances, such as quadrupolar modes, are neglected here since the higher order resonances are excited at shorter wavelengths and do not have significant influence on the optical effects which are discussed in this thesis.

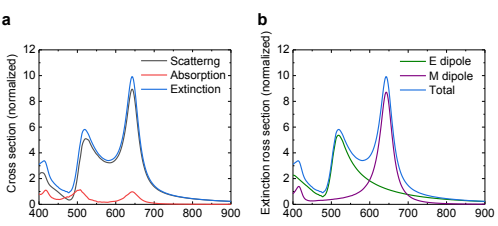

Figure 2.2. (a) Scattering, absorption and extinction spectra of a Si nanoparticle (diameter 160 nm) calculated by Mie theory. (b) The contribution of electric (a_1) and magnetic (b_1) dipoles to the extinction spectrum.

To understand the origin of the magnetic dipolar mode excited in Si nanoparticles, the electric field inside and outside the particle under plane wave illumination is calculated at λ = 520 nm and 642 nm using eq. (2.14) and (2.15), and shown in Figure 2.3. At λ = 520 nm, where the electric dipolar resonance is obtained, the oscillation of the displacement current is observed, offering a similar field map just outside the particle to that of a plasmonic resonance. On the other hand, the rotation of the displacement current is achieved inside the particle at the resonance of magnetic dipolar mode at λ = 624 nm. This rotational oscillation of the displacement current produces the oscillation of magnetic field at the centre from Maxwell equations, which results in the excitation of the magnetic dipole. The rotation of the displacement current can be achieved due to the small absorption of light in the Si nanoparticle, allowing electromagnetic waves to penetrate the particle. Thus, the electric field can be reversed at each side of the particle, causing the rotation of the current. The deep penetration of electromagnetic field into the particle is not possible in the case of noble metals, because of their large imaginary part of refractive index and hence very thin skin depth.

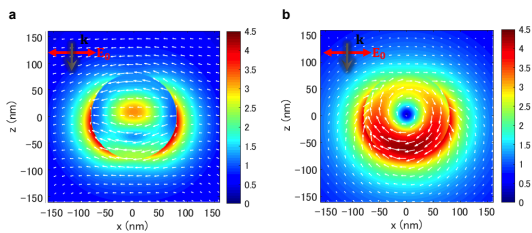

Figure 2.3. Normalized electric field distribution of the Si nanoparticle (diameter 160 nm) at λ = 520 nm (a) and λ = 642 nm (b), which correspond to the electric and magnetic dipolar modes, respectively. White arrows in the figures show the real part of electric field vectors at each calculation cell.

2.3. Achievement of Kerker conditions using dielectric nanoantennas for unidirectional light scattering

Dielectric nanostructures possess not only electric but also magnetic resonances, even without considering complex shapes or arrangements. This feature allows dielectric nanoantennas to perform intriguing optical effects, one of which is unidirectional forward and backward scattering when the Kerker conditions are fulfilled[71,72,100]. The presence of the magnetic resonances induces constructive and destructive interferences with the electric modes, which defines the radiation pattern of the scattered field. At certain wavelengths, the electromagnetic wave can then be scattered from the dielectric nanoparticles selectively either in the forward or backward direction. In this section, we theoretically revisit the Kerker conditions and verify the fulfillment with a Si nanoparticle.

Now we only consider the electric and magnetic dipole excitations and exclude any other higher order multipole modes. The scattering cross section (2.22) is rewritten as follows.

$$C_{sca} = \frac{6\pi}{k^2}(|a_1|^2 + |b_1|^2) \tag{2.25}$$

The far field scattering distribution can be calculated as the differential scattering cross section in terms of the solid angle, which is averaged over the polarization of the incident light[72],

$$\frac{dC_{sca}}{d\Omega}(\theta) = \frac{9}{8k^2}\{(|a_1|^2 + |b_n|^2)(1+\cos^2\theta) + 4\mathrm{Re}(a_1 b_1{}^*)\cos\theta\} \tag{2.26}$$

where the exact forward and backward directions correspond to θ = 0° and θ = 180°, respectively. The scattering intensities in the forward (0°) and backward (180°) directions can be then simplified as

$$\frac{dC_{sca}}{d\Omega}(0°) = \frac{9}{4k^2}|a_1 + b_1|^2 \tag{2.27}$$

$$\frac{dC_{sca}}{d\Omega}(180°) = \frac{9}{4k^2}|a_1 - b_1|^2 \quad (2.28)$$

These equations suggest that, when a_1 = b_1, the backward scattering is completely suppressed and unidirectional forward scattering can be achieved. This is the fulfillment of the first Kerker condition. On the other hand, the forward scattering would have zero intensity if a_1 = -b_1. However, because of the causality principle, the real parts of a_1 and b_1 are always positive, preventing the achievement of the equality condition between a_1 and -b_1. Nonetheless, if the absorption of the particle is negligible, the forward scattering intensity shows a minimum when Re(a_1) = Re(b_1) and Im(a_1) = -Im(b_1). This leads to the fulfillment of the second Kerker condition.

Although the Kerker conditions were first theoretically proposed more than 30 years ago using ideal magnetodielectric particles[71], they have recently re-emerged in the science community after high-index dielectric nanoparticles arose as low loss nanoantennas which can excite both the electric and magnetic dipoles[73,75]. Even simple spherical nanoparticles made of Si have been reported to satisfy the first and second Kerker conditions, exhibiting selective forward and backward scattering[72]. As an example, Figure 2.4a shows the forward and backward scattering spectra of a Si spherical nanoparticle of 160 nm diameter calculated based on the Mie theory, detailed in the previous section. At λ = 594 nm, the forward scattering presents a clear dip and, hence, the F/B ratio becomes minimum. As a result, the far field pattern shows a very small amount of forward scattering, resulting in directional backward scattering (Figure 2.4b). On the other hand, the backward scattering is clearly suppressed at λ = 694 nm. This leads to a far field distribution dominated by the forward scattering, as shown in Figure 2.4c. Note that the wavelengths of the Kerker conditions coincide with the intersecting points between a_1 and b_1 spectra shown in Figure 2.2b, providing the proof of the fulfillment of the Kerker conditions.

2.4.Highly transmissive or reflective dielectric metasurfaces

Metasurfaces are thin optical layers with nanoresonators that are artificially fabricated to exhibit custom and unique optical effects that other materials in nature do not offer. Considering Maxwell equations and wave equations, the permittivity and permeability of the metasurfaces are keys to controlling electromagnetic waves. One

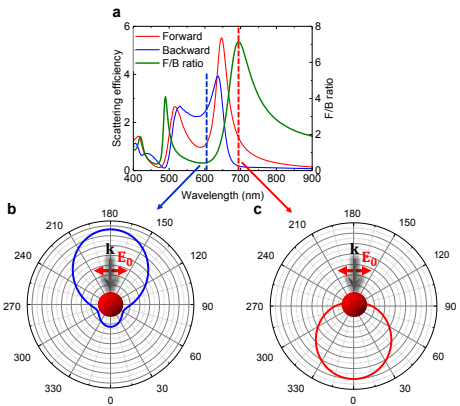

Figure 2.4. (a) Forward and backward scattering spectra of a Si nanoparticle (diameter 160 nm), and the ratio between forward and backward scattering. (b,c) Far field scattering patterns of the Si nanoparticle at λ = 594 nm (a) and λ = 694 nm (b).

example of optical effects obtained by metasurfaces is the near unity transmission or reflection of light by controlling the permittivity and permeability[76–79], which is discussed in this section. For simplicity, we consider the transmission and reflection at the interface between air and a semi-infinite medium.

The reflection coefficient r and intensity R of a plane wave at normal incidence are defined as follows at the interface[78].

$$r = \frac{z-1}{z+1} = \frac{(z'-1)+iz''}{(z'+1)+iz'} \tag{2.29}$$

$$R = |r|^2 = \frac{(z'-1)^2+z''^2}{(z'+1)^2+z''^2} \tag{2.30}$$

where $z = z' + iz''$ is the complex impedance of the metasurface calculated by $z = \sqrt{\mu/\varepsilon}$, in which ε ($= \varepsilon' + i\varepsilon''$) is the complex permittivity and μ ($= \mu' + i\mu''$) is the complex permeability.

Firstly, we explore the conditions to achieve near unity transmission, which requires $R = 0$. This can be satisfied when $z' = 1$ and $z'' = 0$. Simple arithmetic manipulation gives the requirements of ε and μ.

$$\varepsilon' = \mu' \tag{2.31}$$

$$\varepsilon'' = \mu'' = 0 \tag{2.32}$$

These two conditions can be satisfied with a high-index dielectric metasurface at the electric and magnetic resonances of its constituent nanoantennas, if these two resonances have a perfect spectral overlap[77]. From Lewin's effective medium model[101], the effective permittivity and permeability of a metasurface are equal when the Mie coefficients a_1 and b_1 of component nanoantennas are equal. This can be satisfied with high-index dielectric nanoantennas in analogy with the first Kerker condition which was explained in the previous section. Furthermore, the electric and magnetic resonances can be achieved with a small amount of absorption by using high-index dielectric nanoantennas, leading to the fulfilment of eq. (2.32)[79]. In fact, the near unity transmission with full 2π phase control has been demonstrated using metasurfaces made of dielectric nanodisks[77,102–104]. For high transmission, nanodisks with low aspect ratios have been used to present spectral overlap between the electric and magnetic dipolar resonances (Figure 2.5a).

Secondly, the near unity reflection, which is $R = 1$, is explored. The required condition is $z' = 0$ from eq. (2.30), which can be converted to the requirements of ε and μ as follows.

$$\frac{\varepsilon'}{\mu'} < 0 \tag{2.33}$$

$$\varepsilon'\mu'' - \varepsilon''\mu' = 0 \tag{2.34}$$

Dielectric metasurfaces again could fulfill these two conditions. When the electric and magnetic dipolar resonances of the high-index dielectric nanoatnennas forming the metasurfaces are separated sufficiently, dispersion-like resonances occur in the real part

of effective permittivity and permeability at different wavelengths[101]. This provides certain wavelength ranges where either ε' or μ' can be a negative value, leading to a single negative metamaterial and satisfying the eq. (2.33)[78–80,105,106]. Although eq. (2.34) looks more restrictive, low loss dielectric metasurfaces have near zero ε'' or μ'', allowing the approximate fulfilment of the eq. (2.34). The perfect reflection was theoretically and experimentally demonstrated using dielectric metasurfaces which are designed with dielectric nanoantennas[79,80]. The aspect ratio of the dielectric nanoantennas in this case is assumed to be high enough to possess a spectral separation between the electric and magnetic dipolar resonances (Figure 2.5b).

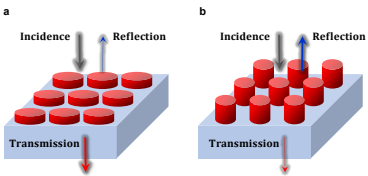

Figure 2.5. Schematic images of dielectric metasurfaces showing selective transmission (a) or reflection (b). The aspect ratio of the dielectric nanoantennas determines the distance of spectral separation between the electric and magnetic dipolar resonances, and hence, if the high reflection or transmission can be realized.

2.5. Excitation of non-radiating anapole modes in dielectric nanoparticles

The excitation of non-radiating resonant modes enables the strong concentration of electromagnetic fields into a particle. An anapole mode is a non-radiating resonance and vanishes in the far field[107], where electric and toroidal dipoles are destructively interfered (Figure 2.6). The toroidal dipole is one of terms in the multipole expansion of the current distribution inside the particle[108]. In this mode, an electric field distribution of solenoid shape induces a magnetic toroid generating an electric field at the center of the particle,

which has the same shape as the electric dipole. Therefore, the electric and toroidal dipoles are indistinguishable in the far field.

From the current inside the particle, an electric dipole moment **p** can be calculated with displacement current inside the particle **J** in the following equations[107].

$$\mathbf{p} = \frac{i}{\omega}\int \mathbf{J}d\mathbf{r} \tag{2.35}$$

$$\mathbf{J} = -i\omega\varepsilon_0(n^2-1)\mathbf{E} \tag{2.36}$$

On the other hand, a toroidal dipole **t** can also be calculated as follows[107].

$$\mathbf{t} = \frac{1}{10c}\int\{(\mathbf{r}\cdot\mathbf{J}) - 2r^2\mathbf{J}\}d\mathbf{r} \tag{2.37}$$

By summing the contribution from these two dipolar modes, the scattered field can now be described as[107]

$$\mathbf{E}_s = \frac{k^2}{4\pi\varepsilon_0}(\mathbf{n}\times\mathbf{p}\times\mathbf{n} + ik\mathbf{n}\times\mathbf{t}\times\mathbf{n}) \tag{2.38}$$

where **n** is the unit vector of the observation point. Eq. (2.38) suggests that the scattered field could vanish (E_s = 0) when the electric and toroidal dipoles are the same in amplitude but are out of phase

$$\mathbf{p} = -ik\mathbf{t} \tag{2.39}$$

Thus, by the destructive interference between the electric and toroidal dipoles, the non-radiating anapole mode can be achieved. The anapole mode was experimentally demonstrated very recently using high-index dielectric nanoantennas[107,109], showing the potential of boosting the optical effects of dielectric nanostructures, such as broadband absorption and nonlinear optical harmonic generation[61,87,110].

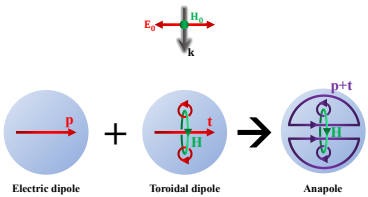

Figure 2.6. Schematic illustration of the excitation of an anapole mode. In the toroidal dipole moment, solenoid displacement currents generate a circulating magnetic field. The resulted toroidal dipole has the same shape as the electric dipole, leading to the destructive interference in far field.

2.6. Third harmonic generation from dielectric nanoparticles

Nonlinear optics describes optical phenomena that respond in a nonlinear manner to the strength of an applied electromagnetic field[85]. One of the beneficial nonlinear effects is harmonic generation, currently used in commercial laser equipment by exciting bulk nonlinear crystals with large illumination powers[111]. In particular, third harmonic generation (THG), a process that coherently triples the energy of the incident photon, can be induced regardless of the inversion symmetry of the media, in contrast to, for example, the case of second harmonic generation (SHG). Interestingly, under appropriate conditions, this nonlinear phenomenon can also be realized at the nanometer scale, becoming a subject of intense research due to its potential applications in (bio)-imaging[112], drug delivery[113] and high-efficiency solar cells[114,115].

In the macroscopic scale, third harmonic (TH) conversion efficiencies can be optimized through a phase-matching condition, $k_{3\omega} = 3k_{\omega}$ (k is the wavenumber, ω is the frequency of the incident light), which produces a strong constructive interference effect for the generated radiation. However, in the case of subwavelength structures, the typical propagation distance of light is generally insufficient to lead to powerful in-phase interactions.

Instead, high third order susceptibility and electric field enhancement are required to improve the efficiency of THG in nanometer scale. The third order nonlinear polarization is proportional to the cube of the electric field amplitude[116].

$$P^{(3)}(t) = \varepsilon_0 \chi^{(3)} E(t)^3 \tag{2.40}$$

where $P^{(3)}$ is the third order nonlinear polarization, ε_0 is the permittivity of free space, $\chi^{(3)}$ is the third order nonlinear optical susceptibility, and E is the electric field amplitude. For simplicity, only the scalar quantities have been taken in Eq (2.40). In the simple case that the applied electric field is monochromatic, $E(t) = E\cos\omega t$, eq. (2.40) is substituted as follows,

$$\begin{aligned} P^{(3)}(t) &= \frac{1}{4}\varepsilon_0 \chi^{(3)} E^3 \cos 3\omega t + \frac{3}{4}\varepsilon_0 \chi^{(3)} E^3 \cos \omega t \\ &= \varepsilon_0 \chi^{(3)}(3\omega; \omega, \omega, \omega) E^3 \cos 3\omega t + \varepsilon_0 \chi^{(3)}(\omega; \omega, -\omega, \omega) E^3 \cos \omega t \end{aligned} \tag{2.41}$$

The first term in eq. (2.41) corresponds to the third harmonic generation, whereas the second describes a nonlinear contribution to the refractive index. This clearly shows that the third order harmonic generation is a function of the third order susceptibility of $\chi^{(3)}(3\omega;\omega, \omega, \omega)$ and the electric field amplitude E. On the other hand, the second term in eq. (2.41) induces a change in the refractive index of a material proportional to E^2, which is known as optical Kerr effect[85].

As for the third order susceptibility, an empirical rule, which is known as the generalized Miller's rule, correlates the third order susceptibility to the linear susceptibility as follows[116].

$$\chi^{(3)}(3\omega; \omega, \omega, \omega) = A\chi^{(1)}(\omega)^3 \tag{2.42}$$

where A is a constant often assumed to be frequency and material independent. Therefore, materials which have a high linear susceptibility $\chi^{(1)}$, which is related to the permittivity and refractive index, would possess a high third order susceptibility for efficient third harmonic generation.

In this context, metallic nanoantennas exciting LSPRs have been intensely investigated, not only due to their ability to highly confine the incident electric field, but also due to the high third-order susceptibilities of metals, which enables, in principle, excellent THG performance[63,64,116–119]. Nevertheless, since the skin depth of conductors is

generally small and, hence, electric fields almost do not penetrate inside their volumes, any third-order nonlinear effect from metals results strongly reduced. That is why, to further enhance the THG process, plasmonic nanostructures have been combined with non-metallic nanometer-scaled nonlinear materials. For example, by placing an ITO nanoparticle at the hot spot of a metallic nanodimer, its TH efficiency has been shown to increase by up to six orders of magnitude[120–122]. But still, the inherent confinement of the electric field by plasmonic nanostructures strongly restricts the amount of nonlinear material that can be excited, highly limiting the overall TH conversion efficiency that can be attained. Moreover, the absorption of light by metals is relatively large at typical operation wavelengths in the visible and NIR range, leading not only to a reduction in the nonlinear performance, but also to the generation of undesired heat that may damage the structure or shift the resonance wavelength because of changes in refractive indices of the nanoparticle and surrounding medium[41,95,123].

These limitations of plasmonic nanoparticles for efficient nonlinear THG prompted the studies of nanoantennas made of high refractive index dielectrics, such as Si, germanium and GaP, for an alternative unit[49,51,52,62]. At their Mie resonances, dielectric nanoantennas can highly enhance electric and magnetic fields within or around the dielectrics without considerable energy losses[55,56,58,59]. Moreover, from the generalized Miller's rule as detailed in eq. (2.42), a high refractive index material implies a high third order nonlinear susceptibility medium, making the dielectric nanoantenna a key element for THG processes[60,61]. Furthermore, the size of enhanced field regions produced by Mie resonances in dielectric nanoantennas can highly exceed that corresponding to plasmonic modes in metallic nanostructures, enabling THG from relatively large volumes, boosting the nonlinear effect[60]. These advantages of high-index dielectric nanoantennas have raised the THG conversion efficiency up to 0.001 % in the nanometer scale[87,88], making high-index dielectric nanoantennas a highly respectable candidate for the realization of nonlinear optical nanodevices.

.

Chapter 3

Methods

3.1. Simulations and modellings

3.1.1. Analytical dipole-dipole model

As addressed in Section 2.2, the electric and magnetic dipolar resonances of a single dielectric spherical nanoparticle can be exactly described by Mie theory[98]. To apply this theoretical analysis to dimers of dielectric nanoparticles, an analytical dipole-dipole model, as detailed in ref[50], is employed. We modify this model, which was originally developed for symmetric dimers, to analyze the excited modes of asymmetric dimers.

The electromagnetic response of high-index dielectric spheres can be replaced by their electric and magnetic dipoles when the dimension of the sphere is much smaller than the wavelength of light. Here we consider a simple case under the plane wave illumination, which is electrically polarized along the dimer axis (y) and propagates towards the z-direction.

$$\mathbf{E}_i(\mathbf{r}) = E_0 \exp(ikz)\mathbf{u}_y \tag{3.1}$$

$$\mathbf{H}_i(\mathbf{r}) = -\frac{E_0}{Z} \exp(ikz)\mathbf{u}_x \tag{3.2}$$

where $Z = (\mu_0\mu_m/(\varepsilon_0\varepsilon_m))^{1/2}$ is the impedance in the medium (μ_0 and ε_0 are the permeability and permittivity of free space, μ_m and ε_m are the relative permeability and permittivity of the medium). The Mie coefficients a_1 and b_1 of the dielectric nanosphere can be calculated by eq. (2.17) and (2.18) in Chapter 2.2.

In the case that there is no interaction between the two spheres, electric and magnetic dipolar polarizabilities are calculated using these coefficients as $\alpha_e = (6\pi i/k^3)a_1$ and $\alpha_m = (6\pi i/k^3)b_1$. The electric (**p**) and magnetic (**m**) dipolar moments are given by

$$\mathbf{p} = \varepsilon_0\varepsilon_m\alpha_e\mathbf{E}_i \tag{3.3}$$

$$\mathbf{m} = \alpha_m \mathbf{H}_i \tag{3.4}$$

Total field is the sum of the incident and scattered filed. Scattered field from the dimer can be calculated with the following equations[50].

$$\mathbf{E}_{\text{scat}}(\mathbf{r}) = \sum_{j=1,2} \left(\frac{k^2}{\varepsilon_0 \varepsilon_m} \vec{\mathbf{G}}_{\text{E}}(\mathbf{r} - \mathbf{r}_j) \cdot \mathbf{p}_j + iZk^2 \vec{\mathbf{G}}_{\text{M}}(\mathbf{r} - \mathbf{r}_j) \cdot \mathbf{m}_j \right) \tag{3.5}$$

$$\mathbf{H}_{\text{scat}}(\mathbf{r}) = \sum_{j=1,2} \left(-i \frac{1}{Z} \frac{k^2}{\varepsilon_0 \varepsilon_m} \vec{\mathbf{G}}_{\text{M}}(\mathbf{r} - \mathbf{r}_j) \cdot \mathbf{p}_j + k^2 \vec{\mathbf{G}}_{\text{E}}(\mathbf{r} - \mathbf{r}_j) \cdot \mathbf{m}_j \right) \tag{3.6}$$

$$\vec{\mathbf{G}}_{\text{E}}(\mathbf{r}) \cdot \mathbf{p} = \left\{ \left(1 + \frac{i}{kr} - \frac{1}{k^2 r^2} \right) \mathbf{p} + \left(-1 - \frac{3i}{kr} + \frac{3}{k^2 r^2} \right) (\mathbf{u}_r \cdot \mathbf{p}) \mathbf{u}_r \right\} g(r) \tag{3.7}$$

$$\vec{\mathbf{G}}_{\text{M}}(\mathbf{r}) \cdot \mathbf{p} = (\mathbf{u}_r \times \mathbf{p}) \left(i - \frac{1}{kr} \right) g(r) \tag{3.8}$$

$$g(r) = \frac{e^{ikr}}{4\pi r} \tag{3.9}$$

where j = 1,2 corresponds to each of the particles forming the dimer, $\vec{\mathbf{G}}_{\text{E}}$ and $\vec{\mathbf{G}}_{\text{M}}$ are the electric and magnetic dyadic Green's functions, respectively, and $g(r)$ is the scalar Green's function[2,98,124].

In the dimer case, each dipole is affected by electromagnetic fields generated from other dipoles excited in the other particle. Hence, electric and magnetic dipoles excited in the dimer are calculated by coupled dipole models[50]

$$\begin{aligned} \mathbf{p}_1 = {} & \varepsilon_0 \varepsilon_m \alpha_e \mathbf{E}_i(\mathbf{r}_1) + \alpha_e k^2 \vec{\mathbf{G}}_{\text{E}}(\mathbf{r}_1 - \mathbf{r}_2) \cdot \mathbf{p}_2 \\ & + iZ \varepsilon_0 \varepsilon_m \alpha_e k^2 \vec{\mathbf{G}}_{\text{M}}(\mathbf{r}_1 - \mathbf{r}_2) \cdot \mathbf{m}_2 \end{aligned} \tag{3.10}$$

$$\mathbf{m}_1 = \alpha_m \mathbf{H}_i(\mathbf{r}_1) - i \frac{\alpha_m}{Z} \frac{k^2}{\varepsilon_0 \varepsilon_m} \vec{\mathbf{G}}_{\text{M}}(\mathbf{r}_1 - \mathbf{r}_2) \cdot \mathbf{p}_2 + \alpha_m k^2 \vec{\mathbf{G}}_{\text{E}}(\mathbf{r}_1 - \mathbf{r}_2) \cdot \mathbf{m}_2 \tag{3.11}$$

$$\mathbf{p}_2 = \varepsilon_0 \varepsilon_m \alpha_e \mathbf{E}_i(\mathbf{r}_2) + \alpha_e k^2 \vec{\mathbf{G}}_{\text{E}}(\mathbf{r}_2 - \mathbf{r}_1) \cdot \mathbf{p}_1 \tag{3.12}$$

$$+iZ\varepsilon_0\varepsilon\alpha_e k^2 \overleftrightarrow{\mathbf{G}}_{\mathrm{M}}(\mathbf{r}_2-\mathbf{r}_1)\cdot\mathbf{m}_1$$

$$\mathbf{m}_2=\alpha_m\mathbf{H}_i(\mathbf{r}_2)-i\frac{\alpha_m}{Z}\frac{k^2}{\varepsilon_0\varepsilon_m}\overleftrightarrow{\mathbf{G}}_{\mathrm{M}}(\mathbf{r}_2-\mathbf{r}_1)\cdot\mathbf{p}_1+\alpha_m k^2\overleftrightarrow{\mathbf{G}}_{\mathrm{E}}(\mathbf{r}_2-\mathbf{r}_1)\cdot\mathbf{m}_1 \tag{3.13}$$

The first terms in the right side of these equations derive from the electromagnetic response of the system to the incident field. The second terms are attributed to the excitation by the electric dipoles of the other particle[125]. The last terms are given by the magnetic dipoles in the other particle[125]. Note that we are treating only electric and magnetic dipoles. Therefore, the problem of the light scattered from a dimer has been reduced to this coupled dipole model only in the case that the particle is small enough in comparison with the wavelength of excitation[50].

When the dimer is illuminated by an incident plane wave along the z axis with the electric field polarized along the y axis and magnetic field along the x axis, the Green's function can be expressed as[50]

$$\overleftrightarrow{\mathbf{G}}_{\mathrm{E}}(\mathbf{r}_1-\mathbf{r}_2)\cdot\mathbf{u}_x=\left(1+\frac{i}{kD}-\frac{1}{k^2D^2}\right)g(D)\mathbf{u}_x\equiv-g_{xx}\mathbf{u}_x \tag{3.14}$$

$$\overleftrightarrow{\mathbf{G}}_{\mathrm{M}}(\mathbf{r}_1-\mathbf{r}_2)\cdot\mathbf{u}_x=-\left(i-\frac{1}{kD}-\right)g(D)\mathbf{u}_z\equiv g_{zx}\mathbf{u}_z \tag{3.15}$$

$$\overleftrightarrow{\mathbf{G}}_{\mathrm{E}}(\mathbf{r}_1-\mathbf{r}_2)\cdot\mathbf{u}_z=\left(1+\frac{i}{kD}-\frac{1}{k^2D^2}\right)g(D)\mathbf{u}_z\equiv-g_{xx}\mathbf{u}_z \tag{3.16}$$

$$\overleftrightarrow{\mathbf{G}}_{\mathrm{M}}(\mathbf{r}_1-\mathbf{r}_2)\cdot\mathbf{u}_x=\left(i-\frac{1}{kD}-\right)g(D)\mathbf{u}_x\equiv-g_{zx}\mathbf{u}_x \tag{3.17}$$

$$\overleftrightarrow{\mathbf{G}}_{\mathrm{E}}(\mathbf{r}_1-\mathbf{r}_2)\cdot\mathbf{u}_y=\left(-\frac{2i}{kD}-\frac{2}{k^2D^2}\right)g(D)\mathbf{u}_y\equiv g_{yy}\mathbf{u}_y \tag{3.18}$$

$$\overleftrightarrow{\mathbf{G}}_{\mathrm{M}}(\mathbf{r}_1-\mathbf{r}_2)\cdot\mathbf{u}_z=0 \tag{3.19}$$

where $D = |\mathbf{r}_1 - \mathbf{r}_2|$. Due to $\mathbf{r}_1 - \mathbf{r}_2 = -(\mathbf{r}_2 - \mathbf{r}_1)$, the electric and magnetic dipoles in the nanoparticle $j = 2$ can be calculated by substituting the Green's functions above as follows

$$\overleftrightarrow{\mathbf{G}}_{\mathrm{E}}(\mathbf{r}_1 - \mathbf{r}_2) = \overleftrightarrow{\mathbf{G}}_{\mathrm{E}}(\mathbf{r}_2 - \mathbf{r}_1) \tag{3.20}$$

$$\overleftrightarrow{\mathbf{G}}_{\mathrm{M}}(\mathbf{r}_1 - \mathbf{r}_2) = -\overleftrightarrow{\mathbf{G}}_{\mathrm{M}}(\mathbf{r}_2 - \mathbf{r}_1) \tag{3.21}$$

Thus, each component of the electric and magnetic dipoles in the two particles is given by solving following equations.

$$p_{1y} = \varepsilon_0 \varepsilon_m \alpha_e E_0 + \alpha_e k^2 g_{yy} p_{2y} \tag{3.22}$$

$$p_{2y} = \varepsilon_0 \varepsilon_m \alpha_e E_0 + \alpha_e k^2 g_{yy} p_{1y} \tag{3.23}$$

$$p_{1z} = -\alpha_e k^2 g_{xx} p_{2z} + i\varepsilon_0 \varepsilon_m \alpha_e Z k^2 g_{zx} m_{2x} \tag{3.24}$$

$$p_{2z} = -\alpha_e k^2 g_{xx} p_{1z} - i\varepsilon_0 \varepsilon_m \alpha_e Z k^2 g_{zx} m_{1x} \tag{3.25}$$

$$m_{1x} = -\frac{\alpha_m}{Z} E_0 + i \frac{\alpha_m}{Z} \frac{k^2}{\varepsilon_0 \varepsilon} g_{zx} p_{2z} - \alpha_m k^2 g_{xx} m_{2x} \tag{3.26}$$

$$m_{2x} = -\frac{\alpha_m}{Z} E_0 - i \frac{\alpha_m}{Z} \frac{k^2}{\varepsilon_0 \varepsilon} g_{zx} p_{1z} - \alpha_m k^2 g_{xx} m_{1x} \tag{3.27}$$

The extinction cross section can be then calculated by considering the imaginary part of the excited dipoles in the forward direction:

$$\sigma_{ext} = \frac{4\pi}{k E_0} \mathrm{Im}\left\{ \frac{k^2}{4\pi \varepsilon_0 \varepsilon} (p_{1y} + p_{2y}) - \frac{Z k^2}{4\pi} (m_{1x} + m_{2x}) \right\} \tag{3.28}$$

The far field distribution of the scattered field intensity per unit area is calculated from the scattered field $\mathbf{E}_{\mathrm{scat}}(\mathbf{r})$ and $\mathbf{H}_{\mathrm{scat}}(\mathbf{r})$ at $r \to \infty$,

$$S(\theta, \phi) = \lim_{r \to \infty} \frac{1}{2} \mathrm{Re}(\mathbf{E}_{scat}(r) \times \mathbf{H}_{scat}(r)^*) \tag{3.29}$$

Equations (3.1) – (3.29) were coded and calculated in Matlab.

3.1.2. Finite-difference time-domain method

Theoretical analyses based on Mie theory and the analytical dipole-dipole model are useful for the detailed investigations of the resonances of ideal spherical nanoparticles. However, computational simulations with a large number of numerical calculations would be required to explore the optical responses of complex single nanostructures, such as ring-disk hetero structures, or periodic arrays of nanostructures. One of the most used numerical simulation methods is the finite-difference time-domain (FDTD) method[126]. In FDTD simulations, electric and magnetic fields are calculated straightforwardly by solving Maxwell equations which are discretized into differential equations as a function of space and time.

In this section, we briefly revisit the basic principles of the FDTD method. Maxwell equations are described as follows when combined with Ohm's law,

$$\nabla \times \mathbf{E} = -\mu \frac{\partial \mathbf{H}}{\partial t} \tag{3.30}$$

$$\nabla \times \mathbf{H} = -\varepsilon \frac{\partial \mathbf{E}}{\partial t} + \sigma \mathbf{E} \tag{3.31}$$

Time derivatives of electric and magnetic fields can be discretized in terms of time in the following equations.

$$\left.\frac{\partial \mathbf{E}}{\partial t}\right|_{t=\left(\left(n-\frac{1}{2}\right)\Delta t\right)} = \frac{\mathbf{E}^{n} - \mathbf{E}^{n-1}}{\Delta t} \tag{3.32}$$

$$\left.\frac{\partial \mathbf{H}}{\partial t}\right|_{t=(n\Delta t)} = \frac{\mathbf{H}^{n+\frac{1}{2}} - \mathbf{H}^{n-\frac{1}{2}}}{\Delta t} \tag{3.33}$$

Inserting eq. (3.32) and (3.33) into (3.30) and (3.31) yields

$$\frac{\mathbf{E}^n - \mathbf{E}^{n-1}}{\Delta t} = -\frac{\sigma}{\varepsilon}\mathbf{E}^{n-\frac{1}{2}} + \frac{1}{\varepsilon}\nabla\times\mathbf{H}^{n-\frac{1}{2}} \tag{3.34}$$

$$\frac{\mathbf{H}^{n+\frac{1}{2}} - \mathbf{H}^{n-\frac{1}{2}}}{\Delta t} = -\frac{1}{\mu}\nabla\times\mathbf{E}^n \tag{3.35}$$

$$\mathbf{E}^{n-\frac{1}{2}} = \frac{\mathbf{E}^{n-1} + \mathbf{E}^n}{2} \tag{3.36}$$

The discretization of fields in terms of space coordinates are carried out by dividing calculation regions into small Yee cells (Figure 3.1). Electric and magnetic fields are calculated on the edges of the cells and at the centre of the faces of the cells, respectively, which can fulfill the discretized Maxwell equations (3.34) and (3.35). FDTD method provides us the solution of Maxwell equations, electric and magnetic fields, at any Yee cell and at any discretized time. This method is convenient to analyze optical phenomena, such as the enhancement of near field and far field scattering properties.

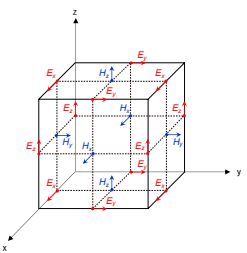

Figure 3.1. A Yee cell with electric and magnetic field elements assigned in the positions to calculate the propagation of electromagnetic waves in FDTD method.

The FDTD method is generally robust and straightforward as Maxwell equations are directly solved without any complicated assumptions. This feature also causes some disadvantages; for example, fine grids are required to investigate configurations with small features, such as a narrow gap in dimers, resulting in huge computational region

and long calculation time. However, obtained results are usually trustful given the good convergence is achieved. Since the studies in this thesis range widely from light scattering to nonlinear harmonic generations from nanoantennas, we adopted the FDTD method for a numerical simulation to analyze obtained optical effects. A commercially available FDTD solver Lumerical was used for numerical simulations in this thesis.

3.2. Sample fabrications

All nanosturctures experimentally studied in this thesis were fabricated by dry-etching process based on electron beam lithography (EBL) and reactive ion etching (RIE) techniques. In comparison with other methods, such as a laser ablation technique[127], chemical syntheses[128,129], laser printing[130] and nano-imprinting technique[131], the top-down method using EBL and RIE enables the fabrication of finely controlled nanometer scale dielectric structures on a substrate.

3.2.1. Electron beam lithography and reactive ion etching

In this section, we shortly describe the basic nanofabrication techniques; EBL and RIE. EBL is a lithography method using an electron beam to expose a pattern onto an electron-sensitive material called a resist. The chemical property of the resist is changed either soluble or insoluble to developer solution by the electron beam exposure, providing the pattern defined by soluble and insoluble regions. Since the energy of electron is high enough to have very small wavelength (e.g., 10 ekV electron beam has a wavelength of 0.01 nm), EBL can draw the pattern with nanometer scale resolution. RIE is a dry etching process using chemically reactive plasma. The chemical plasma can remove the material selectively depending on the reactivity between them. For instance, the etch rate ratio of chemical plasma generated by the mixture of SF_6 and CHF_3 gases is significantly high between Si and Cr; Si can be etched down easily by this chemical plasma, while Cr can remain stable. This selectivity enables the patterning of Si nanostructures with a Cr mask.

3.2.2. Fabrication of all-dielectric nanostructures

All-dielectric Si nanostructures, which are studied in Chapters 4, 5 and 6, were fabricated using EBL and RIE techniques. For samples in Chapter 4 and 5, we used a

commercially available epitaxially grown Si-on-sapphire substrate with a polished backside. For the samples in Chapter 6, a thin layer of amorphous Si deposited on a silica substrate by plasma-enhanced chemical vapor deposition was used to match the refractive indices of the substrate and prism in the experimental setup. The refractive indices of the Si used in this thesis were measured by ellipsometry technique and shown in Figure 3.2. The epitaxially grown Si thin layer on the sapphire substrate showed the real and imaginary part of refractive index as high as single crystalline Si[45], confirming the capability of generating electric and magnetic resonances when it's patterned into high-index dielectric nanostructures. The real part of the refractive index of the amorphous Si on silica substrate, on the other hand, was slightly smaller than the crystalline Si (around 3.2 at $\lambda = 650$ nm). However, this refractive index is high enough as to excite electric and magnetic resonance, as nanostructures of refractive index larger than 2 reportedly showed resonances on a silica substrate[57]. Therefore, we confirmed that both the Si samples were suitable for our studies in which high-index dielectric nanostructures provide with electric and magnetic resonances.

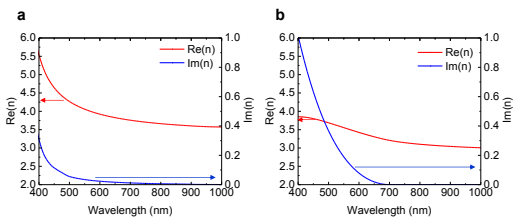

Figure 3.2. Real and imaginary parts of the refractive index of the commercial crystalline Si on sapphire substrate (a) and the deposited amorphous Si on silica substrate (b).

In the fabrication process, which is summarized in Figure 3.3, the thin Si layers were first etched down to a desirable thickness by RIE using SF_6 and CHF_3 gases. The substrates were coated with positive tone resist PMMA (poly (methyl methacrylate)) and baked at 180 °C for 2 minutes. Spin-coating technique was used, providing the PMMA layer of 220 nm thickness, which was confirmed by a stylus profiler. Electron beam (20 ekV, 10 μm aperture) was exposed onto the PMMA according to the pattern prepared by a CAD program. The electron beam exposure was followed by a development procedure

with MIBK (methyl isobutyl ketone) : IPA (isopropanol) = 1 : 3 solution for 70 seconds. Then a 40 nm Cr thin layer was deposited by thermal evaporation, followed by lift-off process with acetone solution. Subsequently the pattern was transferred to the Si layers using the RIE process with the Cr nanostructures as a mask. The Cr mask was removed with commercial Cr etchant solution to obtain the final sample.

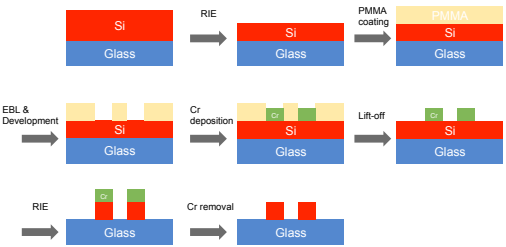

Figure 3.3. Fabrication procedure of all-dielectric nanostructures based on EBL and RIE technique.

3.2.3. Fabrication of Au – Si hybrid structures

Fabrication of hybrid nanostructures of Au and Si (used in Chapter 7) were conducted by a similar procedure to the all-dielectric ones. A schematic illustration is shown in Figure 3.4. First the Si nanostructures were fabricated using Si on sapphire substrates by the method above. After the fabrication of the Si nanodisk, the second PMMA layer was coated on the substrate, which had the thickness of 300 nm. The thicker PMMA layer was used to make the layer as flat as possible even in the presence of Si nanostructures on the substrate. The PMMA layer was treated by the same EBL procedures. The position of the second PMMA mask was aligned to the Si nanodisk using cross-shaped markers enabling the fabrication of hetero-material structures in 20 nm resolution. A Au layer was then thermally evaporated onto the substrate, and the following lift-off process provided final hybrid samples.

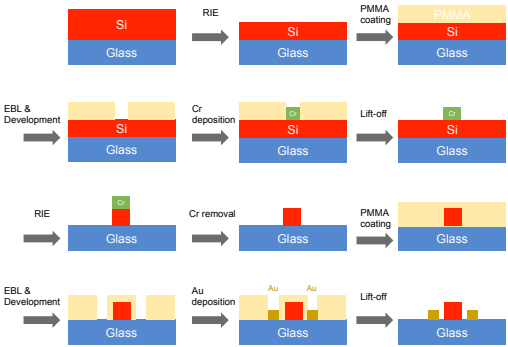

Figure 3.4. Fabrication procedure of Si – Au hybrid nanostructures based on EBL and RIE technique.

3.3. Optical measurements

Despite that the scattering efficiency of the resonant nanoantenna is usually large, optical signals from small nanostructures are often quite weak and have some noise hindering detailed and precise analyses. This often forces researchers to build their own optical setups to obtain sufficient signals from the nanostructures and to analyze it correctly. The required systems depend on the purpose of the optical measurements. In this section, we introduce the optical measurement setups that we have built up for each project.

3.3.1. Dark field optical spectroscopy for measuring forward and backward light scattering from nanoantennas

In Chapter 4, we discuss light scattering towards forward or backward direction from dielectric nanoantennas. Dark field microscopy is a suitable technique to collect the scattered field from individual nanoantennas. For that purpose, we developed an optical

dark field measurement system equipped with a microscope (Nikon, Ti-U), photon counter and spectrometer, as shown in Figure 3.5. The incident light of the Xe lamp was illuminated from a dark field objective (Nikon LU Plan ELWD 100x NA0.80) with an incident angle θ_i = 60-70°. The incident light was polarized parallel to the dimer axis by a linear polarizer placed on the light path. The polarization direction was confirmed by inserting another polarizer right over the fabricated sample. In the case of forward scattering, another dark field objective set below the sample collected the scattered field. Backward scattering was detected by the same dark field objective used for illumination. The NA of the objectives for light illumination and collection was 0.8, which corresponds to the maximum collection angle θ_s = 53°. The collected light was collimated by a set of lenses and went through a fiber with a 50 μm pinhole. In the ideal case, this pinhole and the magnification of the used objective provides 500 nm resolution in the collection area given the wavelength of interest is short enough. The scattered light was then divided into two paths either to the photon counter or spectrometer by a flipping mirror. The position of the measurement was determined by maximizing the signal collected by the photon counter. Finally, the spectrum of the scattered field from single nanoantennas was obtained with the spectrometer. The normalization of the measured signal intensity was carried out using a commercially available flat pellet of barium sulfate fine powder which can generate reflection close to the Lambertian pattern.

The backward scattering setup is also used in Chapter 5 to confirm the presence of electric and magnetic resonances of fabricated dielectric nanoantennas.

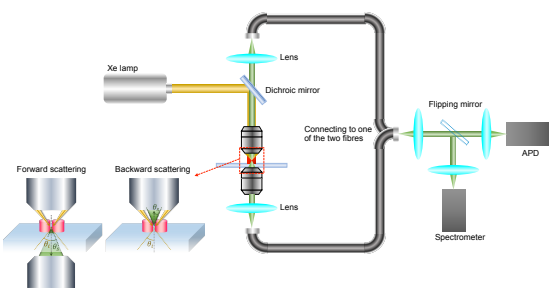

Figure 3.5. Schematic image of the dark field optical measurement setup for the forward scattering and backward scattering.

3.3.2. Fourier transform infrared spectroscopy for measuring transmission and reflection of metasurfaces

When the spectrum of interest is in the IR region, Fourier transform infrared (FTIR) spectroscopy is a useful method to measure optical responses of samples. In comparison with an ordinary dispersive spectroscopy which sweeps monochromatic light in a certain range, FTIR spectroscopy uses a broadband light source. Then the frequencies of the incident light can be altered by using Michelson interferometer, in which one of two mirrors after a beam splitter moves precisely, causing the difference between the optical paths via the two mirrors. This optical path difference results in interference of light between the two optical paths, and light intensity of incident light can vary by moving the mirror, generating an optical interferometry which can be converted to a spectrum by Fourier transformation.

In Chapter 5, we investigate the transmission and reflection of dielectric metasurfaces using the FTIR technique. An FTIR microscope (Bruker Infinion) with 35× Cassegrain objectives was used to collect the transmission and reflection signals from dielectric metasurfaces. The objective has a weighted-average incident and collection angle of approximately 25°. An aperture was used for all samples to limit the collection area to 50 × 50 μm^2, so that dielectric metasurfaces fabricated by the EBL and RIE techniques can be observed. The transmission and reflection signals from the samples were normalized by the transmission in air and the reflection from a Au mirror under the same settings, respectively.

3.3.3. Back focal plane technique combined with prism coupling for measuring scattering patterns along the substrate

The back focal plane (BFP) imaging technique is a useful tool to characterize the directionality of the electromagnetic field of light scattered from nanoantennas, as the position of pixels in the BFP images corresponds to the light propagation angle[21,22,132]. BFP techniques reported to date for measuring the scattering patterns from nanoparticles were, in general, designed to monitor the scattered field propagating towards the substrate with the incident illumination normal to the substrate[21,22,132,133]. That setup has not yet been used to investigate the scattering light in a plane along the substrate. This is the main objective in Chapter 6 due to its importance for applications such as optical nanocircuitry or efficient light guiding in a medium on the substrate.

Here, a specially designed BFP imaging setup combined with prism coupling was built to measure the scattering profiles parallel to the substrate. This system provides an evanescent wave to excite the nanoantenna and allows us to explore the distribution of the scattering field for light travelling along the substrate. A schematic of the experimental setup is shown in Figure 3.6. A Yb:KGW PHAROS laser system was used as the pump for an ORPHEUS collinear optical parametric amplifier with a LYRA wavelength extension option (Light Conversion Ltd, pulse duration 200 fs, repetition rate 100 kHz). The incident laser was directed towards the nanoantenna through the silica substrate that was combined with the silica prism. The grazing incident light, which was set at an angle of 80°, resulted in total reflection at the interface between the silica substrate and air, generating an evanescent wave to excite the nanoantenna. Light scattered from the nanoantennas was collected by an objective (Nikon CFI Plan Fluor 100x NA0.90). BFP images of the objective which corresponds to the scattering patterns were recorded with a CCD camera after being magnified by a set of two lenses (f = 75 mm and 175 mm) so that full BFP images can be collected in the sensor of the camera. There have been reported some measurement techniques to improve image quality of BFP from a single nanoparticle[134,135]. In this study, we used a pinhole to restrict the sample area and to collect signal from a single nanostructure. The enlarged view in Figure 3.6 also shows the

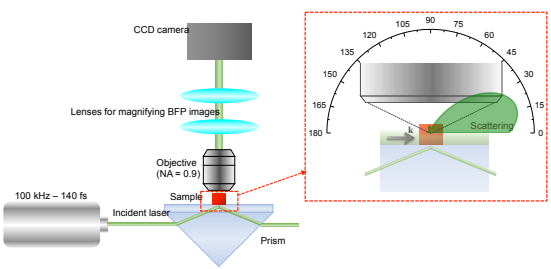

Figure 3.6. Schematic diagram of the optical setup for measuring the scattering along the substrate using a BFP imaging technique combined with a prism coupling. Evanescent field, which is generated by the total internal reflection at the interface of the substrate and air, propagates along the surface and decays exponentially into the air. The enlarged view on the right-hand side includes the scattering pattern calculated at $\lambda = 480$ nm, $\theta = 0\text{-}180°$ and $\varphi = 7°$.

scattering pattern calculated at λ = 480 nm, θ = 0-180° and φ = 7° (details will be described in Chapter 6). The scattered light has a certain lobe width extending from the surface of the substrate to at least 45°, which is detectable by the objective of NA0.90, corresponding to the collection of light up to 64°.

3.3.4. Nonlinear optical measurement with fs pulsed laser

Since the efficiency of nonlinear harmonic generations from optical nanoantennas is low, the measurement of the nonlinear optical effects requires a high-power laser and elaborate detecting system to measure small signals. To study third harmonic generation from metal-dielectric hybrid nanoantennas, which will be described in detail in Chapter 7, we built up the experimental setup illustrated in Figure 3.7. A pulsed Yb:KGW PHAROS laser system was used as the pump of a collinear optical parametric amplifier ORPHEUS with a LYRA wavelength extension option (Light Conversion Ltd., pulse duration of 180 fs, repetition rate of 100 kHz). The excitation beam was reflected by a short-pass dichroic mirror (Thorlabs DMSP805 for λ = 1300−1500 nm or DMSP1000 forλ = 1500−1800 nm)

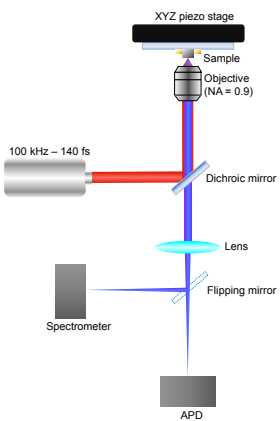

Figure 3.7. Schematic image of the experimental THG measurement setup.

and focused onto the sample with a 100× (NA = 0.90) air objective from Nikon, giving rise to an excitation spot of 1400 nm FWTM (full width at tenth of maximum). The third harmonic emission was collected in a backscattering configuration via the same objective and detected with an avalanche photodiode (MPD PDM series by Picoquant) for imaging or by a spectrograph (PI Acton SP2300 by Princeton Instruments) for spectral measurements. The sample was fixed to an XYZ piezo-scanner stage (Nano-Drive, Mad City Laboratories) to perform the scanning. The conversion efficiency was determined by directly measuring the collected TH emission power with a calibrated Si photodetector (Newport), and the excitation power with a germanium photodetector (Thorlabs), and then computing the ratio between the both. For <1 pW TH powers, values were calibrated by using the measured TH spectra.

Chapter 4

Unidirectional light scattering with high efficiency using asymmetric Si dimers

The Kerker conditions, as detailed in Chapter 2.3, were proposed first with an ideal magnetodielectric particle in 1983[71]. After high refractive index dielectric nanoparticles were found to excite both the electric and magnetic resonances, the unidirectional forward and backward scattering by the Kerker conditions have been theoretically and experimentally examined using these dielectric nanoparticles with the expectation that this could open the path to realize high-performance directional low-loss nanoantennas[72–76]. However, the scattering efficiency at the wavelength of the Kerker conditions is generally quite low for spherical particles. This is because spherical dielectric particles have the electric and magnetic resonances with considerably large spectral separation in terms of resonant wavelength and intensity, and the Kerker conditions are fulfilled far from the resonant peaks[73,74]. Heterodimer structures using Au and Si nanospheres were investigated to enhance the scattering intensity with high directionality, exploring the interference between broad and narrow-band hybrid modes; however, structures with metals still suffer from substantial ohmic losses[136]. These losses could cause not only the reduction in scattering efficiency but also substantial heat which is undesirable for many applications, such as spectroscopic techniques for heat-sensitive molecules[51,52]. A theoretical study on dielectric spheroids and core-shell particles has revealed that tuning the aspect ratio of the spheroid or the core radius of the core-shell particle can shift the electric and magnetic dipole modes to the same resonant wavelengths[137–139]. However, these structures are quite difficult to fabricate on the nanometer scale with fine precision. Dielectric nanodisks with low aspect ratio could be another possible candidate to obtain unidirectional forward scattering with high efficiency[76]. However, in order to optimize resonant intensity and peak width, only adjusting the aspect ratio of the structure itself would be insufficient. For instance, the precise control of refractive index of a substrate and surrounding media equal to 1.66 is reportedly required to attain high transmittance, which has been demonstrated only theoretically[77].

In this section, we investigate asymmetric dimer configurations of high-index

dielectric nanoparticles, Si in particular, as a novel solution to achieve directional scattering with high efficiency. The resonant wavelengths of dielectric nanostructures are tuneable by changing the dimension of the particles[55]. Also, previous studies revealed that dielectric dimers can offer strong coupling between the electric resonance excited in one particle and the magnetic one in the other if the two particles are placed close to each other[50,140]. This study will use a detailed theoretical analysis based on an asymmetric dimer of spherical Si nanoparticles, which is introduced in Chapter 3.1, to prove the concept of Kerker-like unidirectional forward scattering but with high scattering efficiency near the resonance. Furthermore, a practical configuration of a dimer of asymmetric Si nanodisks on a transparent substrate will be used to experimentally demonstrate highly efficient unidirectional forward scattering of visible light from the nanoantenna. We will also discuss a design to obtain a multi-wavelength or broadband response by adding more finely tuned nanoparticles. The dielectric nanoantennas introduced in this chapter could be a key unit constituting metasurfaces and nanometer scale devices such as efficient solar cells and optical sensors.

4.1. Theoretical study of asymmetric Si spherical dimer for highly efficient unidirectional forward scattering

4.1.1. Scattering Properties of an asymmetric Si dimer

We first numerically investigate an asymmetric dimer of Si spherical nanoparticles in air using the FDTD simulation method and the analytical dipole-dipole model to clarify whether the Kerker conditions can be achieved in the dimer case. Note that the spherical nanoparticles were used in this section since the full Mie theory can be applied, giving us the exact solutions of the resonant modes.

Figures 4.1 shows the numerical results of the scattering spectra towards forward and backward direction and their ratio (F/B ratio) for single and dimer configurations. Two Si spherical nanoparticles, whose diameters were 165 nm and 225 nm, were placed in air forming a dimer. For the theoretical analysis, we first used a separation distance of 5 nm to obtain strong coupling between the two particles. This dimer was illuminated by a plane wave polarized parallel to the dimer axis. Two broad peaks were observed around λ = 530 nm and 654 nm, and around λ = 660nm and 860nm in the scattering spectra of the

small and large single particle cases, which correspond to the electric and magnetic dipolar resonances of the small and large particles, respectively. The scattering peaks observed at shorter wavelengths than the dipolar modes were attributed to higher-order mode resonances. In the F/B ratio spectra of the single spheres, two peaks were observed at wavelengths shorter than the electric dipole resonance and longer than magnetic dipole resonance, at which the first Kerker condition was achieved. However, the forward scattering efficiency at those wavelengths was very low, as reported previously, since the first Kerker condition occurs away from the resonance peaks[73,74]. The asymmetric dimer structure, on the other hand, showed a distinct new peak in its F/B ratio spectrum around λ = 650 nm, at which the forward scattering presented a peak and backward scattering

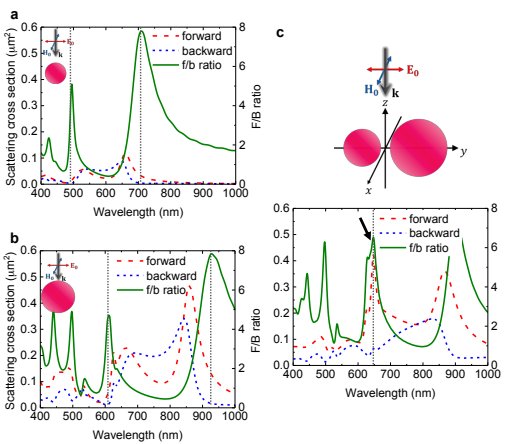

Figure 4.1. Configuration and results of the FDTD simulation. (a-c) Spectra of scattering cross section to the forward and backward direction and F/B ratio of the 165 nm diameter single sphere (a), the 225 nm diameter single sphere (b) and the dimer of these spheres (c). Insets are configurations used in the calculation.

was suppressed. This demonstrates unidirectional scattering to the forward direction with high scattering efficiency using the asymmetric dimer configuration. The wavelength showing this unidirectional scattering is close to the wavelength at which we observe the magnetic dipolar resonance in the small particle and the electric dipolar resonance in the large.

The other peaks in the F/B ratio spectra of the dimer configuration derive from the response of each individual particle; for example, the peak of F/B ratio at λ = 900 nm of the dimer structure agrees well with that at λ = 925 nm of the large single particle. The scattering efficiencies at these wavelengths, however, were low compared to the new peak around λ = 650 nm. Please note that we integrated the scattered filed throughout hemispheres in the forward and backward direction to calculate the scattering efficiencies and F/B ratio since this condition is close to the experimental demonstration described below. A previous theoretical work showed that a single Si nanodisk which has diameter of 620 nm and thickness of 220 nm exhibited more than 10^3 front to back ratio at NIR wavelengths[76]. However, that number was calculated with an ideal point dipolar source and considering a singular forward and backward direction point (0° and 180° respectively). When the structure was illuminated by a plane (or Gaussian) wave, and the scattered light was collected throughout both hemispheres in the far field, the nanodisk exhibited a F/B ratio of around 8. This F/B ratio is comparable with those of the single spheres and the dimer shown in Figure 4.1 given the same calculation method is used.

Figure 4.2a shows the radiation patterns of the scattered field on x-z plane at the wavelengths of maximum F/B ratios. The scattering intensity of the dimer in the 0° direction, which corresponds to direct forward scattering, was more than 10 times larger than for single spheres. This enhancement in intensity clearly showed the advantage of the asymmetric dimer which can fully utilize the scattering resonance for unidirectional forward scattering. A small fraction of scattering to the backward direction was also observed in the far-field distribution of the dimer, possibly due to the presence of magnetic quadrupoles excited near the electric dipolar response of the larger sphere. The far field patterns on y-z plane is shown in Figure 4.2b, where the high scattering intensity of the dimer was also confirmed.

The electric near field in the y-z plane was monitored at λ = 647 nm (Figure 4.3) to explore the resonances excited in the dimer. The typical rotation and oscillation of the displacement current, which correspond to the magnetic and electric resonances respectively, were observed in the small and large spheres. The electric resonance in the large particle shows not only a y-component but also a z-component, since an electric resonance along to the z-axis was induced by the interaction with the magnetic resonance

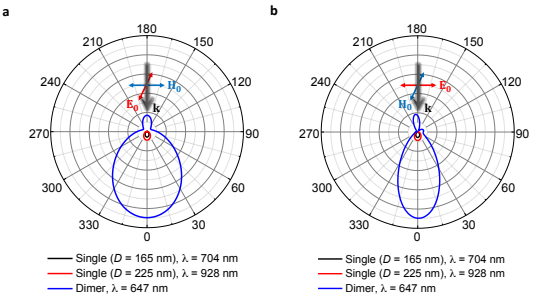

Figure 4.2. Scattering pattern in far field from the single spheres and dimer configuration projected in (a) x-z plane and (b) y-z plane.

of the small particle[50]. Intense confinement and enhancement of the electric field was generated in the gap, suggesting the presence of coupling between the electric and magnetic near-field dipolar resonances of each particle. The hot spot generated at the gap introduces another key advantage of this asymmetric dimer over the single disk configu-

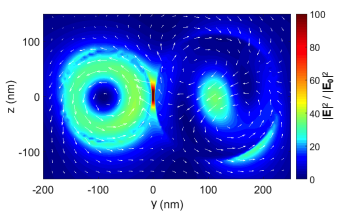

Figure 4.3. Electric field intensity and coupling between the resonances. Cross section of electric field intensity inside and near the dimer configuration at 647 nm illumination in the y-z plane. White arrows in the figure show the real part of electric field vectors at each calculation cell.

-ration. As reported[50–52,141,142], the hot spot of dielectric nanodimers can be applied to surface enhanced spectroscopic applications. In fact, we would expect that combining the highly efficient unidirectional forward scattering with the hot spot generated at the gap of the dimer could open up the path to highly sensitive spectroscopic applications in nanometer scale.

4.1.2. Theoretical investigation on the fulfilment of the first Kerker condition

To verify the achievement of the first Kerker condition, we analyzed the dimer configuration using the analytical dipole-dipole model described in detail in Chapter 3.1. The electric and magnetic dipoles excited perpendicular to the incident axis in the small (p_{1y} and m_{1x}) and large (p_{2y} and m_{2x}) nanoparticles contribute to the directional scattering along the incident axis. The first Kerker condition can be fulfilled when the Mie coefficients of electric and magnetic dipolar resonances are equal. The contribution of the electric and magnetic dipoles both in real and imaginary parts are calculated as follows,

$$\Re_e = \mathrm{Re}\left(\frac{1}{\varepsilon_0 \varepsilon_m}\left(p_{1y} + p_{2y}\right)\right) \tag{4.1}$$

$$\Re_m = -\mathrm{Re}\left(Z\left(m_{1x} + m_{2x}\right)\right) \tag{4.2}$$

$$\Im_e = \mathrm{Im}\left(\frac{1}{\varepsilon_0 \varepsilon_m}\left(p_{1y} + p_{2y}\right)\right) \tag{4.3}$$

$$\Im_m = -\mathrm{Im}\left(Z\left(m_{1x} + m_{2x}\right)\right) \tag{4.4}$$

where ε_0 is the vacuum permittivity, ε_m is the relative permittivity of the lossless media, and Z_0 is the vacuum impedance. In order to achieve the first Kerker condition, we need to satisfy following equations.

$$\Re_e = \Re_m \tag{4.5}$$

$$\Im_e = \Im_m \tag{4.6}$$

The real and imaginary part of the electric and magnetic dipolar resonances are plotted in Figure 4.4. The equations (4.5) and (4.6) were satisfied around 650 nm at which unidirectional forward scattering was observed in the FDTD numerical simulation. This agreement strongly suggests that the first Kerker condition was achieved with the asymmetric dimer configuration around 650 nm, at which the resonant scattering peak was also observed. Note that the analytical dipole-dipole model we used includes all the possible couplings such as electric-electric, magnetic-magnetic and electric-magnetic dipoles[9]. As shown in Figure 4.3, the electric-magnetic coupling was dominant and contributed most to the unidirectional forward scattering.

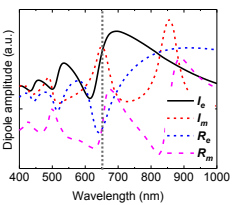

Figure 4.4. Theoretical analysis using the dipole-dipole model. The real and imaginary part of the electric and magnetic dipolar resonances excited in the dimer configuration calculated using the analytical dipole-dipole model.

4.1.3. Comparison with other structures showing unidirectional forward scattering

We now compare our asymmetric dimer configuration with a symmetric one, which exhibits a directional Fano-like resonance. This resonance can be obtained in the symmetric Si dimer structure due to the interaction between the sharp magnetic dipolar resonance and the electric dipolar resonance broadened by strong coupling between the two particles[143]. This strong coupling is possible only when the two particles are placed very close to each other[50]. The scattering and F/B ratio spectra of an asymmetric dimer of 165 nm and 225 nm diameter Si spherical nanoparticles and a symmetric dimer of 165 nm

diameter nanoparticles are shown in Figures 4.5a-d, for gap of 5 nm and 20 nm. With the smaller gap, the forward scattering cross section has a resonant peak at 647 nm for the asymmetric dimer, and at 657 nm for the symmetric one. The F/B ratio at the resonant maximum was almost the same between the two configurations. However, the situation changed significantly when the gap separation is increased to 20 nm. Both the forward scattering and the F/B ratio spectra of the asymmetric dimer showed little change even for the larger gap. In contrast, the maximum forward scattering efficiency of the symmetric dimer dropped by 12 %, and the forward scattering and F/B ratio peaks were shifted, showing more separation between them. Figure 4.5e shows the F/B ratio at the forward scattering maximum as a function of the gap separation distance for both dimers. As the gap increases, the F/B ratio of the symmetric dimer structure drops more rapidly than that of the asymmetric one. In addition, the maximum of forward scattering efficiency also showed a drop only in the case of symmetric dimer (Figure 4.5f). These differences in behavior with gap size are due to the fact that strong coupling is necessary to achieve a Fano resonance, owing to broadening of the electric mode. In contrast, the fulfilment of the Kerker condition requires only the overlap of the independent electric and magnetic resonances and, therefore, becomes less dependent on the coupling amplitude. These results would make the asymmetric dimer superior to the symmetric one for practical applications since gap sizes are not so critical in the Kerker case, enabling realization with less demanding lithography.

We note that the wavelength of the electric and magnetic resonances generated in dielectric particles is tuneable by changing the dimension of the nanoparticles. As an example, we show in Fig. 4.6 the calculated scattering and F/B spectra of a dimer with Si spherical particles of 110 nm and 150 nm diameter (Fig 4.6a), and of 225 nm and 310 nm diameter (Fig 4.6b), both with a gap separation of 5 nm. Efficient unidirectional forward scattering was confirmed as well around $\lambda = 480$ nm and $\lambda = 860$ nm, which were shifted from $\lambda = 650$ nm in the former dimer case as the dimensions of the nanoparticles were changed. Furthermore, the rescalability of highly efficient unidirectional scattering is not restricted to the optical regime. It is well known that the scattering properties of a dielectric object are fully scalable with identical properties as long as the size parameter of the object is the same[68,73,144]. Therefore, the concept introduced in this study of using asymmetric dimers could be used from the optical to the microwave regime.

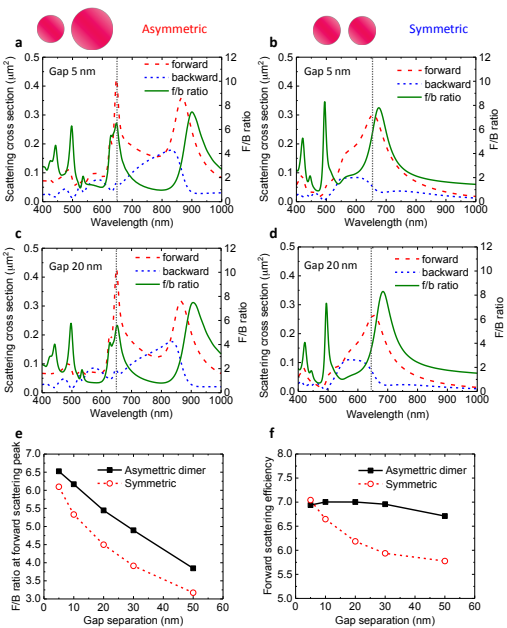

Figure 4.5. Comparison between Kerker-like asymmetric and Fano-like symmetric dimer structures. (a-b) Spectra of scattering cross section to the forward and backward direction and F/B ratio of the asymmetric dimer (a) and symmetric dimer (b) with the gap separation of 5 nm. (c-d) Spectra of the asymmetric dimer (c) and symmetric dimer (d) with the gap separation of 20 nm. (e-f) F/B ratio (e) and forward scattering efficiency (f) as a function of the gap separation of asymmetric (black, solid line, full square) and symmetric (red, broken line, open circle) dimers.

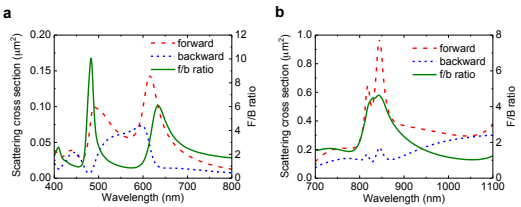

Figure 4.6. Scattering properties shifted to the boundaries of the visible regime. Spectra of scattering cross sections to the forward and backward directions and F/B ratio of the dimer using Si spheres of 110 nm and 150 nm diameter (a) and the dimer using Si spheres of 225 nm and 310 nm diameter (b).

4.2. Experimental demonstration of the unidirectional forward scattering with Si disk asymmetric dimer

4.2.1. Scattering properties of fabricated samples observed with dark field spectroscopy

We fabricated isolated Si nanodisks and Si nanodimers on transparent sapphire substrates using the lithography method described in detail in Chapter 3.3.1. Insets of Figures 4.7a-c show the SEM images of a fabricated nanodisk dimer and isolated single nanodisks. From the top side, the shape of the structures was almost an exact circle and the gap of the dimer was clear without any residuals. The lateral view of the fabricated dimer showed that the side wall of the disks vertically reached the surface of the substrate. The diameters of the disks were 125 nm and 155 nm for the small and large particles respectively, both with a thickness of 220 nm. These dimensions were suitable to study the overlap of the electric dipolar resonance of one particle and the magnetic resonance of the other, because a high aspect ratio favours the spectral separation between electric and magnetic dipolar resonances[79]. The gap of the dimer structure was designed as 20 nm, which is close to the resolution limit of our electron beam lithography equipment.

To experimentally confirm the directional forward scattering, we conducted nanoparticle dark field spectroscopy measurements for the single and dimer disks into the forward and backward scattering directions. The experimental setup is described in detail in Chapter 3.4.1. Note that the antennas were fabricated with a pitch of 5 μm between antennas, which was sufficient to ensure that scattering was collected from a single antenna at a time. In Figure 4.7, we show on the left-hand side the forward and backward scattering spectra obtained experimentally (Figures 4.7a-c). In Figures 4.7d-f, we compare them with the numerically simulated scattering spectra. The forward scattering spectra of the single disks have two resonant peaks at λ = 585 nm and λ = 623 nm for the small disk, and at λ = 642 nm and λ = 718 nm for the large one. The backward scattering spectra present peaks at λ = 613 nm and λ = 703 nm for the small and large disks, respectively, showing no clear dip around the wavelengths of the forward scattering peaks. However, in the case of the dimer, the spectra show the largest forward scattering peak around λ = 660 nm, where a clear suppression of the backward scattering was observed. This result shows that preferential forward scattering was achieved with high forward scattering efficiency only for the dimer configuration.

A numerical study based on the FDTD method was carried out to analyze and interpret the experimental findings (Figures 4.7d-f). The experimentally obtained scattering spectra agreed well with those numerically calculated. The spectra of the single disks presented high F/B ratios at wavelengths shorter than the electric dipolar resonances and longer than the magnetic ones. However, the directional forward scattering was achieved away from any resonant peaks and the forward scattering intensity was low, as well as in the single sphere case. In the asymmetric dimer case, in contrast, the peak of the forward scattering and the dip of the backward scattering were observed at the same wavelength around λ = 650 nm, leading to the high F/B ratio with strong forward scattering. These results showed that placing the two disks in a proximity to get strong coupling between the electric and magnetic dipolar resonance resulted in increasing the scattering efficiency at the same time in improving the F/B ratio.

Note that the calculated F/B ratio was lower than in the case of the sphere. The increase in the incident angle caused the reduction in the F/B ratio because disks on a substrate do not have the perfect symmetry that spheres in air have. The illumination from a wide incident angle, hence, could cause the distortion in the resonances, disturbing the coupling between the two nanoparticles. To verify and evaluate this, scattering spectra of Si dimer nanodisks on a sapphire substrate were calculated when changing the incident angle of the dark field source θ_i from 10 – 20° to 60 - 70° by 10°, and plotted the F/B ratio as a function of the maximum incident angle in Figure 4.8. When incident light is

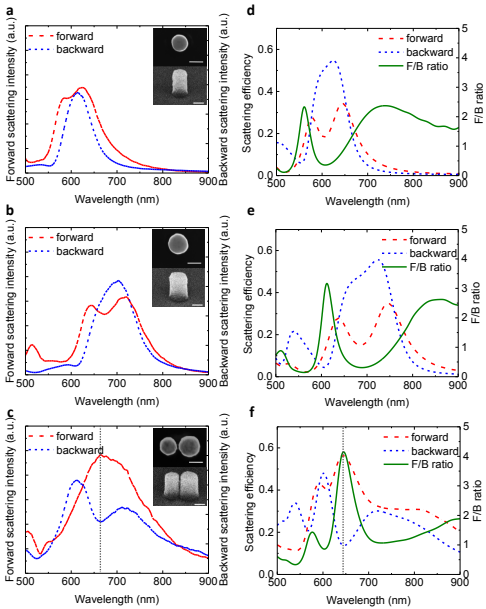

Figure 4.7. Experimentally measured scattering properties and comparison with simulations. (a-c) Scattering spectra to the forward and backward directions obtained in dark field single nanoantenna measurements of a single disk of 125 nm diameter (a), a single disk of 155 nm diameter (b) and the dimer of these two disks (c). (inset) SEM images of the fabricated samples with a scale bar of 100 nm. (d-f) Scattering spectra to the forward and backward directions and the F/B ratio calculated using the FDTD method.

normal or close to normal to the substrate, the F/B ratio increases significantly and can reach values of around 15. However, the F/B ratio was decreased as the incident angle increased.

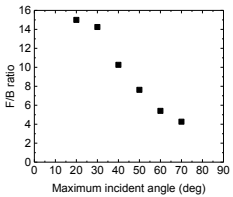

Figure 4.8. FDTD simulation results of maximum F/B ratio of scattered field from the dimer of Si nanodisks on a sapphire substrate as a function of the incident angle.

The experimental results only show minor differences when compared to the simulated results. The small differences would be attributed to the imperfectness of the fabricated structures. We conducted the same measurement with other dimers, which revealed small differences amongst each other in the shape of the spectra but the clear reproducibility of the unidirectional forward scattering and some vague peaks which agree well with the spectra obtained in the simulation (Figure 4.9).

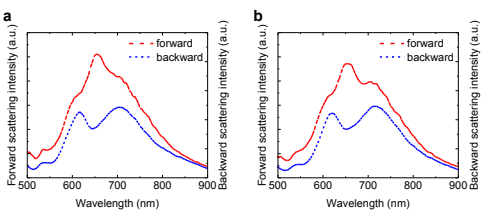

Figure 4.9. Scattering spectra of dimers obtained in experiments. (a,b) Spectra of the scattered field from the dimer measured with the single particle dark field spectroscopy measurements.

4.2.2. Verification of the suppression of the backward scattering and highly efficient unidirectional forward scattering

Backward scattering spectra of single and dimer disks are also compared in detail. In these experimental spectra (shown in Figure 4.10a), no dip is observed by just summing the spectra of each single disk, while a clear dip in the backward scattering appeared in the dimer spectrum around λ = 660 nm. The backward scattering spectra obtained in the simulation are plotted in Figure 4.10b, showing a similar tendency, and confirming that only the dimer structure exhibits a dip around 650 nm. This comparison suggests that the suppression of backward scattering and directional forward scattering can be obtained with the dimer configuration where strong coupling between the electric and magnetic dipole in each particle is observed. Note that, as it was obtained with the sphere case, the unidirectional forward scattering with the dimer of Si nanodisks on a substrate is also spectrally scalable. The electric and magnetic dipolar resonance can be easily tuned by changing the height and/or diameter of the disk shape[57].

The theoretical analysis and experimental demonstration with the dimer of nanospheres and high-aspect ratio nanodisks showed that the concept of using asymmetric dimer for unidirectional forward scattering with high efficiency is not restricted by the shape of the nanoparticles. The proposed idea could be applied to any arbitrary shapes including spheres, spheroids, high or low aspect ratio disks and rectangles.

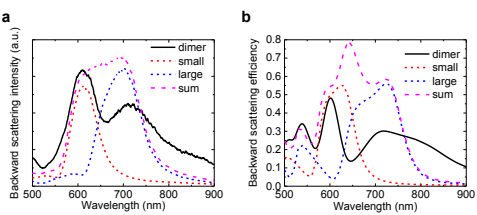

Figure 4.10. Comparison of experimental (a) and theoretical (b) scattering spectra to the backward direction of the single disks, the numerical sum of these two disks and the dimer configuration.

4.3. Oligomer nanostructures for multiwavelength forward scattering

4.3.1. Trimer of Si special nanoparticles showing unidirectional forward scattering at multiple wavelengths

The dimer configuration shows unidirectional forward scattering with high scattering efficiency at a certain wavelength that can be tuned with the particle size ratio. However, other applications such as solar cells and lighting instruments may require multi-wavelengths or broadband responses to improve their performance. In order to extend the wavelength range which shows unidirectional forward scattering, a trimer configuration was also explored. As an example, three Si spheres aligned in line with diameter of 165 nm, 225 nm, and 310 nm and a gap of 5 nm between each particle were investigated with FDTD simulations using incident light with polarization parallel to the trimer axis (Figure 4.11a). We chose these three diameters to obtain the overlapping between the electric and magnetic dipolar resonances at two different wavelengths in visible regime as shown in Figure 4.1c and 4.6b. Figure 4.11b shows forward and backward scattering spectra from the trimer and their F/B ratio. Large F/B ratios were obtained around λ = 650 nm and λ = 850 nm, where the forward scattering also showed

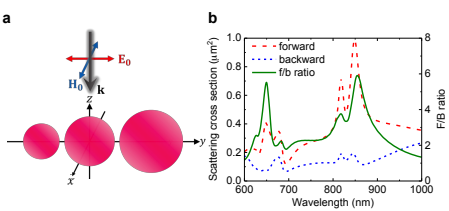

Figure 4.11. (a) Schematic image of the configuration used in calculation. (b) Scattering spectra of the trimer. Scattering cross section to the forward and backward direction and F/B ratio of the trimer using Si spheres of 165 nm, 225 nm and 310 nm diameter.

resonant peaks. This result shows that the proposed asymmetric configurations are not limited to one wavelength, but can be extend to multi-wavelengths resonances. Note that the multi-wavelength response obtained in this study is distinguishable from previous works where the oligomer configuration was used for highly directional nanoantennas based on Yagi-Uda like structures[67,145,146]. The oligomer proposed here consists of nanoparticles which are designed to provide multiple overlapping between electric and magnetic modes throughout the desired range of wavelength and, hence, could reach a broadband unidirectional forward scattering with high efficiency.

4.4. Summary

We revealed that highly efficient unidirectional forward scattering can be obtained using dimers of asymmetric Si nanoparticles (spheres or disks). Theoretical and numerical analyses of the spherical dimer showed that this configuration is capable of scattering light towards the forward direction selectively with high efficiency by fulfilling the first Kerker condition between the electric dipolar resonance excited in one particle and the magnetic in the other. This unidirectional scattering was experimentally confirmed by dark field scattering measurements with a dimer of asymmetric Si disks on a sapphire substrate. Our study shows that finely tuned and aligned dielectric nanoparticles act as low-loss nanoantennas which can route light with high efficiency, and hence boost the realization of practical metasurface and nanometer scale devices using optical subwavelength nanoantennas. Also, the presence of the hot spot, when coupled to the highly efficient unidirectional forward scattering demonstrated in this work, could help improve existing spectroscopic techniques.

Chapter 5

Polarization control over switching high transmission / reflection from dielectric metasurfaces

Metasurfaces are flat, ultrathin optical components artificially consisting of arrays of subwavelength optical nanoantennas[147,148]. Despite the light propagation distance being smaller than the wavelength, strong light-matter interactions mediated by the resonances can still offer the manipulation over the amplitude and phase of electromagnetic waves, providing interesting optical properties not found in materials in nature, such as negative refraction, beam shaping and perfect absorption[149–152]. The optical effects from metasurfaces, therefore, can be mainly determined by the resonant properties of the constituting nanostructures. Plasmonic nanoantennas made of noble metals have been commonly employed as nanoresonators for metasurfaces, due to their ability to confine and control the light even below the diffraction limit[15,92]. However, ohmic losses and consequentially undesirable heat are inevitable with plasmonic nanoparticles especially in the visible and NIR regime. This has hampered plasmonic metasurfaces from being applied in real applications[41]. Also, the lack of strong magnetic resonances in plasmonic nanoantennas has limited the capability of plasmonic metasurfaces for manipulating electromagnetic waves.

These drawbacks of conventional plasmonic metasurfaces have stimulated the studies of all-dielectric metasurfaces as an alternative for flat optical components[104,153–162]. The presence of magnetic resonances and low energy losses of high-index dielectric metasurfaces have offered unique optical effects, as well as high-index dielectric nanoantennas. One example is the high transmission efficiency from a metasurface using low aspect-ratio resonant dielectric nanoantennas as Huygens' sources[76,77,102,103]. The overlap of the electric and magnetic resonances excited in the nanoantenna results in the selective forward scattering[71,73–75]. By finely optimizing the configuration of both the resonator and its surrounding medium, the metasurface based on the Huygens' sources can fulfill eq. (2.31) and (2.32) in Chapter 2.4, showing nearly unity transmission with full phase control from 0 to 2π. On the other hand, perfect flat reflectors have also been

reported using metasurfaces built of high aspect-ratio dielectric resonators[78–80,163]. The spectral separation of the electric and magnetic dipolar resonances offers single-negative metasurfaces, in which either its relative permittivity or permeability is negative. The single-negative metasurfaces without substantial energy losses can offer nearly full reflection by satisfying eq. (2.33) and (2.34).

However, the control over the switching of high transmission / reflection have been barely explored[89,90]. Very recently, a circular dichroism waveplate was proposed using Si-based all-dielectric chiral metasurface, showing high transmittance or reflectance depending on the circular polarization[91].

In this Chapter, we theoretically and experimentally demonstrate how metasurfaces can act as a switch of the conversion from high transmission to high reflection by simply changing the linear polarization state of light in NIR region. These metasurfaces are composed of an array of Si dimeric nanoparticles, in which excited electric and magnetic dipoles are coupled and form hybridized modes[50,140,141]. Although the metasurface remains passive, the energy level of the hybridized modes can be controlled by the incident polarization, allowing the metasurfaces to have anisotropic optical responses. The concept is confirmed with numerical simulations using an array of Si spherical nanodimers in air, which is the ideal case that can be theoretically explored. Later, we fabricate an array of Si disk nanodimers with electron beam lithography on a sapphire substrate for the experimental demonstration. These ultrathin metasurfaces that can work either as a transmitter or as a reflector by simply controlling the linear polarization of the incident light could be one of the key components in tuneable optical flat devices.

5.1. Mode hybridization of electric and magnetic dipolar resonances in a high-index dielectric nanodimer depending on the incident polarization

In this section, we explore the mode hybridization in a high-index dielectric dimer. Similarly to the well-known interactions of the electric dipoles in plasmonic nanoparticles[18,164,165], electric and magnetic resonances excited in the dielectric nanoparticles can also show interactions between the resonances and hence mode hybridizations can occur. Here only the hybridization modes of electric – electric and magnetic – magnetic dipole interactions are explored. The higher-order modes, such as quadrupolar resonances, in general concentrate the electric field enhancement inside the

particles, leading to less strong interactions[50]. Also, heterogeneous electric – magnetic dipole interactions can be achieved in the dimer of dielectric nanoparticles; however, the contribution of this coupling is much smaller than the homogeneous electric – electric or magnetic – magnetic coupling, and it can be neglected, as previously reported[50,140]. We, therefore, explore only the homogeneous dipole interactions of electric – electric and magnetic – magnetic dipoles couplings.

Figure 5.1a and b show the schematic images of the electric and magnetic dipoles excited in a high-index dielectric dimer under the illumination of incident light polarized along (TM polarization) and perpendicular to (TE polarization) the dimer axis[140]. The TM polarized incidence excites electric dipoles along the dimer axis, inducing the bonding electric – electric dipole interaction, similar to the plasmonic dimers case[164–166]. This interaction can lower the energy of the excited electric dipoles, resulting in a redshift of the resonant wavelength of the electric mode, as shown in Figure 5.1c. At the same time, the magnetic dipoles are excited in each particle but perpendicularly to the dimer axis. The repulsive force between the poles in the particles heightens the energy level of the magnetic mode, leading to a blue-shift of the resonant wavelength. On the other hand, the other polarization (TE) results in an opposite effect both on the spectral shift and on the energy diagram of the dielectric dimer system. As shown in Figure 5.1b, the magnetic dipoles are excited along the dimer axis and form the bonding modes to red-shift its energy level by the TE polarized light (Figure 5.1d). The electric modes, in contrast, are blue-shifted by the coupling of the electric dipoles excited perpendicular to the dimer axis. Thus, the optical responses and hybridization modes of a high-index dielectric dimer can be controlled by changing the linear polarization state of the incident light.

5.2. Theoretical verification of the switch with dimer array of spherical Si dimers

5.2.1. Polarization dependent extinction of a dimer of Si spherical nanoparticles

To confirm the polarization dependent mode hybridizations described in the former

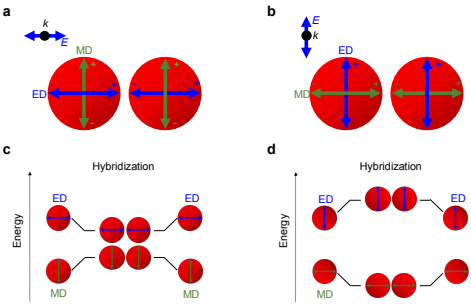

Figure 5.1. Polarization dependent dipole excitation and hybridization of the Si dimer illuminated by (a,c) TM polarization and (b,d) TE polarization. (a,b) Schematic images of excited electric and magnetic dipoles. (c,d) Mode hybridization of the Si dimer.

section, we first investigate an ideal dimer of spherical Si dimers in air. The unit cell of the metasurface consists of a dimer of Si spherical nanoparticles of 300 nm diameter, which are separated 10 nm. The FDTD method was used to numerally calculate the optical responses of the single unit cell and of the metasurfaces. Figure 5.2 shows a comparison of the calculated extinction spectra of a Si dimer and one of the isolated Si nanospheres forming the dimer, under the excitation of linearly polarized light. The isolated spherical nanoparticle showed the electric and magnetic dipolar resonances at λ = 860 nm and λ = 1110 nm, respectively. When the Si dimeric nanoparticle was excited by TM polarized light, the resonances of electric and magnetic dipoles were red-shifted and blue-shifted, respectively. These spectral shifts resulted in the two resonances approaching each other and showing a spectral overlap around λ = 1000 nm. The TE polarized light, on the other hand, blue-shifted and red-shifted the electric and magnetic dipolar resonances, respectively, causing the large spectral separation between the two resonant wavelengths. These results agreed well with the model of mode hybridizations, which present the energy shift depending on the incident polarization[140]. Thus, the illumination of TM and TE polarized incident light can give rise to the spectrum overlap and separation in the extinction spectrum of the Si nanodimer, respectively. Note that the spectral overlap of constituent nanoantennas of metasurface reportedly results in the high

transmission, whereas the spectral separation leads in opposition to a high reflection of the system[76–79].

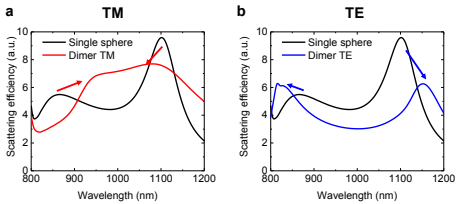

Figure 5.2. Extinction spectra of a single Si nanosphere and dimer which are illuminated by TM (a) and TE (b) polarized incidence.

5.2.2. Transmission and reflection of an array of the spherical Si dimers

As discussed in Chapter 2.4, high transmission and reflection of the metasurfaces can be achieved by the manipulation of their effective permittivity and permeability[101,105,106], which can be tuned by the electric and magnetic resonances of constituent dielectric nanoparticles[77,78]. Since high-index dielectric dimers show the pursued spectral overlap or separation between the electric and magnetic dipolar resonances depending on the incident polarization, an array of dielectric dimers could work as a metasurface that can switch the high transmission and reflection simply by changing the linear polarization of the incident light.

We numerically simulated the array of the Si spherical dimer using the FDTD method with an incident plane wave normal to the dimer array (Figure 5.3a). Figure 5.3b shows the transmission and reflection of the dimer array having the dimensions described in the previous section (diameter of 300 nm and separation distance of 10 nm). The periodicities of the array along and perpendicular to the dimer axis were set to 790 nm and 480 nm, respectively. The light illumination of TM polarization evoked high transmission 96.5 % at λ = 975 nm. However, when the dimer array was excited by the TE polarized light, the transmission peak disappeared and the reflection stayed as high as R = 86 % at λ = 975 nm. The switching wavelength between high transmission and reflection by the incident polarization agreed well with the wavelength where the spectral overlap and separation were observed in the extinction spectrum of the Si spherical dimer

unit (Figure 5.2). Thus, the switch from high transmission to reflection was theoretically demonstrated using the linear polarization tuning of the electric and magnetic hybridizations in high-index dielectric dimer unit cells.

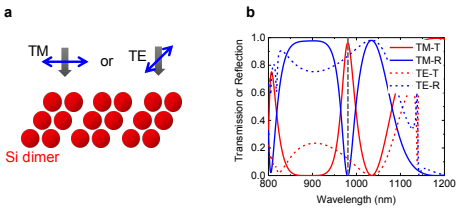

Figure 5.3. (a) Schematic image of the Si dimer array in air shined by the linearly polarized incident light. (b) Transmission (red lines) and reflection (blue lines) spectra of the Si dimer array under the illumination of TM (solid lines) and TE (broken lines) polarization.

Note that the reflection observed from the array of the Si spherical dimer under the excitation of TE polarized light was a bit lower than the reflection obtained using Si cylindrical nanoparticles with high aspect ratio[79]. This might be because the spectral separation of the electric and magnetic modes in the Si dimer in the case of TE-polarization was too large to achieve the high reflection. The centre wavelength of the large spectral separation is far from both the resonances and, hence, the absolute values of effective permittivity and permeability are small. This leads to the small imaginary part of the refractive index and allows the evanescent tunneling to occur, causing the reduction in the reflection value of the metasurface[78,79].

5.3. Experimental demonstration of high transmission to reflection switching

To experimentally demonstrate the switch between high transmission and reflection of a high-index dielectric metasurface, we fabricated an array of Si disk nanodimers on a

sapphire substrate using electron beam lithography and reactive ion etching, as described in detail in Chapter 3.3.1. The SEM images of the fabricated sample are shown in Figure 5.4, showing the dimers of Si nanodisk of 652 nm diameter and 314 nm height. The aspect ratio of the Si nanodisk was lower than 1 so that the electric and magnetic dipoles are excited at closer wavelengths under the illumination of the TM polarized incidence, and the large spectral separation, which reduces the reflection of the metasurface, can be circumvented under the illumination of the TE polarized incidence. The periodicities of the array were set to 1544 nm and 852 nm along and perpendicular to the dimer axis, respectively. These periodicities would meet the requirement of nanoresonator density which needs to be high enough to avoid the strong diffraction effect as discussed later. Also, the densely packed array is preferred especially for the high reflection to achieve the sharp dispersion in permittivity and permeability which can reach the negative value[78]. As shown in the SEM images, the array of identical Si dimers was fabricated uniformly throughout the metasurface.

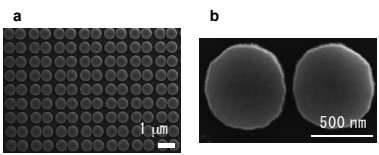

Figure 5.4. SEM images of the Si dimer metasurface fabricated on a sapphire substrate. The image of low magnification (a) confirmed the uniform fabrication on the substrate. The small gap and circular shape were observed in the image of high magnification (b).

We investigated the transmission and reflection of the fabricated Si dimer metasurface (Figure 5.5a) using FDTD method and FTIR spectroscopic technique (as detailed in Chapter 3.4.2), and the transmission and reflection spectra are shown in Figure 5.5b-c. In the FDTD simulation results, the metasurface exhibited the switch from the transmission of 99 % to reflection of 95 % at λ = 1688 nm by changing the polarization from TM to TE state. The experimental spectra also showed high transmission (T=86 %) and high reflection (R = 77 %) at λ = 1718 nm depending on the incident polarization. These results theoretically and experimentally confirmed that a metasurface comprised of dielectric nanodimers can switch the high transmission and reflection by changing the linear polarization state of the incident light. The small disagreements between the

numerical simulations and experiments might be attributed to the imperfection of the sample fabrication, and also to the experimental measurement conditions which were different from the ideal simulation. We used Cassegrain objectives in the experiment to observe transmission and reflection of the dielectric metasurfaces in the NIR region and, therefore, the transmitted or reflected light normal to the substrate cannot be observed. This might cause the small disagreement with the simulation in the obtained optical responses. However, the experimental setup can still monitor substantial amount of the transmitted and reflected light and, hence, does not change our conclusion.

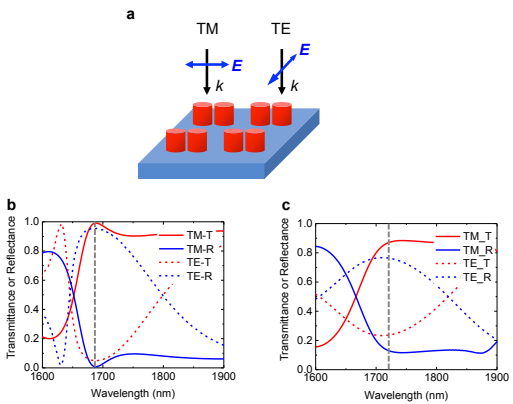

Figure 5.5. (a) Schematic image of the Si dimer array on a sapphire substrate illuminated by the linearly polarized incident light. (b-c) Transmission (red lines) and reflection (blue lines) spectra of the Si dimer array under the illumination of TM (solid lines) and TE (broken lines) polarization in the FDTD simulations (b) and experiments (c).

The periodicity along the dimer axis was 1544 nm, which was close to the switching wavelength around 1700 nm. Another optical effect, the diffraction of light, then might affect the transmission and reflection properties of the fabricated metasurfaces. To estimate the influence of the light diffraction, we numerically calculated the transmission

and reflection of the metasurfaces by varying the diameters and height of the nanodisks and the periodicities of the dimer unit, which are shown in Figure 5.6. When the size of the particles forming the unit cell of the metasurfaces became just 5 % smaller or larger than the original one (Figure 5.6a and 5.6b), the switching wavelength was correspondingly shifted by up to 70 nm. However, as shown in Figure 5.6c and 5.6d, the change of 5 % in periodicity of the unit exhibited little shift, up to 20 nm, in the position of the wavelength at which the switch between high transmission and reflection was observed. The very small shift observed by varying the periodicity could be attributed to the interaction between the dimers which can be altered by the separation distance. These results suggest that the switching between high transmission and reflection observed by

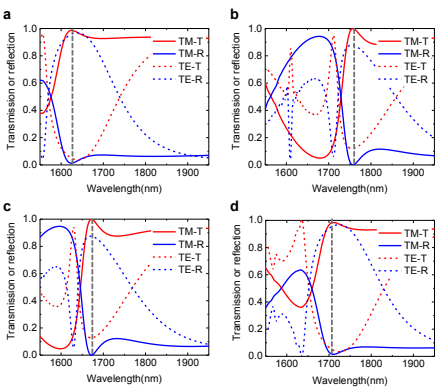

Figure 5.6. Transmission (red lines) and reflection (blue lines) spectra of the Si dimer arrays under the illumination of TM (solid lines) and TE (broken lines) polarization in the FDTD simulations, where the geometrical parameters were changed. (a,b) The diameter and height of the dielectric nanodisk were changed from the original nanodisk of 652 nm diameter and 314 nm height, to (a) 619 nm diameter and 298 nm height and (b) 685 nm diameter and 330 nm height. (c,d) The periodicities of the dimer unit were changed from the original metasurface with periodicities of 1544 nm and 852 nm along and perpendicular to the dimer axis, to (c) 1467 nm and 809 nm, and (d) 1621 nm and 895 nm.

the dielectric metasurface originated mainly from the manipulation of effective permittivity and permeability determined by the electric and magnetic dipoles excited in the dielectric dimers, rather than the diffraction effect.

5.4. Summary

We theoretically and experimentally demonstrated that metasurfaces comprised of the array of high-index dielectric dimers can switch the optical response from high transmission to high reflection simply by changing the incident linear polarization. The hybridization mode of the excited electric and magnetic dipoles in the dielectric dimer can be tuned by the polarization of the incident light. The numerical simulations of an array of Si spherical nanodimers revealed that the different mode hybridizations lead to the spectral overlap or separation between the electric and magnetic dipoles, depending on the incident polarization. These spectral features resulted in switching between high transmission and high reflection of the dielectric dimer metasurface by tuning linear polarization state. The switch between high transmission and reflection was experimentally confirmed using a Si disk nanodimer array fabricated on a sapphire substrate and FTIR measurement setup. The tuneable control of the optical response of metasurfaces demonstrated in this chapter could boost the development of highly functional surface for flat optics.

Chapter 6

Tunable directional light scattering from asymmetric dielectric dimers

Chapters 4 and 5 mainly focused on dielectric nanostructures which were used for the directional control of light propagation into the forward or backward direction along the incident axis. This chapter will attempt to extend the capability of dielectric nanostructures of controlling the direction of light propagation by adding a tuneability of the direction away from the incident axis. Precisely, we theoretically and experimentally reveal that a dielectric nanodimer consisting of nanoparticles with different dimensions can scatter light directionally either into the right or left direction by just changing the incident wavelength. Whereas plasmonic nanoantennas would require complex configurations, such as bimetallic structures to attain such functionality[22,167], dielectric nanoantennas can offer easier ways to achieve bidirectionality. A V-shaped nanoantenna made of Si has very recently shown that scattered light can be routed depending on the excitation wavelength[132]. However, a V-shaped antenna fabricated on a substrate are only suitable to steer the scattering of light propagating towards the substrate at normal incidence. Tunable control of directional scattering along the substrate would be preferable for many applications, such as spectroscopic techniques and optical nanocircuitries.

In this chapter, asymmetric Si dimers are explored to achieve tunable directional scattering along the substrate. The underlying reason for directional scattering is that, as it has been shown in previous chapters, amplitude and phase differences of electric and magnetic resonances in dielectric nanoparticles can be tuned by changing geometrical dimensions[55,57]. Therefore, by carefully designing the dimer configuration, the direction of the scattered light becomes tunable due to the interference between the dipoles excited in each particle. Here, we carry out full theoretical calculations using the analytical dipole-dipole model to determine a favourable configuration for highly directional scattering which is tunable by the incident wavelength[50]. Experimental demonstrations are conducted using a back focal plane (BFP) measurement technique combined with a prism coupling setup. The prism coupling setup with grazing incidence illumination generates

an evanescent wave, which propagates along the substrate but decays exponentially in the air, and excites the nanoantenna. We also propose a practical configuration of asymmetric dimers as a nanoscale routing element for an optical nanocircuit using electromagnetic radiation. Tuneable directional control of the scattered light combined with low energy losses presented in this paper can facilitate the development of efficient sensors, waveguides and optical circuits at the nanometer scale.

6.1. Si spherical asymmetric dimer for tuneable directional scattering

6.1.1. Numerical simulations of scattering properties

The polarizability of dielectric nanoparticles strongly depends on their dimensions[32]. Therefore, phase differences in the polarization and interferences between them should appear when two dielectric particles of different dimensions are placed in proximity. This interaction may be able to determine the properties of scattered fields from the dielectric dimer, providing a method to tune the scattering direction.

First, we theoretically investigated a dimer system consisting of spherical Si nanoparticles in air based on an analytical dipole-dipole model (as detailed in Chapter 3.1). Here the electromagnetic responses of Si spherical nanoparticles are substituted by electric and magnetic dipoles, justified by the large ratio of wavelength to particle dimension leading to less significance of higher order modes[98]. In our optimized exemplary system, two nanospheres of diameter D_1 and D_2 ($D_1 < D_2$), are placed at r_1 and r_2 in a Cartesian coordinate space. The configuration used in the theoretical analysis is described in Figure 6.1a. The radii of the smaller and larger spheres are D_1 = 150 nm and D_2 = 230 nm, respectively, and these two spheres are separated by a gap of d = 8 nm in air. Figure 1b shows the calculated extinction spectra of electric and magnetic dipoles excited in a dimer of Si spherical nanoparticles. The two spectra show three peaks; the resonances at the shortest and longest wavelengths are attributed to the excited electric dipoles in the larger particle, and the resonances at intermediate wavelengths correspond to the dipoles excited in the smaller particle. The resonant wavelength of the dielectric particle strongly depends on their dimensions since the oscillation or rotation of displacement current inside the particle results in the excitation of electric or magnetic resonances[19,20]. Note

that the intensities of these resonances are comparable between the two spheres and, hence, suitable for generating constructive or destructive interferences.

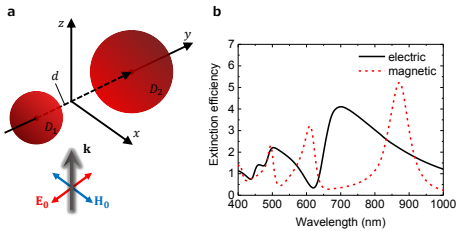

Figure 6.1. (a) A schematic image of a dimer of Si spherical nanoparticles and the propagation direction of incident radiation (TM-polarized). (b) Extinction spectra of electric and magnetic dipoles calculated using an analytical dipole-dipole model.

In Figure 6.2a, we plot the angle of maximum scattering intensity in the projection of the far field pattern on the y-z plane. Here the scattering angle of $\varphi = 0^{\circ}$ corresponds to the forward scattering, and the two quadrants ($\varphi = 0^{\circ} \sim +90^{\circ}$ and $\varphi = 0^{\circ} \sim -90^{\circ}$) correspond to the scattering hemisphere of the smaller and larger particles, respectively. The direction of the scattered light bends left ($\varphi = +18^{\circ}$) or right ($\varphi = -52^{\circ}$) at λ =500 nm and λ = 630 nm, respectively. The y-z plane projection of the far field patterns at these wavelengths are shown in Figure 6.2b. At λ = 500 nm, the scattered light was directed to the smaller sphere but suppressed in the direction of the larger sphere. Meanwhile, a completely opposite result was achieved at λ = 630 nm; the light scattered to the smaller sphere was suppressed but the light to the larger sphere was intensified. This means that the direction of the scattered field can be tuned by changing incident wavelength.

Note that the diameters and gap separation of the dimeric structure are parameters that can affect the resonant characteristics of the dielectric dimer and, hence, the property of light steering. Figure 6.3a and 6.3b show the influence of the gap size of the asymmetric Si dimer. Extinction spectra and far field patterns of scattered field of the spherical dimer were calculated with different gap separations (d = 8, 50, 100, 300, 600 nm) at λ = 630 nm. As the gap was enlarged, electric dipolar resonances became narrow, which was revealed in the previous study[50]. The directionality of the scattering to the larger sphere side was reduced by increasing the gap distance, specifically the separation

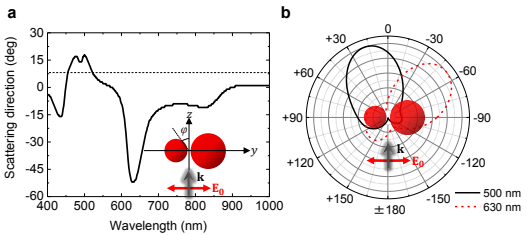

Figure 6.2. (a) Angle of maximum scattered intensity on the y-z plane projection. (b) Far field radiation patterns of the scattered light at λ = 500 nm and λ = 630 nm.

d > 100 nm. This is because the second term of the phase difference model described in the next section changes with the gap separation. Furthermore, the small gap is suitable for creating nanoantennas which would be used in optical nanocircuit application. We also estimated the influence of diameter ratio between D_1 and D_2 to the steering of scattered field. Figure 6c shows the extinction spectra of Si spherical dimers where the ratio of the diameter between the two spheres, $X = D_1 / D_2$, was varied as X = 0.5 (D_1 = 125 nm and D_2 = 250 nm), 0.65 (D_1 = 150 nm and D_2 = 230 nm), 0.8 (D_1 = 168 nm and D_2 = 210 nm) and 1 ($D_1 = D_2$ = 190 nm). The position of the resonant peaks shifted since the electric and magnetic resonant wavelengths depend on the dimension of the particle. Note that here we changed the diameter of both the two spheres because the wavelengths at which the directional scatterings can be observed should be kept within visible regime considering the prospective application of optical nanocircuit proposed here. Figure 6d shows the far field distribution of scattered fields in which the directional scattering to either left or right was achieved depending on the excitation wavelength. Since the resonant wavelengths of the dipolar modes were shifted because of the change in the geometrical dimensions, the wavelengths showing the directional scattering were also shifted. However, the steering of scattered field can be basically achieved when asymmetric Si dimer is used, whereas the symmetric dimer (X = 1) does not steer the light either to left or right throughout the incident wavelengths.

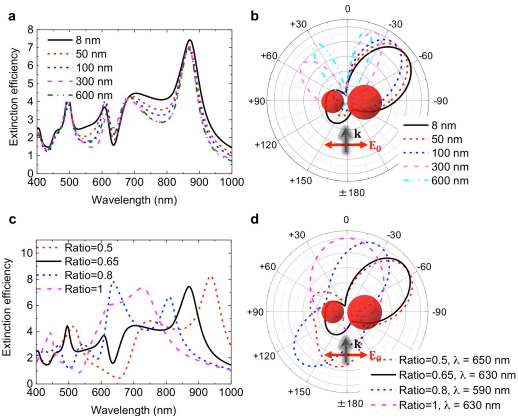

Figure 6.3. Influence of (a-b) gap size and (c-d) size ratio to the scattering properties (a, c) Total extinction spectra of the dimer and (b,d) far field patterns of the scattered field at λ = 630 nm.

Figure 6.4a shows the extinction cross section calculated by both the dipole-dipole model and the full numerical simulations by FDTD method to verify our theoretical model. These spectra basically showed a good agreement. A distinct peak at λ = 640 nm was observed only in the FDTD simulation, which corresponds to the magnetic quadrupolar resonance of the larger sphere (not contemplated in the dipolar model). Figure 6.4b shows the scattering radiation patterns at λ = 630 nm calculated by both the analytical and numerical simulation. These patterns agreed well with each other, even though the FDTD calculation includes higher order modes. This may be because higher order modes generally show narrow peaks compared to the dipolar modes, which could result in the small effect onto far field radiation patterns calculated by the dipole-dipole model. The existence of the magnetic quadrupolar resonance in the FDTD calculation could be responsible of the smaller scattering rotation (φ = -33º) than that in the dipole model (φ = -52º) due to the interference.

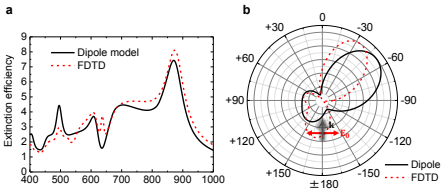

Figure 6.4. Comparison of the (a) extinction spectrum and (b) far field radiation pattern of the scattered field at 630 nm, calculated by the analytical dipole-dipole model (black solid line) and by the full numerical FDTD method (red dash line).

Figure 6.5 shows the angle of maximum scattering intensity in the far field radiation pattern on the y-z plane calculated by the dipole-dipole model and FDTD methods. Although these two plots showed a good agreement, the new peak of the magnetic quadrupolar mode at $\lambda = 640$ nm caused a destructive effect for the light steering to the right direction. However, we can see that there was also extra constructive interference in the FDTD result to enhance the degree of steering around $\lambda = 550$ nm to the left and $\lambda = 850$ nm to the right. Note that the configuration here was not optimized with the FDTD calculations. Furthermore, as the FDTD calculations show later in this chapter, in a real situation of a dimer of Si disks on a substrate, the steering of light is of around 30º, which is enough to excite a target at a certain position selectively. These results show that the influence of higher order modes does not change our conclusion.

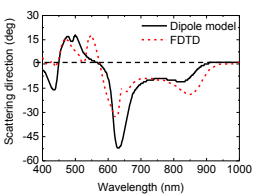

Figure 6.5. Angle of the maximum scattered field projected on the y-z plane calculated by the dipole model (black solid line) and numerical FDTD method (red dash line).

6.1.2. Theoretical analysis of phase difference

To understand the basic mechanism of this directional scattering, the phase difference of the excited dipoles was extracted from the analytical dipole-dipole model and analyzed. The electric dipoles excited along to the dimer axis were found to have no major contributions to the scattered light along the y-axis direction. In a similar manner, the electric dipoles excited along the z-axis by the magnetic dipoles can be neglected since their intensity in the analyzed illumination configuration is very small. Therefore, we focus only on the magnetic dipoles excited along the x-axis. The oscillation of the magnetic dipole can generate the electromagnetic field, which can contribute to scattered field intensity in far field. It should be noted that excitation of magnetic resonances is possible due to the high refractive index of the dielectric material, whereas in the case of plasmonic nanostructures this is not possible because the small skin depth does not allow the field to penetrate enough as to generate sufficient displacement currents for the excitation of magnetic resonances[22]. The phase difference generated by each particle, $\Delta\Phi_1$ and $\Delta\Phi_2$, can be calculated from the complex value of the magnetic polarizabilities. For the phase difference model, the scattering intensities I_+ and I_- due to the interferences between the two magnetic dipoles are given by

$$I_+ = \left| |m_{1x}| e^{-\Delta\Phi_1} + |m_{2x}| e^{-\left(\Delta\Phi_2 - k(R_1+R_2+d)\right)} \right|^2 \tag{6.1}$$

$$I_- = \left| |m_{1x}| e^{-\Delta\Phi_1} - |m_{2x}| e^{-\left(\Delta\Phi_2 - k(R_1+R_2+d)\right)} \right|^2 \tag{6.2}$$

in the direction of the smaller disk (+) and the larger disk (-), respectively. Directional scattering is achieved if constructive interference occurs in one direction and destructive interference in the other. Figure 6.6 shows a comparison of the scattered light intensity propagating towards φ =+90º and φ = -90º, given by the far field calculated with the analytical dipole-dipole model and with the approximated phase difference model. These two plots qualitatively agree well specifically in terms of the wavelengths at which directional scattering occurs. The small discrepancy between the two plots can be attributed to not considering the presence of electric dipoles and their very small interaction with magnetic dipoles.

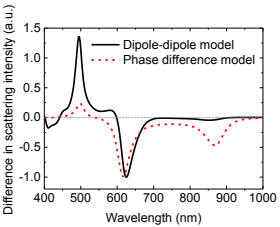

Figure 6.6. Comparison of the difference in scattering intensity calculated by the analytical dipole-dipole model (black solid line) and the phase difference model (red dash line).

We also explored different polarization configurations of the exciting radiation. Electric and magnetic dipoles in dielectric nanoparticles are excited at different wavelengths and perpendicular to each other. A change in incident polarization could lead to a shift of the wavelength at which the directional scattering is achieved. Here, the dimer structure was the same as the previous one, but the incident light is configured with electric polarization perpendicular to the dimer axis (TE-polarized). Figure 6.7 shows the far field distribution of the scattered light which was projected on the y-z plane at λ = 430 nm and 604 nm. The scattered light was also directed to the larger (φ = -13º) or smaller (φ = +10º) sphere, depending on the incident wavelength. In this polarization configuration, the directional scattering could be mainly attributed with the interference between the two electric dipoles excited perpendicular to the dimer axis. Since the electric dipoles resonate at shorter wavelengths than the magnetic dipoles, the wavelengths at which the directional scattering was achieved were blue-shifted, which also supports our conclusion that the dipoles excited perpendicular to the dimer axis are responsible for the tuneable directional scattering. The degrees of the rotation were slightly smaller, because the dimensions were optimized in the case of TM polarization. The obtained results, therefore, suggest that incident polarization provides, in addition to excitation wavelength, another route for tuning the spectral response of directional scattering.

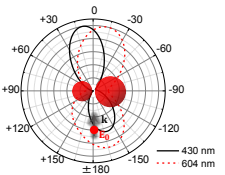

Figure 6.7. Far field radiation patterns of the scattered light at λ = 430 nm and 604 nm excited with TE-polarization.

6.2. Experimental demonstration of tuneable scattering along a substrate

For the experimental demonstration, a dimer of Si nanodisks was fabricated by electron beam lithography followed by reactive ion etching, as described in Chapter 3.3.1. An amorphous Si thin layer on a silica substrate was used here to match the refractive indices between the substrate and prism, which was incorporated in the measurement system of the scattering patterns. Figure 6.8a shows scanning electron microscopy (SEM) images of the fabricated asymmetric Si dimer. The SEM observations confirmed that the side walls of the structures were vertical relative to the substrate and, hence, the gap distance between the nanodisks of the dimer was uniform from the bottom to the top of the disks. Isolated single nanodisks were also fabricated for comparison as a reference, as shown in Figure 6.8b and 6.8c.

First, the backward scattering spectra of the fabricated samples were measured using dark field optical spectroscopy, as illustrated in detail in Chapter 3.4.1. The antennas were fabricated with a pitch of 5 μm between them, which was sufficient to ensure that scattering was collected from a single antenna at a time. Incident light was polarized along the dimer axis using a linear polarizer along the illumination path. Numerical simulations were conducted with FDTD method to calculate the scattering spectra of Si nanodisks on a silica substrate. A dark field source was used in the numerical simulations to reproduce the experimental settings. The experimental and simulated scattering spectra are shown in Figure 6.8d-f. Theoretical and experimental results show good agreement,

verifying that the experimentally fabricated samples have both of electric and magnetic resonances as theoretically predicted. The experimental spectrum showed a shift to shorter wavelengths by around 30 nm. This is likely due to small imperfections in the fabricated samples and the presence of a native oxide layer covering the surface of the nanoantennas. Such a native oxide layer would reduce the effective volume of the nanoantennnas[59].

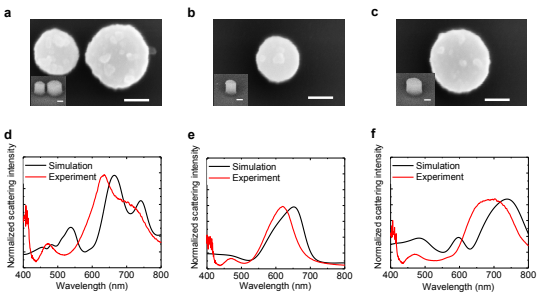

Figure 6.8. (a) SEM image of the fabricated asymmetric dimer of Si nanodisks. The scale bar is equal to 100 nm. H = 170 nm, D1 = 180 nm, D2 = 250 nm and d = 40 nm correspond to height, diameters of the small and large nanodisks, and the gap distance, respectively. The isolated small (b) and large (c) disks were also fabricated for comparison. (insets) SEM images from tilted angle. (d-f) Dark field scattering spectra of the dimer (d), small disk (e) and large disk (f), obtained from experiment and simulation.

Measurements of the scattering patterns of the fabricated asymmetric dielectric dimer were then performed using the BFP imaging setup combined with prism coupling, which was illustrated in detail in Chapter 3.4.3. This measurement system allows us to explore the field scattered from the nanoantennas, propagating along the substrate. Figure 6.9 compares the calculated and measured scattering patterns for incident illumination at λ = 480 and 590 nm. Here, we define scattering towards the smaller particle side as the positive direction and scattering towards the larger particle side as the negative direction, as shown in Figure 6.9a. The scattering patterns obtained experimentally agree well with the numerically calculated patterns. At λ = 480 nm, the scattered field was steered to the

positive direction. On the other hand, at λ = 590nm the scattering direction is clearly steered towards the negative direction. From the results obtained in the numerical simulation, the steering angle was estimated as +9° at λ = 480 nm and -47° at λ = 590 nm. These angles would selectively guide light and signals with different wavelengths to two different angular regions, as shown later.

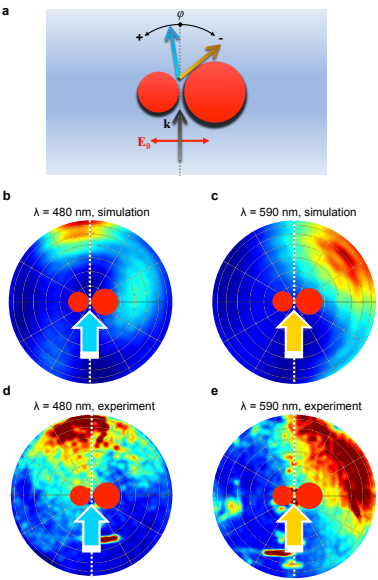

Figure 6.9. Scattering patterns from an asymmetric dimer of Si nanodisks. (a) Schematic image describing how the scattering angle was defined. Scattering patterns were monitored for incident illumination at λ = 480 nm (b,d) and λ = 590 nm (c,e) in the simulation and experiment. Note that experimental results include some speckles, which is an undesirable artefact of light being scattered from the optical measurement setup or some defects/roughness on the sample's surface. See the experimental setup detailed in Figure 3.6.

For comparison, the experimental and simulated scattering patterns for single disks are also shown in Figure 6.10. Even though the shape of the simulated and measured scattering patterns did not fully agree, due to the small signal collected from the isolated nanodisks and the limitation in the sensitivity of the CCD camera, the single disks did not show any asymmetric side scattering in either the positive or negative directions, but only along the incident axis (0°).

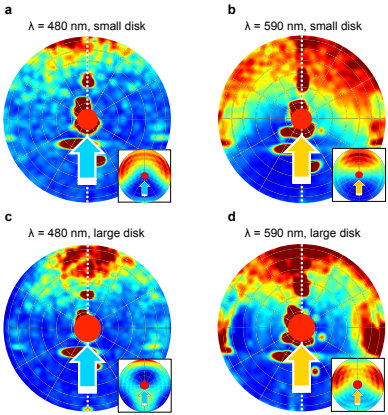

Figure 6.10. Scattering patterns of isolated single Si nanodisk on a silica substrate in the experiment. (Insets) Scattering patterns simulated by FDTD methods. Scattering patterns were monitored for incident illumination at λ = 480 nm (a,c) and λ = 590 nm (b,d) in the simulation and experiment.

In order to quantitatively analyze the directionality of the nanoantenna, we calculated the directivity, *D*, of the scattered light[21,132]. The directivity was estimated as the ratio of light intensity scattered to the two directions,

$$D = 10\log_{10}\frac{\iint_{(\theta_m-\delta,\varphi_p-\delta)}^{(\theta_m+\delta,\varphi_p+\delta)} S(\theta,\varphi)\sin\theta\, d\varphi d\theta}{\iint_{(\theta_m-\delta,\varphi_n-\delta)}^{(\theta_m+\delta,\varphi_n+\delta)} S(\theta,\varphi)\sin\theta\, d\varphi d\theta} \tag{6.3}$$

where $S(\theta,\varphi)$ is the intensity of the scattered light at a given angle in the BFP image. θ_m = 57°, φ_p = 9°, φ_n = -47° and δ = 7° were assigned for the calculation (see Figure 6.11a). Figure 6.11b shows a plot of the directivity as a function of the wavelength. The experimental results showed a reasonable agreement with the numerical ones obtained from simulation. The tuning of scattering direction from the positive to negative direction was clearly observed in the wavelength region from λ = 450 nm to λ = 650 nm. The range of the directivity reached -4.8 to +6.8 dB in the simulation and -3.1 to +3.1 in the experiment. The quantitative differences between the experiment and simulation may be caused by small errors in the fabrication and the undesirable speckles observed in the experimental BFP images. As shown in the previous section, the scattering properties of asymmetric dielectric dimers can be significantly affected by a variety of geometrical parameters of the constituent nanodisks. Also, the ellipticity of dielectric nanoparticles have been studied as a key factor to determine the scattering pattern in far field[74,76,79,137]. Moreover, the directivity defined by eq. (1) in this paper could be slightly shifted when strong noise is observed in the experimental BFP images. However, this does not change the conclusion that an asymmetric Si dimer can steer light to selective directions depending on the wavelengths of excitation, as it can be seen in Figure 6.11b.

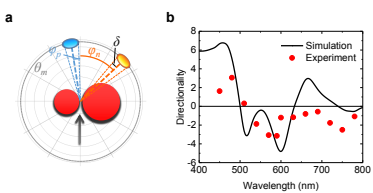

Figure 6.11. (a) A schematic image of the angular regions (blue and orange circles) used for the directivity calculation. (b) Directivity of the scattered field from the asymmetric Si nanodimer calculated from the obtained scattering pattern in the simulation and experiment.

To support the result of the scattering directivity, we plotted the peak scattering angle of φ in Figure 6.12. We used the data at θ_m = 57°, which corresponds to the polar angle used to calculate Figure 6.11b. In the experimental plot, since the data was noisy, we smoothened the data near the peak with polynomial function to find the peak. This plot

qualitatively showed that the scattering direction was shifted from the positive to negative direction as the excitation wavelength was increased.

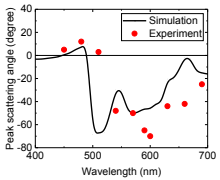

Figure 6.12. The peak scattering angle as a function of excitation wavelength.

The scattered light measured in the experiment did not propagate exactly along the substrate since the objective used to collect the scattered light in this study had NA = 0.9, which corresponds to a collection angle of up to 64°. However, this NA value is enough as to observe the tail of scattering lobes from excited dipoles (see Figure 3.6). This was confirmed via numerical simulation using an incident wave propagating along the substrate and the asymmetric dimer which has the same dimensions as in the experimental case. The calculated scattering patterns in the plane which is parallel to the substrate are shown in Figure 6.13. Although the wavelengths and scattering angles used in Figure 6.13 were not the same as those used for the experimental demonstration due to the use of a different excitation method, the asymmetric nanodimer showed the capability of

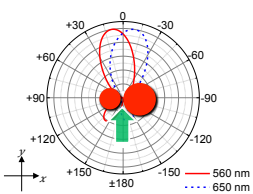

Figure 6.13. Scattering patterns of the asymmetric Si dimer in the plane parallel to the substrate. The nanodimer was illuminated by the incidence propagating along the substrate.

routing the scattering either to the left or to the right direction along the substrate. This result clearly suggests that the experimental demonstration in this study provides the proof of concept of controlling bidirectional scattering along the substrate using asymmetric dielectric antennas.

Also mention that a monometallic Au dimer was reported to show side scattering, but not tuneability of the scattering direction[22]. To highlight this, we conducted numerical FDTD simulations of the Au nanodimer under the same simulation condition as the Si nanodimer. As representative scattering patterns at λ = 480 nm and 590 nm are shown in Figure 6.14, the Au nanodimer showed a small steering of light, but no tuning between the negative and positive direction throughout the visible regime. The main hypothesis of this behavior is the change or switch of the magnetic dipoles excited perpendicular to the dimer axis are mainly responsible to tune the scattering direction in the Si dimer case. However, in the case of the Au nanodisks, the asymmetric dimer cannot excite the magnetic resonances, resulting also in a very little steering of the scattered light.

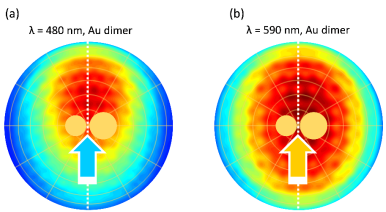

Figure 6.14. Simulated scattering patterns of the Au nanodimer at (a) λ= 480 nm and (b) 590 nm. The dimensions of the Au dimer were as follows: H = 50 nm, D_1 = 110 nm, D_2 = 130 nm and d = 40 nm correspond to height, diameters of the small and large nanodisks, and the gap distance, respectively.

6.3. Example of a practical application: tuneable excitation in optical nanocircuitry

In an optical circuit, a tuneable nanoantenna could be responsible to guide the light to an appropriate direction. In this section, we investigate the possibility of using our asymmetric dielectric dimer as a tuneable nanoantenna for an optical circuit.

We performed numerical simulations of the electromagnetic behavior of the light scattered from the nanoantenna using the FDTD method. Specifically, we explore a platform with a dimer of Si nanodisks placed on a silica substrate, in line with experimentally achievable geometric dimensions. The disks have diameters of 108 nm and 140 nm and a height of 120 nm, being separated 20 nm. A plane wave source illuminates the structure in parallel to the substrate with the electric field polarized along the dimer axis. The scattering spectrum calculated in this configuration is shown in Figure 6.15a. A small peak at λ = 470 nm corresponds to the electric dipolar resonance of the smaller disk. The overlap of the magnetic dipole of the smaller disk and the electric dipole of the larger disk manifests itself with a distinct peak at λ = 510 nm. The peak at λ = 610 nm is associated with the magnetic dipole of the larger disk. Note that the peaks around λ = 400 nm correspond to the magnetic quadrupolar resonances of the Si disks. These higher order modes were neglected in the analytical dipole-dipole model used in the previous section. Figure 6.15b shows the scattering patterns in the far field at λ = 440 nm and 600 nm. While the scattered light was directed to the smaller disk at λ = 440 nm,

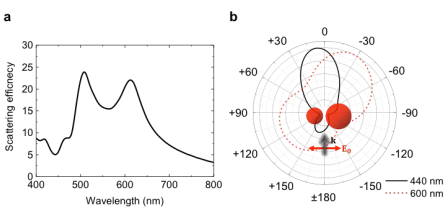

Figure 6.15. (a) Scattering spectrum of a dimer of Si nanodisks on a silica substrate illuminated by an incidence propagating along the substrate with TM-polarization. (b) Far field radiation patterns of the scattered light on the plane parallel to the substrate at λ = 440 nm and 600 nm.

the scattering direction changed towards the larger disk side at λ = 600 nm. Thus, the dimer of Si nanodisks on a substrate also exhibits switchable scattering depending on the wavelength of incidence. This configuration would be quite straightforward to fabricate by top-down single-step lithography, in contrast to scattering elements based on bimetallic structures.

This directional scattering could be used to route light propagation to selective positions, depending on the incident wavelength. To explore this possibility, we studied configurations with two dimers using FDTD method. The first dimer was excited under the same source conditions as the single one described in Figure 6.16. The second dimer was placed at two different angular positions from the first dimer, +7.2° and -27° and at a separation distance of 1.2 μm. The intensity of the electric near field excited inside and outside the second dimer was monitored. When the first dimer was illuminated by incident light at λ = 440 nm, the second dimer placed at +7.2° showed a higher electric field intensity than the other placed at -27°. In contrast, when the first dimer was illumina-

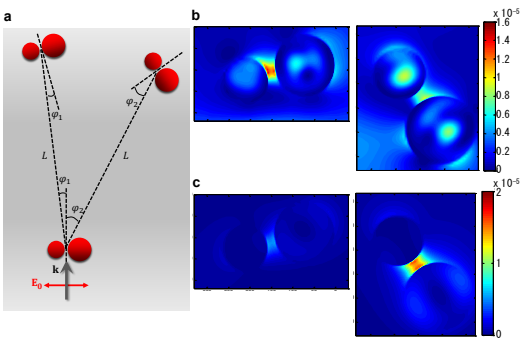

Figure 6.16. (a) Schematic illustration of the configuration used for the demonstration of tunable optical guide. The first dimer was illuminated by the incident light parallel to the substrate with polarization along the dimer axis. The second dimer was placed at either left (φ_1=7.2°) or right (φ_2=27°) from the first one. The separation distance is L=1.2 μm. (b,c) The electric field intensity monitored at the second dimer with the wavelength of excitation at λ = 440 nm (b) and 600 nm (c).

-ted by incident light at λ = 600 nm, the second dimer placed at -27º was excited more than the other placed at +7.2º. This selective and tuneable excitation corresponds to the far field distribution of the first dimer and its dependence on the incident wavelength. These results suggest that asymmetric dimers of high refractive index dielectrics can be used as nanoantennas which can tune the direction of the scattered field propagation by simply changing the wavelength of excitation.

6.4. Summary

In conclusion, we have theoretically and experimentally demonstrated that asymmetric dimers of dielectric nanoparticles can function as nanoantennas for tuning the scattering direction of incident electromagnetic radiation by changing the incident wavelength. The excited dipoles and scattered fields have been theoretically explored using the analytical dipole-dipole and phase difference models, revealing that interference between two dipoles generated perpendicular to the dimer axis is mainly responsible for the directional scattering. The tuneable directionality of the scattered field was achieved even when the dipoles perpendicular to the dimer axis were exchanged between electric and magnetic ones by changing the incident polarization. The optical measurement setup using prism coupling and a BFP imaging technique enabled the characterization of the profile of the scattered field propagating along the substrate, demonstrating that the scattering direction can be routed by changing the excitation wavelength. Finally, an application as a tunable nanoantenna for optical nanocircuitry has been demonstrated. This study shows that asymmetric high-index dielectric dimers could be a basic unit for spectroscopic techniques and nanocircuitry where tuning the light propagation direction would be helpful to improve their performance.

Chapter 7

Efficient third harmonic generation from metal-dielectric hybrid nanoantennas

In the previous chapters, we investigated linear optical responses, specifically the efficient and tuneable control of the light propagation direction, using the electric and magnetic resonances of dielectric nanostructures. Recent studies have revealed that the dielectric nanoantennas are also promising optical units to achieve efficient nonlinear optical effects in nanometer scale. The high nonlinear susceptibility of high-index dielectric materials and the large volume of field enhancement without considerable energy losses can significantly improve the efficiency of nonlinear harmonic generations, as explored in Chapter 2.5[49,51,52,62]. However, despite the fact that all-dielectric configurations have, in several cases, highly exceeded plasmonic-based nonlinear performances[82,83,87], there is still a clear demand for novel strategies that further improve the THG efficiency at nanometer scales. Indeed, while Ge nanostructures have shown conversion efficiency values as large as 0.001% at 550 nm (green) TH wavelength (1650 nm fundamental wavelength) [28], this performance cannot be extended to the blue region of the visible spectrum. This is due to the very high intrinsic absorption of gemanium below 1600 nm, including 1300-1400 nm fundamental wavelengths of the blue THG[45]. Moreover, while absorption in Si is small in this spectral regime (enabling tunability at blue TH frequencies), its lower refractive index and third-order susceptibility compared to Ge, lead to a clear reduction of maximum possible efficiencies, reaching values of only 0.0001%-0.0002% even when considering complex Si metamaterials[60,82,83,88].

In this Chapter, we reveal that a hybrid structure that combines a metallic and a high-index dielectric nanoparticle can produce efficient THG along all the optical regime (from blue to red wavelengths). The adopted approach, theoretically modelled very recently[168], can boost the electric field enhancement inside a resonant Si nanodisk, placed at the core of a plasmonic Au nanoring (schematic illustration shown in Figure 7.1), highly improving the nonlinear capabilities of the nanosystem. When exciting the composed structure at the anapole mode, which is detailed in Chapter 2.6, a TH conversion efficiency as high as 0.007% at a TH wavelength of 440 nm is experimentally demonstrated by femtosecond laser pumping. Comparison with the isolated Si and Au

nanostructure components further confirms that the high TH intensity in the hybrid is achieved by the coupling between its constituting elements. Finally, by adequately modifying the dimensions of the metal-dielectric nanoantennas, we extend its spectral range of operation to longer wavelengths in the visible light region.

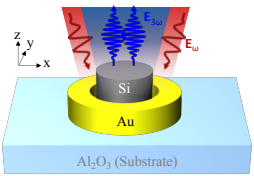

Figure 7.1. Schematic of the experimental configuration used for THG studies.

7.1. Excitation of anapole mode with a hybrid nanostructure

7.1.1. Extinction spectra of the fabricated samples

Si-Au (nanodisk-nanoring) hybrid structures were fabricated on a sapphire substrate via electron-beam lithography and reactive-ion etching techniques. Figure 7.2 shows a scanning electron microscope (SEM) image of the designed hybrid nanoantenna. A 155 nm thick Si nanodisk (680 nm diameter) is surrounded by an 80 nm height Au nanoring (inner diameter of 780 nm, outer diameter of 1360 nm), with a gap of 50 nm in-between to ensure strong coupling[50,140,169].

We first numerically and experimentally analyze the extinction spectrum of the fabricated samples to explore their linear response. Numerical simulations were conducted using the FDTD methods considering linearly polarized plane waves propagating normal to the substrate surface. The experimental extinction spectrum, characterized through FTIR spectroscopy, was obtained by measuring the transmission (T) spectrum of an array of identical 20 x 20 hybrid nanostructures, interspaced by 3.5 μm distance to avoid optical coupling between them. Black curves in Figure 7.3a and 7.3b show the experimental and simulated extinction spectrum of the metal-dielectric

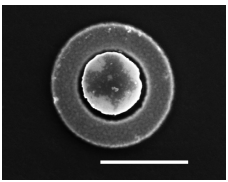

Figure 7.2. SEM image of the fabricated hybrid nanoantenna. The Si nanodisk has a diameter D_1 = 680 nm with height H_1 = 155 nm, and the Au nanoring has an inner diameter D_{21} = 780 nm, outer diameter D_{22} = 1360 nm and height H_2 = 80 nm. The scale bar is 1 μm.

nanosystem, respectively, presenting a minimum at around λ = 1325 nm. As verified later in the chapter, this sharp valley in the extinction spectrum indicates the excitation of the anapole mode, whose physical origin has been theoretically attributed to the destructive interference in the far field between the radiation patterns produced by the electric and toroidal dipole modes[107]. Note that the minor differences observed between experiment and theory could arise from the small size and shape variations among the different structures composing the measured array.

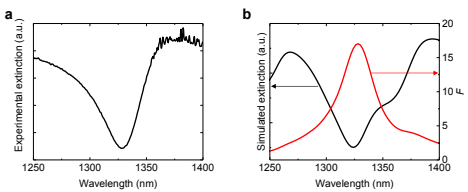

Figure 7.3. (a) Experimental and (b) simulated extinction spectrum of the hybrid nanoantenna (black curves). Experimental extinction values were calculated as 1-T. Red curve in (b) describes the normalized electric field intensity averaged within the Si nanodisk (F).

The simulated extinction spectra of the isolated Si disk and Au ring are also shown in Figure 7.4 as reference, showing no clear dips in comparison to the hybrid structure.

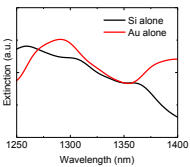

Figure 7.4. Simulated extinction spectra of the isolated Si disk and Au ring.

7.1.2. Electric field distribution and enhancement

In order to predict the THG capabilities of the hybrid structure, we evaluate its ability to concentrate the electric field inside the dielectric core. To that end, we numerically explore the normalized electric field intensity, averaged within the Si nanodisk, using the following expression:

$$F = \frac{\iiint |E|^2 \mathrm{d}V}{|E_0|^2 V} \tag{7.1}$$

where V is the volume of the Si nanoparticle, and $|E_0|$ the amplitude of the incident electric field. Interestingly, as shown in Figure 7.3(b), F (red curve) exhibits a sharp peak at the valley of the simulated extinction cross section (black curve). To further analyze the origin of this resonance, we computed its corresponding electric field distribution, shown in Figure 7.5a, which revealed the pattern of the anapole mode inside the dielectric, as anticipated[61,87,107]. When studying the composing particles separately, we found that the Au nanoring alone produced enhanced field regions mainly at its empty inner core (Figure 7.5b, left panel), enabling strong interaction with the dielectric nanodisk when placed at the geometrical center. Consistent with this, we observed that the electric field enhancement factor ($|E|/|E_0|$), which reached a maximum value of only 2 when considering the bare Si nanoparticle (Figure 7.5b, right panel), increased to around 9 for the hybrid nanosystem (Figure 7.5a), demonstrating the magnitude of the metal-dielectric coupling. Furthermore, by confining the electric field inside the Si nanodisk, rather than at the surfaces, undesirable energy losses from the surrounding metal were largely avoided.

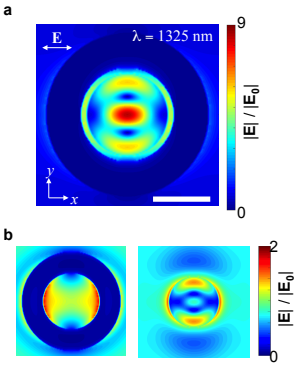

Figure 7.5. Normalized electric field distribution of the hybrid (a), bare Au nanoring (b, left panel) and isolated Si nanodisk (b, right panel), computed in the XY-plane at 40 nm above the substrate surface, at λ = 1325 nm.

7.2. Nonlinear optical measurement

7.2.1. Experimental verification of the enhancement in THG using the hybrid nanostructure

To experimentally analyze the nonlinear THG response from the fabricated samples, we employed a standard optical microscope setup coupled to femtosecond laser excitation, as detailed in Chapter 3.4.4. Figure 7.6 shows the measured TH spectra from the hybrid nanoantenna and its individual (isolated) components when exciting at λ = 1320 nm, i.e. at the valley of the extinction spectrum (Figure 7.3), where the electric field inside the dielectric is predicted to be maximum (Figure 7.3(b)). In all cases, a single peak at λ = 440 nm (1320 nm/3) was observed, as numerically predicted. Remarkably, the hybrid structure exhibited a TH intensity 1.6×10^3 and 3×10^5 times larger than that of the isolated

Si nanodisk, and that of the bare Au nanoring, respectively, demonstrating a strong interaction between its composing parts. The fact that the signal measured from the uncoupled Au nanoring was found to be significantly smaller than that from the individual Si nanodisk can be understood from the volume of excited nonlinear material. While the bare Si nanodisk enhanced the electric field mainly in its volume, the Au nanoring confined the light inside the empty ring core, inefficiently exciting the high third order susceptibility metal (see Figure 7.5b).

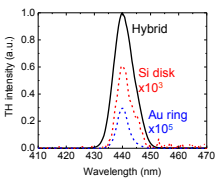

Figure 7.6. THG spectra of the hybrid structure, isolated Si nanodisk and bare Au nanoring measured at λ = 1320 nm excitation wavelength and 1 μW excitation power.

7.2.2. TH efficiency and effective third order susceptibility

To further study the nonlinear characteristics of the hybrid nanostructure, we also measured the absolute power of the collected TH emission when varying the excitation power, as shown in Figure 7.7a. As observed in the figure, at low excitation powers (below 1.5 μW), the TH intensity is found to increase with the cube of the pump power, as evidenced by the linear fit in logarithmic scale, which presents the expected slope equal to 3. However, for larger excitation powers (above 1.5 μW), the nanosystem deviated from the predicted trend, possibly due to heating effects induced by the strong illumination power, which would have weakened the nonlinear performance by driving the nanoantenna off resonance[61]. It should be noted here that no physical damage of the structure was observed in the range of powers analyzed. As a result, as shown in Figure 7.7b, the TH conversion efficiency, η_{TH}, defined as the ratio between emission and excitation powers, presented a saturation behavior, reaching a maximum value of 0.007%. Remarkably, this performance represents the highest TH efficiency reported to date on the nanoscale at optical frequencies, to the best of our knowledge. The obtained TH

efficiency exceeds by more than one order of magnitude previous reports on Si-based nanoantennas and metamaterials[82,83], and by a factor of 7 the case of the Ge nanodisk excited at a higher-order anapole mode[87]. By comparing the nonlinear performance of the hybrid system with that of bulk Si, we calculated the effective third-order nonlinear susceptibility of the hybrid nanoantenna to be $\chi^{(3)}_{Hybrid} = 4.96 \times 10^{-9}$ esu, which is around 1000 times higher than that of bulk Si[170]. Moreover, we obtained a penetration depth ($\delta = \lambda/4\pi\kappa$, with κ as the extinction coefficient) for the dielectric at 440 nm of ~200 nm, which is larger than the height of the Si disk, allowing effective extraction of TH light from the nanosystem.

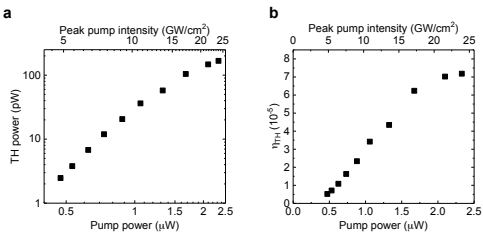

Figure 7.7. Measured TH power (a) and TH conversion efficiency (b) as a function of pump power at λ = 1320 nm. The dashed line in the figure 7.6(a) is a fit of the data considering the expected cubic dependence.

7.3. Scalability of highly efficient third harmonic generation

Finally, in order to expand the spectral range of operation of our system, we appropriately modified geometrical parameters of the nanoantenna to shift the anapole mode resonance to lower frequencies in the near-infrared regime, enabling efficient TH emission at longer wavelengths in the visible range. Figure 7.8 shows the extinction spectra of the hybrid structures in which the geometrical parameters were modified to expand the spectral range of operation of our nanosystem. The dimensions of the hybrid nanoantennas corresponding to the figures are as follows. (a) Si nanodisk: 840 nm

diameter and 195 nm height. Au nanoring: 940 nm inner diameter, 1720 nm outer diameter and 145 nm height. (b) Si nanodisk: 960 nm diameter and 220 nm height. Au nanoring: 1060 nm inner diameter, 1960 nm outer diameter and 160 nm height.

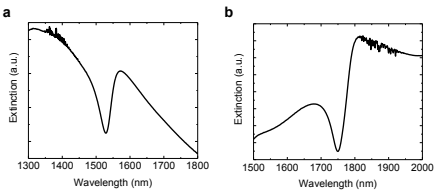

Figure 7.8. Experimental extinction spectra of the hybrid nanoantenna which generates TH at (a) λ = 515 nm and (b) λ = 590 nm.

Figure 7.9a shows the nonlinear response experimentally obtained from three different samples (corresponding SEM images on top), including the previously analyzed case, when varying the excitation wavelength at fixed pump power. As it can be observed, when the dimensions of the system are increased, the maximum TH efficiency is achieved at longer wavelengths. This result can be understood from the usual resonance redshift characteristic when increasing particle height or diameter[55,57]. In order to theoretically describe this behavior, in Figure 7.9b we plot, for the three different configurations, the spectral dependence of the third power of the normalized electric field intensity averaged within the dielectric (i.e., F^3). Noticeably, in all cases, the simulated curves suitably reproduced their corresponding nonlinear experimental results, in consistency with the characteristic of the THG phenomenon as a third-order nonlinear effect. Regarding the measured TH efficiencies, we find that they are within the same order of magnitude for all different frequencies, showing an effective control of the nonlinear emission throughout the visible regime.

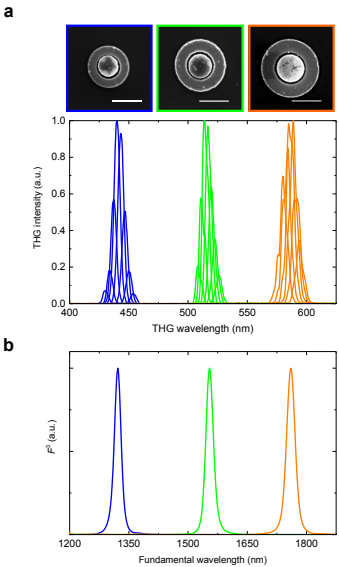

Figure 7.9. (a) Dependence of the TH spectrum on the excitation wavelength for the fabricated three hybrid nanoantennas at 1 μW excitation power, with respective SEM images displayed on top. The sets of curves are normalized to have equal maximum intensity. Each spectrum corresponds to a different fundamental wavelength of triple that of the central TH wavelength. (b) Corresponding spectral dependence of the simulated third power of the normalized electric field intensity averaged within the Si nanodisk.

7.4. Summary

In conclusion, we have demonstrated that a hybrid structure consisting of a Si nanodisk and a Au nanoring can generate strong TH emission in the optical range. The anapole mode supported by the dielectric core, boosted by the plasmonic resonance of the surrounding metal nanoparticle, produced high electric field enhancement within the Si nanostructure. As a result, the TH conversion efficiency was found to drastically improve due to the coupling between the individual components that define the hybrid structure, reaching values of up to 0.007%. We have also shown that the optimum emission wavelength can be tuned from the blue to the red region of the visible spectrum by suitably adapting the nanosystem geometrical dimensions. Combining plasmonic nanostructures with resonant high-index dielectric nanoparticles to enhance their field confinement capabilities presents as a key concept for the realization of highly efficient nonlinear optical systems at nanometer scales.

Chapter 8

Conclusion and outlook

8.1. Conclusion

In this thesis, a variety of high refractive index dielectric nanostructures have been studied to achieve efficient and tuneable control of electromagnetic waves in nanometer scale. High-index dielectric nanostructures can potentially compensate plasmonic nanostructures by overcoming their drawbacks, thanks to the excitation of both the electric and magnetic resonances without considerable energy losses. However, we still need to improve the performance of dielectric nanostructures in terms of efficiency, tunability and directionality for prospective future applications.

The work here has been carried out to address these issues and to extend the applications of high-index dielectric nanostructures. The first results chapter (Chapter 4) explored asymmetric high-index dielectric dimers to obtain highly efficient unidirectional forward scattering by fulfilling the first Kerker condition. Theoretical and numerical approach to analyze the optical responses of dielectric dimers verified that precise tuning of the geometric parameters of the dielectric dimers can attain the satisfaction of the first Kerker condition at the peak of electric and magnetic dipolar resonances. This led to the interference between the two dipoles, giving rise to the pursued unidirectional forward scattering with high scattering efficiency. The highly efficient unidirectional forward scattering was later experimentally demonstrated using a dark field optical spectroscopy which was designed to observe the forward and backward scattering from single nanoantennas. Chapter 5 focused on obtaining a control to switch between high transmission and reflection of metasurfaces formed by arrays of high-index dielectric dimers by just changing the linear polarization state of incident light. Mode hybridization of the high-index dielectric dimer can be altered by changing the linear incident polarization due to the coupling between electric and magnetic dipoles excited in the dimer. The hybridization resulted in spectral overlap and separation between the electric and magnetic modes, which are preferable for high transmission and reflection, respectively, when metasurfaces of periodic dielectric dimer arrays were formed. The

experimental demonstration of switching between high transmission and reflection was carried out using a metasurface of Si dimer arrays fabricated on a sapphire substrate and FTIR measurement setup. In Chapter 6, an extension of the directional control of scattering light by dielectric nanoantennas was demonstrated. This time, light was directed to the left and right side of the incident direction and parallel to the substrate. Asymmetric Si dimes were shown to have the capability of routing light scattering direction depending on the excitation wavelength. This is due to the interference between either electric or magnetic dipoles excited perpendicular to the dimer axis. The tuneable directional light scattering propagating along the substrate was confirmed experimentally with a back focal plane technique combined with prism coupling. The excited evanescent wave propagates along the substrate, exciting the asymmetric Si dimer on a silica substrate which scatters light in the left or right direction depending on the wavelength. The scattered light was monitored with a high numerical aperture objective, presenting scattering patterns on the back focal plane. A tuneable excitation of other Si dimers located at a certain distance from the source one, acting as targets, was also theoretically demonstrated, which could be applied for optical nanocircutry. Finally, in Chapter 7, high efficiency of THG in nanometer scale was attained with hybrid metal – dielectric nanoantennas. Resonances of a metal nanoring and high-index dielectric nanodisk can be strongly coupled, leading to the excitation of an enhanced anapole mode. The anapole mode in the hybrid structures amplified the electric field inside the dielectric nanodisk, which has a large third order susceptibility due to the generalized Miller's rule. The high field enhancement can generate highly efficient TH signal due to its cubic dependence on the field amplitude. The high efficiency of THG was experimentally verified using the Au – Si hybrid nanostructures, which were analyzed by a nonlinear optical measurement setup using a fs-pulsed laser. The maximum TH efficiency of the hybrid nanostructure reached 0.007 %, which is, to the best of our knowledge, the highest efficiency of THG in nanometer scale. Furthermore, this highly efficient THG is tuneable throughout the visible light regime by changing the dimensions of the structures.

Before presenting some concluding remarks, possible applications, where the optical effects that were revealed in this thesis could be of valuable help in a close future are described next:

- **Solar cells and light emitting optical devices showing high efficiency**

  Highly efficient unidirectional forward scattering demonstrated in Chapter 3 could enhance the efficiency of some optical devices. One example is a Si solar cell, which has the problem of high Fresnel reflection at the interface with air. High-index

dielectric nanoresonator were already reported to be able to perform the function of anti-reflection units[171,172]. To improve the ability of dielectric nanoantennas for anti-reflection, the asymmetric dielectric dimers showing more efficient unidirectional forward scattering could be a potential candidate. Also, light emitting devices, such as light emitting diodes, often suffer from the reduction in efficiency because of the Fresnel reflection and total reflection at the interface with air[173]. Our asymmetric dimer again could be a solution to circumvent the considerable reflection by scattering light only in the forward direction with high efficiency.

· **Spectroscopic or sensing applications for heat-degradable samples**

The directional control of light scattering from dielectric dimers demonstrated in Chapters 4 and 6 could be used for spectroscopic or sensing applications, especially for samples which are heat-sensitive. For example, proteins are in general degraded or denatured when exposed to excessive heat, which could be generated by LSPRs. On the other hand, dielectric dimers have been studied as low loss nanoantennas to enhance the spectroscopic and sensing efficiency without causing undesirable heat. To further boost the sensitivity, directional scattering could be employed, as reported by previous studies using bimetallic plasmonic nanoantennas[22,167,174]. Sensitivity of the applications could be enhanced by placing the detector in the scattering direction in the case of unidirectional scattering, or by tracing the ratio between the signal captured by two detectors in the case of tuneable scattering.

· **Tuneable optical nanocomponents to realize all-optical logical devices**

Chapters 5 and 6 presented the tuneability of light propagation direction; metasurfaces that can switch from high transmission to reflection, and optical nanoantennas that are able to tune the light scattering direction into the left or right side. These nanostructures could be the constituent unit cells in all-optical logical devices such as optical nanocircuitry[10–12]. In these devices, the active manipulation of light is required at nanometer scale, even below the Abbe's diffraction limit. The tuneable control of light propagation direction demonstrated in this work, which can be attained simply by changing the polarization or wavelength of excitation without substantial energy losses, could be one of key functions to realize the all-optical logical devices.

· **Efficient up-conversion nanosystems**

The major problem to employ nonlinear optical effects in nanometer scale is

certainly the efficiency. The work shown in Chapter 7 revealed a new methodology by employing hybrid metal – dielectric nanostructures to drastically enhance the efficiency in nanosystems, and it could be a breakthrough for the achievement of practical nonlinear up-conversion nanosystems. This could be used in various applications, such as bio-imaging[112], drug delivery[113], light energy harvesting devices[114,115] and sensors[175]. However, the realization of these future applications still may require further efficiency improvement.

Thus, dielectric nanostructures for the control of electromagnetic waves studied in this work could provide key elements, efficiency and tuneability, to the development of novel optical nanodevices, and hence, could boost the research in nanophotonics for practical applications.

8.2. Outlook

Our work has presented various dielectric nanostructures showing intriguing optical effects. Nevertheless, we still need to further explore the optical response of other dielectric nanostructures, based on the work here. Besides the demonstration of some immediate applications as shown above, following is a list of possible ideas to be explored in the near future.

- **Highly efficient unidirectional backward scattering by fulfilling the second Kerker condition**

  In some cases, backward scattering is preferable rather than forward scattering (e.g., spectroscopic technique using a microscope would prefer backward scattering as only one objective is required.). The highly efficient unidirectional backward scattering would be more challenging than the unidirectional forward scattering for two reasons. First, as discussed in Chapter 2.3, zero forward scattering cannot be achieved because of the causality principle, reducing the selectivity of scattering towards backward direction[71,72]. Second, the peak separation between electric and magnetic dipoles is preferable for unidirectional backward scattering, making it difficult to use the peak of the two dipolar resonances[73,74]. A possible solution is to use a bit complex structures, such as dielectric V-shape nanoantennas[21,132], to utilize not only dipolar resonances but also higher-order resonances. The interference including

higher order modes has more parameters to be tuned than the interference of only dipolar resonances, suggesting a potential achievement of the Kerker-type unidirectional backward scattering with high efficiency.

- **Polarization tuning of directional scattering from dielectric nanoantennas**

  Chapter 6 of the thesis has demonstrated the wavelength tuning of directional scattering from high-index dielectric nanoantennas in the optical regime. However, full color control into each direction would be preferred for practical displaying devices. Besides wavelengths, polarization states of incident light could be an alternative consideration to regulate the direction of scattering light from dielectric nanoantennas[104,176,177]. Due to the ability to excite electric and magnetic dipolar resonances orthogonally, the incident polarization determines which dipole would mainly contribute to the direction of light scattering, as discussed in Chapter 6. This exchange between the excited dipoles responsible for directional scattering could result in tuneable light scattering in either left or right direction, depending on the incident polarization, enabling the use of full color throughout the visible light wavelength.

- **Further investigation of hybrid nanostructures for highly efficient THG**

  The concept of using both the resonances of plasmonic and high-index dielectric nanoantennas was successfully demonstrated for THG in nanometer scale with high efficiency. We may still be able to improve the efficiency further by investigating hybrid nanostrucutres at a greater depth. Both of metallic and high-index dielectric materials can be substituted for other ones. For instance, Ag may be an alternative for Au due to its low absorption in visible light region, possibly reducing the energy losses at the TH wavelength.[45]. Also, Si could be replaced by Ge, which has been reported to exhibit high TH efficiency even with a single nanoscale object due to its large refractive index and third order susceptibility[61,87]. Furthermore, another study revealed that THG from a high-index dielectric nanoantenna has a directionality by a factor of up to twenty[88]. By considering the directionality, the efficiency of THG from hybrid nanostructures could be increased.

- **Hetero structures having resonances at the frequency of 3ω and ω for efficient THG**

  To date, most of studies of THG from dielectric nanoantennas have focused on the electric field enhancement at the fundamental frequency ω. However, the resonant mode of dielectric nanoantennas at the TH frequency 3ω could affect the performance

of THG. For example, if dielectric nanoantennas have a radiative resonance at the TH frequency, the generated TH field could be coupled to that radiative mode, increasing the efficiency of TH emission. We could fabricate ring-disk structures in which the ring and disk have a resonance at the fundamental and TH frequency, respectively, to investigate whether the radiative characteristics at TH frequency affect the efficiency of THG.

Appendix

A1. Lewin theory

The effective permittivity and permeability of a medium loaded with resonant nanoparticles can be deduced by calculating the scattered filed from the nanoparticles. Here we revisit a theory[101] providing the effective permittivity and permeability, which is called Lewin's theory.

Let us assume that the electromagnetic field propagates in a homogeneous medium along the $+z$ direction and is polarized along the x direction. The propagating field impinges on the interface (z = 0) with the same medium but embedding resonant nanoparticles. The electromagnetic field into the region with the nanoparticles, which has the effective permittivity ε and permeability μ, can be calculated as follows[101].

$$E_{x,t} = (1+r)E_0\exp\left(-ik_0 z\sqrt{\varepsilon\mu}\right) \tag{A2.1}$$

$$H_{y,t} = -(1+r)\sqrt{\varepsilon\mu}E_0\exp\left(-ik_0 z\sqrt{\varepsilon\mu}\right) \tag{A2.2}$$

where E_0 is the incident electric field, k_0 is the wavenumber in vacuum, and r is the reflection coefficient.

$$r = \frac{\sqrt{\frac{\mu}{\varepsilon}} - \sqrt{\frac{\mu_1}{\varepsilon_1}}}{\sqrt{\frac{\mu}{\varepsilon}} + \sqrt{\frac{\mu_1}{\varepsilon_1}}} \tag{A2.3}$$

ε_1 and μ_1 are the permittivity and permeability of the medium. Thus, the values of the effective permittivity ε and permeability μ can be obtained by calculating the propagation constant $k_0\sqrt{\varepsilon\mu}$ in the medium with nanoparticles and the reflection coefficient r.

Next, we consider the scattered field from a nanoparticle embedded in the medium. When the particle is small enough compared to the excitation wavelength, only the first scattering terms, which correspond the scattered field from electric and magnetic dipoles, need to be retained. The scattering coefficients are calculated as follows[101].

$$a_1 = i\frac{2}{3}\left(k_0{}^2\varepsilon_1\mu_1\right)^{\frac{3}{2}}a^3\frac{\varepsilon_1-\varepsilon_p}{2\varepsilon_1+\varepsilon_p} \tag{A2.4}$$

$$b_1 = i\frac{2}{3}\left(k_0{}^2\varepsilon_1\mu_1\right)^{\frac{3}{2}}a^3\frac{\mu_1-\mu_p}{2\mu_1+\mu_p} \tag{A2.5}$$

where a is the radius of the particle, and ε_p and μ_p are the effective permittivity and permeability of the resonating nanoparticle. These effective optical constants are calculated by[101]

$$\frac{\varepsilon_p}{\varepsilon_2}=\frac{\mu_p}{\mu_2}=\frac{2(\sin\theta-\theta\cos\theta)}{(\theta^2-1)\sin\theta+\theta\cos\theta} \tag{A2.6}$$

$$\theta = k_0 a\sqrt{\varepsilon_2\mu_2} \tag{A2.7}$$

where ε_2 and μ_2 are the permittivity and permeability of the material of the nanoparticle. The scattered electromagnetic fields at $z = z_0$ are given by[101]

$$\begin{aligned}E_{x,s} = a^3\Bigg[&E(z_0)\frac{\varepsilon_p-\varepsilon_1}{\varepsilon_p+2\varepsilon_1}\left(\frac{\partial^2}{\partial x^2}+k_0{}^2\varepsilon_1\mu_1\right)\\&-ik_0\mu_1H(z_0)\frac{\mu_p-\mu_1}{\mu_p+2\mu_1}\frac{\partial}{\partial z}\Bigg]\frac{\exp(-ik_0r_0)}{r_0}\sqrt{\varepsilon_1\mu_1}\end{aligned} \tag{A2.8}$$

$$\begin{aligned}H_{y,s} = a^3\Bigg[&H(z_0)\frac{\mu_p-\mu_1}{\mu_p+2\mu_1}\left(\frac{\partial^2}{\partial y^2}+k_0{}^2\varepsilon_1\mu_1\right)\\&-ik_0\varepsilon_1E(z_0)\frac{\varepsilon_p-\varepsilon_1}{\varepsilon_p+2\varepsilon_1}\frac{\partial}{\partial z}\Bigg]\frac{\exp(-ik_0r_0)}{r_0}\sqrt{\varepsilon_1\mu_1}\end{aligned} \tag{A2.9}$$

The transmitted field at (x, y, z) = (x_0, y_0, z_0) can be retained by summing the scattered electric field from all the nanoparticles and the incident field. The distance from each nanoparticle to the point at (x, y, z) = (x_0, y_0, z_0) can be calculated as $R_0 = \sqrt{(ls-x_0)^2+(ms-y_0)^2+(ns-z_0)^2}$ (s is the lattice constant of the particle array). The total transmitted field can be described in the following equation[101].

$$E(z_0) = E_0 \exp\left(-ik_0 z\sqrt{\varepsilon_1\mu_1}\right) + \sum_{l=-\infty}^{\infty}\sum_{m=-\infty}^{\infty}\sum_{n=0}^{\infty} a^3 \left[E(ns)\frac{\varepsilon_p - \varepsilon_1}{\varepsilon_p + 2\varepsilon_1}\left(\frac{\partial^2}{\partial {x_0}^2} + {k_0}^2\varepsilon_1\mu_1\right) - ik_0\mu_1 H(z_0)\frac{\mu_p - \mu_1}{\mu_p + 2\mu_1}\frac{\partial}{\partial z_0}\right]\frac{\exp(-ik_0 r_0)}{r_0}\sqrt{\varepsilon_1\mu_1} \quad \text{(A2.10)}$$

Mathematical manipulations can simplify the eq. (A2.8) as follows[101].

$$E(z_0) = E_0\exp\left(-ik_0 z_0\sqrt{\varepsilon_1\mu_1}\right) + \frac{4}{3}\pi\frac{a^3}{s^3}E(z_0)\frac{\varepsilon_p - \varepsilon_1}{\varepsilon_p + 2\varepsilon_1} - \frac{2i\pi}{k_0\sqrt{\varepsilon_1\mu_1}}\frac{a^3}{s^3}\int_0^{\infty}\left\{{k_0}^2\varepsilon_1\mu_1 E(\gamma)\frac{\varepsilon_p - \varepsilon_1}{\varepsilon_p + 2\varepsilon_1} + ik_0\mu_1 H(\gamma)\frac{\mu_p - \mu_1}{\mu_p + 2\mu_1}\frac{\partial}{\partial\gamma}\right\}\exp\left(-ik_0|\gamma - z_0|\sqrt{\varepsilon_1\mu_1}\right)d\gamma \quad \text{(A2.11)}$$

where $\gamma = ns$, and there is a similar equation for $H(z_0)$. The solution of these equations presents the transmitted electromagnetic field, from which we can derive the propagation constant and reflection coefficient. Finally, the effective permittivity and permeability of the medium loaded with nanoparticles are achieved in the following equations.

$$\varepsilon = \varepsilon_1\left(1 + \frac{3f}{\frac{\varepsilon_p + 2\varepsilon_1}{\varepsilon_p - \varepsilon_1} - f}\right) \quad \text{(A2.12)}$$

$$\mu = \mu_1\left(1 + \frac{3f}{\frac{\mu_p + 2\mu_1}{\mu_p - \mu_1} - f}\right) \quad \text{(A2.13)}$$

$$f = \frac{4}{3}\pi\frac{a^3}{s^3} \quad \text{(A2.14)}$$

where f is the ratio between the particles and the total volume of the mixture. Figure A.1

shows the effective permittivity and permeability of air embedding Si nanoparticles. The optical constants are obtained from ref[178] and, for simplicity, only the real value is considered. The radius of the nanoparticle and the lattice constant are set to 80 nm and 180 nm, respectively. The dispersive peaks are obtained at λ =520 nm and 650 nm in the effective permittivity and permeability. Furthermore, at λ = 500 – 520 nm and 600 – 650 nm, either the effective permittivity or permeability is negative, and the other is positive. This condition of single negative constant can give rise to the high reflection at the interface, as detailed in Chapter 2.4. Note that the wavelengths of the dispersive peaks correspond to those of the electric and magnetic dipolar resonances of a Si nanoparticle, as shown in Figure 2.2. This implies that the dispersive peaks observed with the effective constants would be de rive from the electric and magnetic dipolar resonances of the constituting nanoparticles.

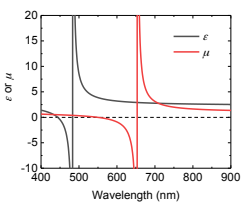

Figure A.1. The effective permittivity and permeability of air embedding Si calculated by Lewin's theory.

A2. Multipole theory for nanoantennas

Given the scattered electric field $\mathbf{E}_s$ is known in the medium surrounding the scattering particles, the multipole coefficients $a_E(l,m)$ and $a_M(l,m)$ can be calculated from the distribution of the scattered electric field on any spherical surface that encloses the scatterer.

$$a_E(l,m) = \frac{(-i)^{l+1} kr}{h_l^{(1)}(kr) E_0 [\pi(2l+1)l(l+1)]^{\frac{1}{2}}} \qquad \text{(A2.15)}$$

$$\int_0^{2\pi}\int_0^{\pi} Y_{lm}^{*}(\theta,\phi)\mathbf{u}_r \cdot \mathbf{E}_S(\mathbf{r}) \sin\theta \, d\theta d\phi$$

$$a_M(l,m) = \frac{(-i)^{l+1}\eta kr}{h_l^{(1)}(kr)E_0[\pi(2l+1)l(l+1)]^{\frac{1}{2}}} \int_0^{2\pi}\int_0^{\pi} Y_{lm}^{*}(\theta,\phi)\mathbf{u}_r \cdot \mathbf{H}_S(\mathbf{r}) \sin\theta \, d\theta d\phi \quad \text{(A2.16)}$$

where k is the wavenumber in the surrounding medium, $h_l^{(1)}$ is the spherical Hankel functions of the first kind, E_0 is the incident electric field amplitude, Y_{lm}^{*} is the scalar spherical harmonics, $\mathbf{E}_s$ and $\mathbf{H}_s$ are the scattered electric and magnetic fields.

Next, we consider the displacement current inside the particle. The displacement current related to the light scattering can be defined as follows.

$$\mathbf{J}_s(r) = -i\omega\varepsilon_0[\varepsilon(\mathbf{r}) - \varepsilon_m]\mathbf{E}_s(\mathbf{r}) \quad \text{(A2.17)}$$

where ε_m is the relatve permittivity of the surrounding medium. Inserting eq. (A2.17) into Maxwell equations provide the following equations.

$$\nabla \cdot \mathbf{E}_s(\mathbf{r}) = -\frac{i\eta}{k}\nabla \cdot \mathbf{J}_s(\mathbf{r}) \quad \text{(A2.18)}$$

$$\nabla \cdot \mathbf{H}_s(\mathbf{r}) = 0 \quad \text{(A2.19)}$$

$$\nabla \times \mathbf{E}_s(\mathbf{r}) = -ik\eta\mathbf{H}_s(\mathbf{r}) \quad \text{(A2.20)}$$

$$\nabla \times \mathbf{H}_s(\mathbf{r}) = -\frac{ik}{\eta}\mathbf{E}_s(\mathbf{r}) + \mathbf{J}_s(\mathbf{r}) \quad \text{(A2.21)}$$

From eq. (A2.18) – (A2.21), we can derive the scalar wave equations

$$(\nabla^2 + k^2)[\mathbf{r} \cdot \mathbf{E}_s(\mathbf{r})] = -ik\eta\mathbf{r} \cdot \mathbf{J}_s(\mathbf{r}) - i\frac{\eta}{k}\left(2 + r\frac{d}{dr}\right)[\nabla \cdot \mathbf{J}_s(\mathbf{r})] \quad \text{(A2.22)}$$

$$(\nabla^2 + k^2)[\mathbf{r} \cdot \mathbf{H}_s(\mathbf{r})] = \mathbf{r} \cdot [\nabla \times \mathbf{J}_s(\mathbf{r})] \quad \text{(A2.23)}$$

The multipole coefficients can be calculated by solving the eq. (A2.22) and (A2.23).

$$a_{\mathrm{E}}(l,m) = \frac{(-i)^{l+1}k^2\eta O_{lm}}{E_0[\pi(2l+1)]^{\frac{1}{2}}}\int \exp(-im\phi)\left\{[\Psi_l(kr)+\Psi_l{}''(kr)]P_l^m(\cos\theta)\mathbf{u}_r \cdot \mathbf{J}_{\mathrm{s}}(\mathbf{r}) + \frac{\Psi_l{}'(kr)}{kr}\left[\tau_{lm}(\theta)\mathbf{u}_\theta \cdot \mathbf{J}_{\mathrm{s}}(\mathbf{r}) - i\pi_{lm}(\theta)\mathbf{u}_\phi \cdot \mathbf{J}_{\mathrm{s}}(\mathbf{r})\right]\right\} d^3r \tag{A2.24}$$

$$a_{\mathrm{M}}(l,m) = \frac{(-i)^{l+1}k^2\eta O_{lm}}{E_0[\pi(2l+1)]^{\frac{1}{2}}}\int \exp(-im\phi)\, j_l(kr)\left[i\pi_{lm}(\theta)\mathbf{u}_\theta \cdot \mathbf{J}_{\mathrm{s}}(\mathbf{r}) + \tau_{lm}(\theta)\mathbf{u}_\phi \cdot \mathbf{J}_{\mathrm{s}}(\mathbf{r})\right] \tag{A2.25}$$

$$O_{lm} = \frac{1}{[l(l+1)]^{1/2}}\left[\frac{2l+1}{4\pi}\frac{(l-m)!}{(L+m)!}\right]^{1/2} \tag{A2.26}$$

$$\tau_{lm} = \frac{d}{d\theta}P_l^m(\cos\theta) \tag{A2.27}$$

$$\pi_{lm} = \frac{m}{\sin\theta}P_l^m(\cos\theta) \tag{A2.28}$$

where $\Psi_l(kr) = krj_l(kr)$ is the Riccati-Bessel functions and P_l^m is the associated Legendre polynomials. Note that the eq. (A2.24) and (A2.25) calculate the multipole coefficients, as well as eq. (A2.15) and (A2.16), but only by the electric field inside the particles.

Meanwhile, the induced current inside the particle can be also calculated using point electric current elements[179]. Let us assume a wire (length L) carrying a time-harmonic electric current (complex amplitude $\mathbf{I}$), which can be considered as a point current element.

$$\mathbf{J}_1(\mathbf{r}) = \mathbf{I}L\delta(\mathbf{r}) \tag{A2.29}$$

An oscillating point electric dipole can be assigned to this current element.

Next we treat two point elements where the two currents oscillate in opposite directions. An element of current +**I** is set at the distance of $s/2$ in the positive x direction, while the other element of a current **-I** is set at the same distance but in the negative x direction. This second order element can be deduced from the first one by applying an operator ς.

$$\mathbf{J}_2(\mathbf{r}) = \varsigma(\mathbf{u}_x)\mathbf{J}_2(\mathbf{r}) \tag{A2.30}$$

$$\varsigma(\mathbf{u}) = -s\frac{d}{du} \tag{A2.31}$$

ς can be defined also in the y and z directions. Any order element of point current can be obtained by sequentially applying the operator ς to the lowest order point element.

The amplitudes of the point current elements can be described by the lth-order current multipole moments.

$$\mathbf{M}^{(l)} = \frac{i}{(l-1)!\,\omega}\int \mathbf{J}(\mathbf{r})\mathbf{r}\mathbf{r}\ldots\mathbf{r}d^3r \tag{A2.32}$$

The multipoles of the orders l = 1,2 and 3 correspond to a dipole ($\mathbf{M}^{(1)} = \mathbf{p}$), quadrupole ($\mathbf{M}^{(2)} = \mathbf{Q}$) and octupole ($\mathbf{M}^{(3)} = \mathbf{O}$) moments, respectively.

The current density in the multipole expansion can be then written in the Cartesian coordinates by repeatedly applying the operator ς.

$$\mathbf{J}(\mathbf{r}) = i\omega\sum_{l=1}^{\infty}\sum_{\mathbf{u}_v=\mathbf{u}_x,\mathbf{u}_y,\mathbf{u}_z}\sum_{a=0}^{l-1}\sum_{b=0}^{l-a-1} M^{(l)}(\mathbf{u}_v,a,b)\,\mathbf{u}_v \frac{(-1)^l(l-1)!}{a!\,b!\,[l-(a+b+1)]}\frac{d^a}{dx^a}\frac{d^b}{dy^b}\frac{d^{l-(a+b+1)}}{dz^{l-(a+b+1)}}\delta(\boldsymbol{r}) \tag{A2.33}$$

where $M^{(l)}$ is the element corresponding to a multipole which can be calculated by applying the operator ς a times in the direction of x, b times in the direction of y, and l-(a+b+1) times in the direction of z. In order to recreate the coefficients $a_{\mathrm{E}}(l,m)$ and $a_{\mathrm{M}}(l,m)$ with $M^{(l)}$, we need to solve the equations of electromagnetic fields by the current described by eq (A2.33). Then a vector potential **A** is assumed in the following equation.

$$\mathbf{H}(\mathbf{r}) = \frac{1}{\mu_0}\nabla\times\mathbf{A}(\mathbf{r}) \tag{A2.34}$$

This vector **A** satisfies the wave equation

$$(\nabla^2 + k^2)\mathbf{A}(\mathbf{r}) = -\mu_0\mathbf{J}(\mathbf{r}) \tag{A2.35}$$

in which the vector **A** and the current **J** are correlated. The electric field can be calculated using the vector A by solving the following equation.

$$\mathbf{E}(\mathbf{r}) = -i\omega\left\{\mathbf{A}(\mathbf{r}) + \frac{1}{k^2}\nabla[\nabla\cdot\mathbf{A}(\mathbf{r})]\right\} \tag{A2.36}$$

Inserting the eq. (A2.36) into (A2.15) and (A2.16) provides the multipole coefficients described by the vector **A** which can be calculated by the current **J**. This current **J** can be deduced by the multipole elements $M^{(l)}$. Finally, we arrive at the multipole coefficients obtained by the multipole elements as follows.

$$\begin{aligned} a_{\mathrm{E}}(3,\pm3) = \sqrt{15}C_3\big[&\pm\big(O_{xxx} - O_{xyy} - 2O_{yyyx}\big) \\ &+ i\big(O_{yyy} - O_{yxx} - 2O_{xxy}\big)\big] \end{aligned} \tag{A2.37}$$

$$\begin{aligned} a_{\mathrm{E}}(3,\pm2) = \sqrt{10}C_3\big[&-2O_{xxz} + O_{yyz} - O_{zxx} + O_{zyy} \\ &\pm i\big(2O_{xyz} + 2O_{yzx} + 2O_{zxy}\big)\big] \end{aligned} \tag{A2.38}$$

$$\begin{aligned} a_{\mathrm{E}}(3,\pm1) = C_3\big[&\mp\big(3O_{xxx} + O_{xyy} - 4O_{xzz} + 2O_{yyx} - 8O_{zzx}\big) \\ &+ i\big(3O_{yyy} + O_{yxx} - 4O_{yzz} + 2O_{xxy} - 8O_{zzy}\big)\big] \end{aligned} \tag{A2.39}$$

$$a_{\mathrm{E}}(3,0) = 2\sqrt{3}C_3\big[2O_{xxz} + 2O_{yyz} - 2O_{zzz} + O_{zxx} + O_{zyy}\big] \tag{A2.40}$$

$$a_{\mathrm{E}}(2,\pm2) = 3C_2\big[Q_{xx} - Q_{yy} \mp i\big(Q_{xy} + Q_{yx}\big)\big] \tag{A2.41}$$

$$a_{\mathrm{E}}(2,\pm1) = 3C_2\big[\mp i(Q_{xz} + Q_{zx}) + i\big(Q_{yz} + Q_{zy}\big)\big] \tag{A2.42}$$

$$a_{\mathrm{E}}(2,0) = \sqrt{6}C_2\big[2Q_{zz} - Q_{xx} - Q_{yy}\big] \tag{A2.43}$$

$$a_{\mathrm{E}}(1,\pm1) = C_1\left[\mp p_x + ip_y\right] + 7C_3\left[\pm\left(O_{xxx} + 2O_{xyy} + 2O_{xzz} - O_{yyx} - O_{zzx}\right) - i\left(O_{yyy} + 2O_{yxx} + 2O_{xxy} - O_{xxxy} - O_{zzy}\right)\right] \quad \text{(A2.44)}$$

$$a_{\mathrm{E}}(1,0) = \sqrt{2}C_1 p_z + 7\sqrt{2}C_3\left[O_{xxz} + 2O_{yyz} - O_{zzz} - 2O_{zxx} - 2O_{zyy}\right] \quad \text{(A2.45)}$$

$$a_{\mathrm{M}}(2,\pm2) = 7C_3\left[\pm\left(-O_{xxz} + O_{yyz} + O_{zxx} - O_{zyy}\right) + i\left(O_{xyz} + O_{yzx} - 2O_{zxy}\right)\right] \quad \text{(A2.46)}$$

$$a_{\mathrm{M}}(2,\pm1) = 7C_3\left[-O_{xyy} + O_{xzz} + O_{yyx} - O_{zzx} \mp i\left(-O_{yxx} + O_{yzz} + O_{xxy} - O_{zzy}\right)\right] \quad \text{(A2.47)}$$

$$a_{\mathrm{M}}(2,0) = 7\sqrt{6}iC_3\left[O_{xyz} - O_{yzx}\right] \quad \text{(A2.48)}$$

$$a_{\mathrm{M}}(1,\pm1) = 5C_2\left[-Q_{xz} + Q_{zx} \mp i\left(-Q_{yz} + Q_{zy}\right)\right] \quad \text{(A2.49)}$$

$$a_{\mathrm{M}}(1,0) = 5\sqrt{2}iC_2\left[-Q_{xy} + Q_{yx}\right] \quad \text{(A2.50)}$$

where $C_1 = -ik^3/(6\pi\varepsilon E_0)$, $C_2 = -k^4/(60\pi\varepsilon E_0)$ and $C_3 = -ik^5/(210\pi\varepsilon E_0)$.

The obtained multipole coefficients can be used to identify the current excitations in the scattering nanoparticles. Special attention would be paid in the three electric dipoe coefficients $a_{\mathrm{E}}(1,\pm1)$ and $a_{\mathrm{E}}(1,0)$. An octupole current distribution can be found to produce electromagnetic field indistinguishable from the one created by an electric dipole. If you consider an octupole of $\mathbf{O} = O_{xxz} + O_{yyz} - 2O_{zxx} - 2O_{zyy}$, this current distribution generates exactly the same scattered field as a dipole moment $\mathbf{p} = 2|\ \mathbf{O}\ |k^2\mathbf{u}_z$. The vector potential of this octupole can be described in the following equation.

$$\mathbf{A}(\mathbf{r}) = \frac{1}{\omega}\frac{k^3}{4\pi\omega} 2O\left(\nabla\frac{d}{dz} + \mathbf{u}_z k^2\right) h_0^{(1)}(kr) \quad \text{(A2.51)}$$

where the second term is precisely the same as the one of the dipole moment above. The first term does not contribute to the radiated field, as this is the gradient of a scholar function.

This multipole theory can explain the origin of an anapole mode, which is described in Chapter 2.5 and used in Chapter 7. When a toroidal moment, which is one of octupole moments, destructively interfere with an electric dipolar moment with the same amplitude,

the total scattered field could vanish and the energy can be concentrated in the nanoparticle.

References

1. Weiner, J. & Ho, P. T. *Light-Matter Interaction*. *Light-Matter Interaction* **1,** (2007).
2. Novotny, L. *Principles of Nano-Optics*. *Nano Today* **1,** (2006).
3. Ohtsu, M. *Principles of Nanophotonics*. *Taylor & Francis Group* (2008).
4. Kirchain, R. & Kimerling, L. A roadmap for nanophotonics. *Nat. Photonics* **1,** 303–305 (2007).
5. Polman, A. & Atwater, H. a. Photonic design principles for ultrahigh-efficiency photovoltaics. *Nat. Mater.* **11,** 174–177 (2012).
6. Yu, Z., Raman, A. & Fan, S. Fundamental limit of nanophotonic light trapping in solar cells. *Proc. Natl. Acad. Sci. U. S. A.* **107,** 17491–6 (2010).
7. Fujii, T. *et al.* Increase in the extraction efficiency of GaN-based light-emitting diodes via surface roughening. *Appl. Phys. Lett.* **84,** 855–857 (2004).
8. Koo, W. H. *et al.* Light extraction from organic light-emitting diodes enhanced by spontaneously formed buckles. *Nat. Photonics* **4,** 222–226 (2010).
9. Yablonovitch, E. Photonic Crystals: Semiconductors of Light. *Sci. Am.* **285,** 46–55 (2001).
10. Almeida, V. R., Barrios, C. A., Panepucci, R. R. & Lipson, M. All-optical control of light on a silicon chip. *Nature* **431,** 1081–4 (2004).
11. Engheta, N. Circuits with light at nanoscales: Optical nanocircuits inspired by metamaterials. *Science.* **317,** 1698–1702 (2007).
12. Miller, D. A. B. Are optical transistors the logical next step? *Nat. Photonics* **4,** 3–5 (2010).
13. Assefa, S., Xia, F. & Vlasov, Y. a. Reinventing germanium avalanche photodetector for nanophotonic on-chip optical interconnects. *Nature* **464,** 80–84 (2010).
14. Abbe, E. A Contribution to the Theory of the Microscope and the nature of Microscopic Vision. *Proc. Bristol Nat. Soc.* **1,** 200 (1876).
15. Maier, S. *Plasmonics: fundamentals and applications*. (Springer, 2007).
16. Schuller, J. A. *et al.* Plasmonics for extreme light concentration and manipulation. *Nat. Mater.* **9,** 193–204 (2010).
17. Kik, P. G. & Brongersma, M. L. Surface plasmon nanophotonics. *Springer Ser. Opt. Sci.* **131,** 1–9 (2007).

18. Giannini, V. *et al.* Controlling light localization and light-matter interactions with nanoplasmonics. *Small* **6,** 2498–2507 (2010).
19. Novotny, L. Effective wavelength scaling for optical antennas. *Phys. Rev. Lett.* **98,** (2007).
20. Kosako, T., Hofmann, H. F. & Kadoya, Y. Directional emission of light from a nano-optical Yagi-Uda antenna. *Nat. Photonics* **4,** 4 (2009).
21. Vercruysse, D. *et al.* Unidirectional Side Scattering of Light by a Single-Element Nanoantenna. *Nano Lett.* **13,** 3843–3849 (2013).
22. Shegai, T. *et al.* A bimetallic nanoantenna for directional colour routing. *Nat. Commun.* **2,** 6 (2011).
23. Coenen, T., Arango, F. B., Koenderink, A. F. & Polman, A. Directional emission from a single plasmonic scatterer. *Nat. Commun.* **5,** (2014).
24. Atwater, H. A. & Polman, A. Plasmonics for improved photovoltaic devices. *Nat. Mater.* **9,** 205–213 (2010).
25. Nakayama, K., Tanabe, K. & Atwater, H. A. Plasmonic nanoparticle enhanced light absorption in GaAs solar cells. *Appl. Phys. Lett.* **93,** (2008).
26. Kwon, M. K. *et al.* Surface-plasmon-enhanced light-emitting diodes. *Adv. Mater.* **20,** 1253–1257 (2008).
27. Nie, S. M. & Emery, S. R. Probing single molecules and single nanoparticles by surface-enhanced Raman scattering. *Science.* **275,** 1102–1106 (1997).
28. Tarcha, P. J., DeSaja-Gonzalez, J., Rodriguez-Llorente, S. & Aroca, R. Surface-enhanced fluorescence on SiO2-coated silver island films. *Appl. Spectrosc.* **53,** 43–48 (1999).
29. Aroca, R. F., Ross, D. J. & Domingo, C. Surface-enhanced infrared spectroscopy. *Appl. Spectrosc.* **58,** (2004).
30. Anker, J. N. *et al.* Biosensing with plasmonic nanosensors. *Nat. Mater.* **7,** 442–453 (2008).
31. Brolo, A. Plasmonics for future biosensors. *Nat. Photonics* **6,** 709–713 (2012).
32. Knight, M. W., Sobhani, H., Nordlander, P. & Halas, N. J. Photodetection with Active Optical Antennas. *Science.* **332,** 702–704 (2011).
33. Pendry, J. B., Holden, A. J., Robbins, D. J. & Stewart, W. J. Magnetism from conductors and enhanced nonlinear phenomena. *IEEE Trans. Microw. Theory Tech.* **47,** 2075–2084 (1999).
34. Smith, D. R., Pendry, J. B. & Wiltshire, M. C. K. Metamaterials and negative refractive index. *Science.* **305,** 788–792 (2004).
35. Shalaev, V. M. Optical negative-index metamaterials. *Nat. Photonics* **1,** 41–48

(2007).
36. Valentine, J. *et al.* Three-dimensional optical metamaterial with a negative refractive index. *Nature* **455,** 376–379 (2008).
37. Pendry, J. B. Negative refraction makes a perfect lens. *Phys. Rev. Lett.* **85,** 3966–3969 (2000).
38. Cai, W., Chettiar, U., Kildishev, A. & Shalaev, V. Optical cloaking with metamaterials. *Nat. Photonics* **1,** 224 (2007).
39. Ergin, T., Stenger, N., Brenner, P., Pendry, J. B. & Wegener, M. Three-dimensional invisibility cloak at optical wavelengths. *Science* **328,** 337–9 (2010).
40. Khurgin, J. B. & Sun, G. Scaling of losses with size and wavelength in nanoplasmonics and metamaterials. *Appl. Phys. Lett.* **99,** (2011).
41. Khurgin, J. B. How to deal with the loss in plasmonics and metamaterials. *Nat. Nanotechnol.* **10,** 2–6 (2015).
42. Kim, J. *et al.* Optical properties of gallium-doped zinc oxide-a low-loss plasmonic material: First-principles theory and experiment. *Phys. Rev. X* **3,** (2014).
43. Boltasseva, A. & Atwater, H. A. Low-Loss Plasmonic Metamaterials. *Science.* **331,** 290–291 (2011).
44. Blaber, M. G., Arnold, M. D. & Ford, M. J. A review of the optical properties of alloys and intermetallics for plasmonics. *J. Phys. Condens. ...* **22,** 143201 (2010).
45. Palik, E. D. *Handbook of Optical Constants of Solids*. (Academic Press, 1985).
46. Coronado, E. A., Encina, E. R. & Stefani, F. D. Optical properties of metallic nanoparticles: manipulating light, heat and forces at the nanoscale. *Nanoscale* **3,** 4042–4059 (2011).
47. Hirsch, L. R. *et al.* Nanoshell-mediated near-infrared thermal therapy of tumors under magnetic resonance guidance. *Proc. Natl. Acad. Sci. U. S. A.* **100,** 13549–54 (2003).
48. Seol, Y., Carpenter, A. E. & Perkins, T. T. Gold nanoparticles : enhanced optical trapping and sensitivity coupled with significant heating. *Opt. Lett.* **31,** 2429–2431 (2006).
49. Popa, B. I. & Cummer, S. A. Compact dielectric particles as a building block for low-loss magnetic metamaterials. *Phys. Rev. Lett.* **100,** 207401 (2008).
50. Albella, P. *et al.* Low-Loss Electric and Magnetic Field-Enhanced Spectroscopy with Subwavelength Silicon Dimers. *J. Phys. Chem. C* **117,** 13573–13584 (2013).
51. Albella, P., de la Osa, R. A., Moreno, F. & Maier, S. A. Electric and Magnetic Field Enhancement with Ultralow Heat Radiation Dielectric Nanoantennas:

Considerations for Surface-Enhanced Spectroscopies. *ACS Photonics* **1,** 524–529 (2014).
52. Caldarola, M. *et al.* Non-plasmonic nanoantennas for surface enhanced spectroscopies with ultra-low heat conversion. *Nat. Commun.* **6,** 7915 (2015).
53. Kinkhabwala, A. *et al.* Large single-molecule fluorescence enhancements produced by a bowtie nanoantenna. *Nat. Photonics* **3,** 654–657 (2009).
54. Sigalas, M. M., Fattal, D. A., Williams, R. S., Wang, S. Y. & Beausoleil, R. G. Electric field enhancement between two Si microdisks. *Opt. Express* **15,** 14711–14716 (2007).
55. Evlyukhin, A. B., Reinhardt, C., Seidel, A., Luk'yanchuk, B. S. & Chichkov, B. N. Optical response features of Si-nanoparticle arrays. *Phys. Rev. B* **82,** 45404 (2010).
56. Garcia-Etxarri, A. *et al.* Strong magnetic response of submicron Silicon particles in the infrared. *Opt. Express* **19,** 4815–4826 (2011).
57. van de Groep, J. & Polman, A. Designing dielectric resonators on substrates: Combining magnetic and electric resonances. *Opt. Express* **21,** 26285–26302 (2013).
58. Kuznetsov, A. I., Miroshnichenko, A. E., Fu, Y. H., Zhang, J. B. & Luk'yanchuk, B. Magnetic light. *Sci. Rep.* **2,** 6 (2012).
59. Evlyukhin, A. B. *et al.* Demonstration of Magnetic Dipole Resonances of Dielectric Nanospheres in the Visible Region. *Nano Lett.* **12,** 3749–3755 (2012).
60. Shcherbakov, M. R. *et al.* Enhanced third-harmonic generation in silicon nanoparticles driven by magnetic response. *Nano Lett.* **14,** 6488–6492 (2014).
61. Grinblat, G., Li, Y., Nielsen, M. P., Oulton, R. F. & Maier, S. A. Enhanced Third Harmonic Generation in Single Germanium Nanodisks Excited at the Anapole Mode. *Nano Lett.* **16,** 4635–4640 (2016).
62. Cambiasso, J. *et al.* Bridging the gap between dielectric nanophotonics and the visible regime with effectively lossless GaP antennas. *Nano Lett.* **17,** 1219–1225 (2017).
63. Lippitz, M., Van Dijk, M. A. & Orrit, M. Third-harmonic generation from single gold nanoparticles. *Nano Lett.* **5,** 799–802 (2005).
64. Kauranen, M. & Zayats, A. V. Nonlinear plasmonics. *Nat. Photonics* **6,** 737–748 (2012).
65. Kim, S.-W. S. *et al.* High-harmonic generation by resonant plasmon field enhancement. *Nature* **453,** 757–760 (2008).
66. Du, J., Liu, S., Lin, Z., Zi, J. & Chui, S. T. Guiding electromagnetic energy below the diffraction limit with dielectric particle arrays. *Phys. Rev. A - At. Mol. Opt.*

Phys. **79,** (2009).
67. Krasnok, A. E., Miroshnichenko, A. E., Belov, P. A. & Kivshar, Y. S. Huygens optical elements and Yagi-Uda nanoantennas based on dielectric nanoparticles. *Jetp Lett.* **94,** 593–598 (2011).
68. Filonov, D. S. *et al.* Experimental verification of the concept of all-dielectric nanoantennas. *Appl. Phys. Lett.* **100,** 4 (2012).
69. Savelev, R. S., Slobozhanyuk, A. P., Miroshnichenko, A. E., Kivshar, Y. S. & Belov, P. A. Subwavelength waveguides composed of dielectric nanoparticles. *Phys. Rev. B* **89,** 7 (2014).
70. Bakker, R. M., Yu, Y. F., Paniagua-Domínguez, R., Luk'Yanchuk, B. & Kuznetsov, A. I. Resonant Light Guiding Along a Chain of Silicon Nanoparticles. *Nano Lett.* **17,** 3458–3464 (2017).
71. Kerker, M., Wang, D. S. & Giles, C. L. ELECTROMAGNETIC SCATTERING BY MAGNETIC SPHERES. *J. Opt. Soc. Am.* **73,** 765–767 (1983).
72. Nieto-Vesperinas, M., Gomez-Medina, R. & Saenz, J. J. Angle-suppressed scattering and optical forces on submicrometer dielectric particles. *J. Opt. Soc. Am. A-Optics Image Sci. Vis.* **28,** 54–60 (2011).
73. Geffrin, J. M. *et al.* Magnetic and electric coherence in forward- and back-scattered electromagnetic waves by a single dielectric subwavelength sphere. *Nat. Commun.* **3,** 8 (2012).
74. Fu, Y. H., Kuznetsov, A. I., Miroshnichenko, A. E., Yu, Y. F. & Luk'yanchuk, B. Directional visible light scattering by silicon nanoparticles. *Nat. Commun.* **4,** 6 (2013).
75. Person, S. *et al.* Demonstration of Zero Optical Backscattering from Single Nanoparticles. *Nano Lett.* **13,** 1806–1809 (2013).
76. Staude, I. *et al.* Tailoring Directional Scattering through Magnetic and Electric Resonances in Subwavelength Silicon Nanodisks. *ACS Nano* **7,** 7824–7832 (2013).
77. Decker, M. *et al.* High-Efficiency Dielectric Huygens' Surfaces. *Adv. Opt. Mater.* **3,** 813–820 (2015).
78. Slovick, B., Yu, Z. G., Berding, M. & Krishnamurthy, S. Perfect dielectric-metamaterial reflector. *Phys. Rev. B.* **88,** (2013).
79. Moitra, P., Slovick, B. A., Yu, Z. G., Krishnamurthy, S. & Valentine, J. Experimental demonstration of a broadband all-dielectric metamaterial perfect reflector. *Appl. Phys. Lett.* **104,** 5 (2014).
80. Moitra, P. *et al.* Large-Scale All-Dielectric Metamaterial Perfect Reflectors. *ACS Photonics* **2,** 692–698 (2015).

81. Shcherbakov, M. R. *et al.* Nonlinear interference and tailorable third-harmonic generation from dielectric oligomers. *ACS Photonics* **2,** 578–582 (2015).
82. Yang, Y. *et al.* Nonlinear Fano-Resonant Dielectric Metasurfaces. *Nano Lett.* **15,** 7388–7393 (2015).
83. Shorokhov, A. S. *et al.* Multifold Enhancement of Third-Harmonic Generation in Dielectric Nanoparticles Driven by Magnetic Fano Resonances. *Nano Lett.* **16,** 4857–4861 (2016).
84. Smirnova, D. A., Khanikaev, A. B., Smirnov, L. A. & Kivshar, Y. S. Multipolar Third-Harmonic Generation Driven by Optically Induced Magnetic Resonances. **3,** 1468 (2016).
85. Boyd, R. W. *Nonlinear Optics*. *Applied Optics* **5,** (2003).
86. Habteyes, T. G. *et al.* Near-Field Mapping of Optical Modes on All-Dielectric Silicon Nanodisks. *Acs Photonics* **1,** 794–798 (2014).
87. Grinblat, G., Li, Y., Nielsen, M. P., Oulton, R. F. & Maier, S. A. Efficient Third Harmonic Generation and Nonlinear Sub-Wavelength Imaging at a Higher-Order Anapole Mode in a Single Germanium Nanodisk. *ACS Nano* **11,** 953–960 (2017).
88. Wang, L. *et al.* Shaping the third-harmonic radiation from silicon nanodimers. *Nanoscale* **9,** 2201–2206 (2017).
89. Sautter, J. *et al.* Active Tuning of All-Dielectric Metasurfaces. *ACS Nano* **9,** 4308–4315 (2015).
90. Komar, A. *et al.* Electrically tunable all-dielectric optical metasurfaces based on liquid crystals. *Appl. Phys. Lett.* **110,** 71109 (2017).
91. Hu, J. *et al.* All-dielectric metasurface circular dichroism waveplate. *Nat. Publ. Gr.* **7,** 41893 (2017).
92. Gramotnev, D. K. & Bozhevolnyi, S. I. Plasmonics beyond the diffraction limit. *Nat. Photonics* **4,** 83–91 (2010).
93. Fernandez-Garcia, R., Sonnefraud, Y., Fernandez-Dominguez, A. I., Giannini, V. & Maier, S. A. Design considerations for near-field enhancement in optical antennas. *Contemp. Phys.* **55,** 1–11 (2014).
94. Verellen, N. *et al.* Fano Resonances in Individual Coherent Plasmonic Nanocavities 2009. **9,** 1663 (2009).
95. Govorov, A. O. & Richardson, H. H. Generating heat with metal nanoparticles. *Nano Today* **2,** 30–38 (2007).
96. Zhao, Q., Zhou, J., Zhang, F. & Lippens, D. Mie resonance-based dielectric metamaterials Increasing attention on metamaterials has been paid due to their. *Mater. Today* **12,** 60–69 (2009).

97. Mühlschlegel, P., Eisler, H.-J., Martin, O. J. F., Hecht, B. & Pohl, D. W. Resonant optical antennas. *Science* **308,** 1607–1609 (2005).
98. Bohren, C. F. & Huffman, D. R. *Absorption and Scattering of Light by Small Particles*. (John Wiley and Sons, 1983).
99. Van De Hulst, H. C. *Light scattering by small particles*. *Light Scattering by Small Particles* **1,** (1981).
100. Zambrana-Puyalto, X., Fernandez-Corbaton, I., Juan, M. L., Vidal, X. & Molina-Terriza, G. Duality symmetry and Kerker conditions. *Opt. Lett.* **38,** 1857–1859 (2013).
101. Lewin, L. The electrical constants of a material loaded with spherical particles. *J. Inst. Electr. Eng. III Radio Commun. Eng.* **94,** 65–68 (1947).
102. Chong, K. E. *et al.* Efficient Polarization-Insensitive Complex Wavefront Control Using Huygens' Metasurfaces Based on Dielectric Resonant Meta-atoms. *ACS Photonics* **3,** 514–519 (2016).
103. Chong, K. E. *et al.* Polarization-Independent Silicon Metadevices for Efficient Optical Wavefront Control. *Nano Lett.* **15,** 5369–5374 (2015).
104. Arbabi, A., Horie, Y., Bagheri, M. & Faraon, A. Dielectric metasurfaces for complete control of phase and polarization with subwavelength spatial resolution and high transmission. *Nat. Nanotechnol.* **10,** 937–943 (2015).
105. Chen, X., Grzegorczyk, T. M., Wu, B. I., Pacheco, J. & Kong, J. A. Robust method to retrieve the constitutive effective parameters of metamaterials. *Phys. Rev. E.* **70,** 1–7 (2004).
106. Smith, D. R., Vier, D. C., Koschny, T. & Soukoulis, C. M. Electromagnetic parameter retrieval from inhomogeneous metamaterials. *Phys. Rev. E.* **71,** 1–11 (2005).
107. Miroshnichenko, A. E. *et al.* Nonradiating anapole modes in dielectric nanoparticles. *Nat. Commun.* **6,** 8069 (2015).
108. Grahn, P., Shevchenko, A. & Kaivola, M. Electromagnetic multipole theory for optical nanomaterials. *New J. Phys.* **14,** (2012).
109. Nemkov, N. A., Stenishchev, I. V. & Basharin, A. A. Nontrivial nonradiating all-dielectric anapole. *Sci. Rep.* **7,** 1064 (2017).
110. Wang, R. & Dal Negro, L. Engineering non-radiative anapole modes for broadband absorption enhancement of light. *Opt. Express* **24,** 19048 (2016).
111. Franken, P. A., Hill, A. E., Peters, C. W. & Weinreich, G. Generation of optical harmonics. *Phys. Rev. Lett.* **7,** 118–119 (1961).
112. Débarre, D. *et al.* Imaging lipid bodies in cells and tissues using third-harmonic

generation microscopy. *Nat. Methods* **3,** 47–53 (2006).
113. Zhou, J., Liu, Z. & Li, F. Upconversion nanophosphors for small-animal imaging. *Chem. Soc. Rev.* **41,** 1323–1349 (2012).
114. Zou, W., Visser, C., Maduro, J. a., Pshenichnikov, M. S. & Hummelen, J. C. Broadband dye-sensitized upconversion of near-infrared light. *Nat. Photonics* **6,** 560–564 (2012).
115. Huang, X., Han, S., Huang, W. & Liu, X. Enhancing solar cell efficiency: the search for luminescent materials as spectral converters. *Chem. Soc. Rev.* **42,** 173–201 (2013).
116. Boyd, R. W. Nonlinear optics. in *Handbook of Laser Technology and Applications* (eds. Webb, C. & Jones, J.) pp161–184 (IoP Publishing, 2004).
117. Klein, M. W., Wegener, M., Feth, N. & Linden, S. Experiments on second-and third-harmonic generation from magnetic metamaterials. *Opt. Express* **15,** 5238–5247 (2007).
118. Hentschel, M., Utikal, T., Giessen, H. & Lippitz, M. Quantitative modeling of the third harmonic emission spectrum of plasmonic nanoantennas. *Nano Lett.* **12,** 737–748 (2012).
119. Metzger, B., Schumacher, T., Hentschel, M., Lippitz, M. & Giessen, H. Third Harmonic Mechanism in Complex Plasmonic Fano Structures. *ACS Photonics* **1,** 471–476 (2014).
120. Aouani, H., Rahmani, M., Navarro-Cía, M. & Maier, S. A. Third-harmonic-upconversion enhancement from a single semiconductor nanoparticle coupled to a plasmonic antenna. *Nat. Nanotechnol.* **9,** 290–294 (2014).
121. Metzger, B. *et al.* Doubling the efficiency of third harmonic generation by positioning ITO nanocrystals into the hot-spot of plasmonic gap-antennas. *Nano Lett.* **14,** 2867–2872 (2014).
122. Aouani, H., Navarro-Cía, M., Rahmani, M. & Maier, S. A. Unveiling the Origin of Third Harmonic Generation in Hybrid ITO-Plasmonic Crystals. *Adv. Opt. Mater.* **3,** 1059–1065 (2015).
123. King, M. D., Khadka, S., Craig, G. A. & Mason, M. D. Effect of local heating on the SERS efficiency of optically trapped prismatic nanoparticles. *J. Phys. Chem. C* **112,** 11751–11757 (2008).
124. Tai, C.-T. *Dyadic Green functions in electromagnetic theory*. *IEEE Press* (1994).
125. Schmidt, M. K. *et al.* Dielectric antennas - a suitable platform for controlling magnetic dipolar emission. *Opt. Express* **20,** 13636–13650 (2012).

126. Yee, K. S. Numerical solution of initial boundary value problems involving Maxwell's equations in isotropic media. *IEEE Trans. Antennas Propag.* **14,** 302–307 (1966).
127. Kuzmin, P. G. *et al.* Silicon Nanoparticles Produced by Femtosecond Laser Ablation in Ethanol: Size Control, Structural Characterization, and Optical Properties. *J. Phys. Chem. C* **114,** 15266–15273 (2010).
128. Shi, L., Tuzer, T. U., Fenollosa, R. & Meseguer, F. A New Dielectric Metamaterial Building Block with a Strong Magnetic Response in the Sub-1.5-Micrometer Region: Silicon Colloid Nanocavities. *Adv. Mater.* **24,** 5934–+ (2012).
129. Shi, L. *et al.* Monodisperse silicon nanocavities and photonic crystals with magnetic response in the optical region. *Nat. Commun.* **4,** 7 (2013).
130. Zywietz, U., Evlyukhin, A. B., Reinhardt, C. & Chichkov, B. N. Laser printing of silicon nanoparticles with resonant optical electric and magnetic responses. *Nat. Commun.* **5,** 7 (2014).
131. Bottein, T. *et al.* 'Black' Titania Coatings Composed of Sol-Gel Imprinted Mie Resonators Arrays. *Adv. Funct. Mater.* **27,** 1604924 (2017).
132. Li, J. *et al.* All-Dielectric Antenna Wavelength Router with Bidirectional Scattering of Visible Light. *Nano Lett.* **16,** 4396–4403 (2016).
133. Curto, A. G. *et al.* Unidirectional emission of a quantum dot coupled to a nanoantenna. *Science* **329,** 930–933 (2010).
134. Bouhelier, a & Wiederrecht, G. P. Surface plasmon rainbow jets. *Opt. Lett.* **30,** 884–886 (2005).
135. Miyazaki, H. T. *et al.* Light diffraction from a bilayer lattice of microspheres enhanced by specular resonance. *J. Appl. Phys.* **95,** 793–805 (2004).
136. Wang, H. *et al.* Janus Magneto-Electric Nanosphere Dimers Exhibiting Unidirectional Visible Light Scattering and Strong Electromagnetic Field Enhancement. *ACS Nano* **9,** 436–448 (2015).
137. Luk'yanchuk, B. S., Voshchinnikov, N. V., Paniagua-Domínguez, R. & Kuznetsov, A. I. Optimum Forward Light Scattering by Spherical and Spheroidal Dielectric Nanoparticles with High Refractive Index. *ACS Photonics* **2,** 993–999 (2015).
138. Liu, W. *et al.* Ultra-directional forward scattering by individual core-shell nanoparticles. *Opt. Express* **22,** 16178 (2014).
139. Naraghi, R. R., Sukhov, S. & Dogariu, A. Directional control of scattering by all-dielectric core-shell spheres. *Opt. Lett.* **40,** 585–588 (2015).
140. Zywietz, U. *et al.* Electromagnetic Resonances of Silicon Nanoparticle Dimers in the Visible. *Acs Photonics* **2,** 913–920 (2015).

141. Bakker, R. M. *et al.* Magnetic and Electric Hotspots with Silicon Nanodimers. *Nano Lett.* **15,** 2137–2142 (2015).
142. Groep, J. van de, Coenen, T., Mann, S. A. & Polman, A. Direct imaging of hybridized eigenmodes in coupled silicon nanoparticles. *Optica* **3,** 7 (2016).
143. Yan, J. H. *et al.* Directional Fano Resonance in a Silicon Nano sphere Dimer. *ACS Nano* **9,** 2968–2980 (2015).
144. Rolly, B., Geffrin, J. M., Abdeddaim, R., Stout, B. & Bonod, N. Controllable emission of a dipolar source coupled with a magneto-dielectric resonant subwavelength scatterer. *Sci. Rep.* **3,** 5 (2013).
145. Krasnok, A. E., Miroshnichenko, A. E., Belov, P. A. & Kivshar, Y. S. All-Dielectric Optical Nanoantennas. in *5th International Workshop on Theoretical and Computational Nano-Photonics (TaCoNa-Photonics)* **1475,** 22–24 (Amer Inst Physics, 2012).
146. Rolly, B., Stout, B. & Bonod, N. Boosting the directivity of optical antennas with magnetic and electric dipolar resonant particles. *Opt. Express* **20,** 20376–20386 (2012).
147. Yu, N. & Capasso, F. Flat optics with designer metasurfaces. *Nat. Mater.* **13,** 139–150 (2014).
148. Kildishev, A. V., Boltasseva, A. & Shalaev, V. M. Planar photonics with metasurfaces. *Science.* **339,** 1232009 (2013).
149. Ni, X., Emani, N. K., Kildishev, A. V, Boltasseva, A. & Shalaev, V. M. Broadband Light Bending with Plasmonic Nanoantennas. *Science.* **335,** 427 (2012).
150. Pfeiffer, C. *et al.* Efficient light bending with isotropic metamaterial Huygens' surfaces. *Nano Lett.* **14,** 2491–2497 (2014).
151. Aieta, F. *et al.* Aberration-free ultrathin flat lenses and axicons at telecom wavelengths based on plasmonic metasurfaces. *Nano Lett.* **12,** 4932–4936 (2012).
152. Li, W. & Valentine, J. Metamaterial perfect absorber based hot electron photodetection. *Nano Lett.* **14,** 3510–3514 (2014).
153. Lin, D. M., Fan, P. Y., Hasman, E. & Brongersma, M. L. Dielectric gradient metasurface optical elements. *Science.* **345,** 298–302 (2014).
154. West, P. R. *et al.* All-dielectric subwavelength metasurface focusing lens. *Opt. Express* **22,** 26212 (2014).
155. Wu, C. *et al.* Spectrally selective chiral silicon metasurfaces based on infrared Fano resonances. *Nat. Commun.* **5,** 3892 (2014).
156. Yang, Y., Kravchenko, I. I., Briggs, D. P. & Valentine, J. All-dielectric metasurface analogue of electromagnetically induced transparency. *Nat. Commun.*

5, 5753 (2014).

157. Shalaev, M. I. *et al.* High-Efficiency All-Dielectric Metasurfaces for Ultracompact Beam Manipulation in Transmission Mode. *Nano Lett.* **15,** 6261–6266 (2015).
158. Kruk, S. *et al.* Broadband highly-efficient dielectric metadevices for polarization control. *APL Photonics* **1,** 30801 (2016).
159. Yi, N. *et al.* Large-Scale and Defect-Free Silicon Metamaterials with Magnetic Response. *Sci. Rep.* **6,** 25760 (2016).
160. Odebo Länk, N., Verre, R., Johansson, P. & Käll, M. Large-Scale Silicon Nanophotonic Metasurfaces with Polarization Independent Near-Perfect Absorption. *Nano Lett.* **17,** 3054–3060 (2017).
161. Wang, F., Wei, Q. H. & Htoon, H. Generation of steep phase anisotropy with zero-backscattering by arrays of coupled dielectric nano-resonators. *Appl. Phys. Lett.* **105,** 5 (2014).
162. Zhang, J., Liu, W., Yuan, X. & Qin, S. Electromagnetically induced transparency-like optical responses in all-dielectric metamaterials. *J. Opt.* **16,** 125102 (2014).
163. Ma, Z. *et al.* Terahertz All-Dielectric Magnetic Mirror Metasurfaces. *ACS Photonics* **3,** 1010–1018 (2016).
164. Prodan, E., Radloff, C., Halas, N. J. & Nordlander, P. A hybridization model for the plasmon response of complex nanostructures. *Science* **302,** 419–422 (2003).
165. Nordlander, P., Oubre, C., Prodan, E., Li, K. & Stockman, M. I. Plasmon hybridization in nanoparticle dimers. *Nano Lett.* **4,** 899–903 (2004).
166. Koh, A. L. *et al.* Electron energy-loss spectroscopy (EELS) of surface plasmons in single silver nanoparticles and dimers: Influence of beam damage and mapping of dark modes. *ACS Nano* **3,** 3015–3022 (2009).
167. Shegai, T., Johansson, P., Langhammer, C. & Kall, M. Directional Scattering and Hydrogen Sensing by Bimetallic Pd-Au Nanoantennas. *Nano Lett.* **12,** 2464–2469 (2012).
168. Zhai, W. C. *et al.* Anticrossing double Fano resonances generated in metallic / dielectric hybrid nanostructures using nonradiative anapole modes for enhanced nonlinear optical effects. *Opt. Express* **24,** 27858–27869 (2016).
169. Rakovich, A., Albella, P. & Maier, S. A. Plasmonic control of radiative properties of semiconductor quantum dots coupled to plasmonic ring cavities. *ACS Nano* **9,** 2648–2658 (2015).
170. Lin, Q. *et al.* Dispersion of silicon nonlinearities in the near infrared region. *Appl. Phys. Lett.* **91,** 21111 (2007).

171. Spinelli, P., Verschuuren, M. A. & Polman, A. Broadband omnidirectional antireflection coating based on subwavelength surface Mie resonators. *Nat. Commun.* **3,** 5 (2012).
172. Brongersma, M. L., Cui, Y. & Fan, S. H. Light management for photovoltaics using high-index nanostructures. *Nat. Mater.* **13,** 451–460 (2014).
173. Schubert, E. F., Gessmann, T. and Kim, J. K. Light emitting diodes. *Kirk-Othmer Encycl. Chem. Technol.* 1–31 (2005).
174. Wersäll, M. *et al.* Directional nanoplasmonic antennas for self-referenced refractometric molecular analysis. *J. Phys. Chem. C* **118,** 21075–21080 (2014).
175. Darbha, G. K. *et al.* Selective detection of mercury (II) ion using nonlinear optical properties of gold nanoparticles. *J. Am. Chem. Soc.* **130,** 8038–8043 (2008).
176. Barreda, A. I. *et al.* Electromagnetic polarization controlled perfect switching effect with high refractive index dimers. the beam-splitter configuration. *Nat. Commun.* **8,** 13910 (2017).
177. Shen, B., Wang, P., Polson, R. & Menon, R. An integrated-nanophotonics polarization beamsplitter with 2.4 x 2.4 μm^2 footprint. *Nat. Photonics* **9,** 378–382 (2015).
178. Palik, E. D. *Handbook of Optical Constants of Solids, Vol. 1.*
179. Soediono, B. *Time Harmonic Electromagnetic Fields, 1961. Journal of Chemical Information and Modeling* **53,** (1989).

Publications

Journal publications

1. T. Shibanuma, P. Albella and S. A. Maier, "Unidirectional light scattering with high efficiency at optical frequencies based on low-loss dielectric nanoantennas", *Nanoscale*, **8**, 14184 (2016).

2. T. Shibanuma, P. Albella and S. A. Maier, "Polarization control of high transmission / reflection switching by all-dielectric metasurfaces", *in preparation.*

3. P. Albella*, T. Shibanuma* and S. A. Maier, "Switchable directional scattering of electromagnetic radiation with subwavelength asymmetric silicon dimers", *Scientific Reports*, **5**, 18322 (2015). (*These authors contributed equally to this work.)

4. T. Shibanuma, T. Matsui, T. Roschuk, J. Wojcik, P. Mascher, P. Albella and S. A. Maier, "Experimental demonstration of tunable directional scattering of visible light from all-dielectric asymmetric dimers", *ACS Photonics*, **4**, 489 (2017).

5. T. Shibanuma, G. Grinblat, P. Albella and S. A. Maier, "Efficient Third Harmonic Generation from Metal–Dielectric Hybrid Nanoantennas", *Nano Letters*, **17**, 2647 (2017).

6. J. Gargiulo, T. Brick, I. L. Violi, F. C. Herrer, T. Shibanuma, P. Albella, F. G. Requejo, E. Cortes, S. A. Maier, F. D. Stefani, "Understanding and reducing photo-thermal forces for the fabrication of Au nanoparticle dimers by optical printing", *Nano Letters*, accepted.

Conference presentations

1. Oral – "Efficient Directional Control of Scattered Field at Optical Frequencies with Subwavelength Asymmetric Dielectric Dimers", Metamaterials' 2016.

2. Poster – "Asymmetric dielectric nanoparticle dimers for control of scattering direction", Postgraduate Symposium 2016

3. Poster – “Asymmetric Dimers of Dielectric Nanoparticles for Efficient Control of Scattering Direction”, London Plasmonics Forum 2016

4. Poster – “High-Index Dielectric Nanoparticles for the Control of Electromagnetic Waves”, RPLAS meeting 2017

List of Figures

Acknowledgements

I would like to thank Prof. Stefan A. Maier for giving me such a wonderful opportunity to pursuit my PhD at Imperial College London. It has been a huge honor to study as a PhD student under the supervision of the top professor in the nanophotonics research field.

I also would like to express my sincere appreciation to Dr. Pablo Albella for his supervision throughout my PhD. I have learned a lot from his expertise in nanophotonics, his experiences as a successful scholar, and his attitude to science.

It has been a great pleasure to work with brilliant and cheerful members in Plasmonics Group. In particular, Dr. Takayuki Matsui, Dr. Yi Li, Dr. Gustavo Grinblat, and Dr. Emiliano Cortes have given me lots of guidance which is of course helpful in my PhD.

Friendship with those who sit in H722 PhD student office is priceless treasure for me. I have shared great memories with Ms. Ngoc Nguyen, Mr. Rodrigo Berte, Mr. Javier Cambiasso (even he is in another office!), Mr. Zhijie Ma, Mr. Daan Arroo, Mr. Albert Lauri, Mr. Thomas Brick, Mr. Xiaofei Xiao, Mr. Brock Doiron, Ms. Harriet Walker, Ms. Monica Mota, and Mr. Nicholas Gusken.

I further acknowledge JXTG Nippon Oil & Energy corporation for giving me a chance to study abroad and for financially supporting my PhD.

I want to thank my siblings and parents. My father and mother are the ideal parents whom I always follow.

Above all, I want to say the biggest thanks to my lovely family, Keiko and Karen. PhD at Imperial College London is undoubtedly a tough course, and I often got frustrated, sometimes even wanted to give it up. Without Keiko's and Karen's support and love, I surely could not go that far beyond my ability.